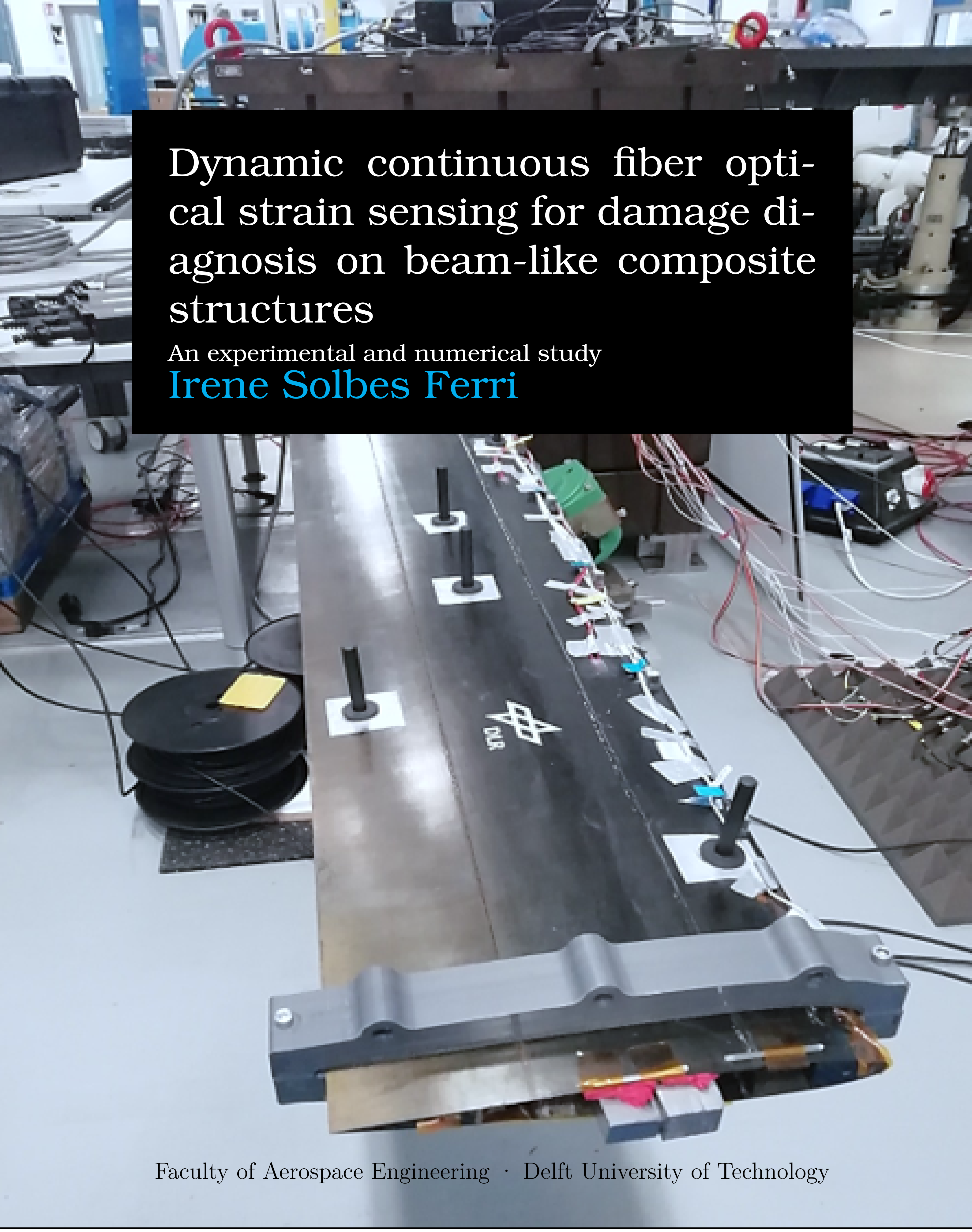

Dynamic continuous fiber optical strain sensing for damage diagnosis on beam-like composite structures

An experimental and numerical study

Irene Solbes Ferri

Faculty of Aerospace Engineering · Delft University of Technology

Dynamic continuous fiber optical strain sensing for damage diagnosis on beam-like composite structures

An experimental and numerical study

MASTER OF SCIENCE THESIS

For obtaining the degree of Master of Science in Aerospace Engineering
at Delft University of Technology

Irene Solbes Ferri

February 10th, 2022

Faculty of Aerospace Engineering · Delft University of Technology

TU Delft
Delft
University of
Technology

DLR
Deutsches Zentrum
für Luft- und Raumfahrt
German Aerospace Center

Delft University of Technology
Faculty of Aerospace Engineering
Department of Aerospace Structures and Materials

GRADUATION COMMITTEE

Dated: February 10th, 2022

Chair holder:

Dr. Roger Groves

Committee members:

Dr. Saullo Giovani Pereira Castro

Dr. Julie Teuwen

Dr. Xuerui Wang

Preface

The present master thesis report is the final step to becoming a Master of Science in Aerospace Structures and Materials by the University of TU Delft. It comprises the experimental and numerical work conducted at the department of Structural Dynamics and System Identification from the DLR Aeroelasticity Institute, in combination with the TU Delft's Aerospace Structures and Materials department.

The author would like to thank the supervisors of this thesis for their time, feedback and suggestions in every single Monday meeting. Thanks to Yves for the internship and thesis experience. Thanks to Saullo for offering me this opportunity and for walking this path of one year and a half with me. Thanks to Roger for all the meticulous advice and comments during the thesis and also thanks for making me feel a part of the NDT department from the beginning. Thanks, Johannes, for all your time, patience, and help during my stay at DLR, it was not always easy but we did a job to be proud of!

The acknowledgements for all my family and friends would take longer than the report itself so I am going to be brief and thank all of you for the support, laughs, time, and love that you shared and gave me during my Master. If someone deserves an especial mention that is Huub Urselmann, thanks for walking alongside me in Delft, Goettingen and Callosa, I hope we walk together many more years.

Last but not least I would like to thank from the bottom of my heart every girl and woman who dared defy the norms and become an engineer. Thanks to every woman that I met during these seven years because without you, I would not be here, and without the ones before us, non of us would be here. Together, we will keep defying gravity.

Irene Solbes Ferri

Delft, The Netherlands, February 2022

“Work is what you do for others, liebchen. Art is what you do for yourself.”

— *Stephen Sondheim, Sunday in the Park with George.*

Abstract

The aerospace and wind energy sectors keep relying more and more on composite materials for their components due to their high specific mechanical properties and tailored design capabilities. Composite materials, however, exhibit complex types of damages which can be challenging to diagnose with inspection techniques and sensors created for metallic or concrete structures. The current inspection methods are often expensive, time-consuming and require the structure to be readily accessible. Vibration-based structural health monitoring technologies are a promising choice as they are capable of online continuous monitoring of the component's health. These methods rely on changes in the structure's modal parameters to identify local damages globally in the structure.

Many vibration-based methods have been proposed in the literature during the last decades, however, few of them have been successfully applied to complex composite structures or during operational conditions. The performance of the method depends on the considered damage scenario, the sensing technique and the structure itself. This thesis focuses on the damage diagnosis in complex beam-like composite structures with a state-of-the-art optical fibre sensing technique capable of acquiring high-spatial-resolution modal parameters. The chosen methods in the present thesis are based on modal curvature and modal strain energy shapes which, according to literature, are the most sensitive to local damages.

The dynamic data extracted from the used wing specimen by this optical fibre sensing technique has been validated through a three-step approach. The natural frequencies and modal shapes are compared to those of typical sensors in vibration testing such as accelerometers and strain gauges. The dynamic strain shapes obtained with the optical fibres are compared to their corresponding static shapes concluding that the same features were present in both shapes. Finally, the repeatability of the experimental set-up was tested by computing the error and standard deviation between seven measurements carried out at different times and days.

The validated parameters from the optical fibres were used in the damage identification procedure as the undamaged configuration of the wing. The damaged configurations were obtained by 18 damage experiments in which damages were introduced using mass attachments at the selected positions of the wing. The design of experiments was performed with the Taguchi method. In order to detect and locate these damages, an algorithm was created in MatLab to compare undamaged and damaged states employing the selected vibration-based methods.

The experimental results from the damage scenarios highlighted that the selected methods and sensing technique are capable of detecting damages in all scenarios. The damage location was successful in most of the scenarios, however, the root of the wing has lower accuracy and probability of correct damage location than the wingtip because the stiffness and mass at the root are the highest along the wingspan. This lead to the conclusion that the location accuracy of damage depends on the relative change of mass or stiffness of that damage with respect to its location. The used vibration-based methods were compared to each other concluding that, although these methods can detect and located damages in more than half of the experiments, the optimal approach is to use a combination of them to enhance the damage identification.

The obtained results and conclusions from this project are expected to assist in the improvement of structural health monitoring techniques for composite structures in the aerospace and wind energy sector. This vibration-based damage identification technique can extend the lifetime of structures by preventing the unnecessary replacement of its components or detecting early damage progression. An accurate and precise, damage identification in operating WTB and airplanes can justify longer inspection periods and lower safety factors in the design.

Contents

List of Figures

List of Tables

List of Symbols and Acronyms

Roman letters

U — Strain energy (Nm).
E_{xx} — Elastic modulus (GPa).
G_{12} — Shear modulus (GPa).
I — Moment of inertia (m^4).
N_{ch} — Active LUNA channels (-).
R_s — LUNA spatial resolution (mm).
T — Temperature (K).
w — Displacement in z-axis (mm).
F_{ij} — Fractional strain energy (Nm).
q — Coordinate (-).
x — Span-wise axis (mm).
y — Chord-wise axis (mm).
z — Gravity axis (mm).

Greek letters

Φ — Modal displacement shapes (m).
κ — Modal curvature shapes (m^{-1}).
ϵ — Strain (-).
ν_j — Combined damage index for DIM (-).
ν_{12} — Poisson's ratio (-).
ρ — Density (kg/m^3).
ω — Frequency (Hz).
β_{ij} — Damage index for DIM (-).
λ — Wavelength (m).
ζ — Damping ratio (-).
Ψ — Modal Strain shapes (-).
η — Noise (-).

Sub-indexes

Ny — Nyquist frequency.
n — Eigenvalue/Natural frequency.
max — Maximum frequency.
s — Sampling frequency.
u — Undamaged configuration.
d — Damaged configuration.
i — Modal mode.
j — Coordinate/Gauge.

Acronyms and Abbreviations

DASML — Delft Aerospace Structures and Materials Laboratory.
WTB — Wind turbine blades.
NDT — Non-destructive testing.
VIB — Vibration-based.
MAC — Modal assurance criterion.
COMAC — Coordinate modal assurance criterion.
MCS — Modal curvature shape.
ADM — Absolute differences method.
DMS — Strain gauge.
CDF — Curvature damage factor.
DIM — Damage index method.
MSS — Modal strain shapes.
MSE — Modal strain energy.
CDA — Central difference approximation.
FRF — Frequency response function.
EMA — Experimental modal analysis.
OMA — Operational modal analysis.
ESMA — Experimental strain modal analysis.
LSCF — Least square complex frequency.
CPSD — Cross-Power spectral density.
FEM — Finite element method.
OF — Optical fibers/Fiber optics.
FBG — Fiber Bragg grating.
OFDR — Optical frequency domain reflectometry.
FOSS — Fiber optic strain sensors.
FC — Force cell.
DI — Damage index.
NDI — Normalized damage index.
MPP — Minimum peak prominence.
MPD — Minimum peak distance.
SHM — Structural health monitoring.
DOE — Design of experiments.
GRFP — Glass reinforced fiber polymer.
CFRP — Carbon fiber reinforced polymer.
GLARE — Glass-reinforced fibre metal laminate.
OOP — Out-of-plane.
IP — In-plane.
DMS — Strain gauges.
CFOR — Crest factor optimized random.
MSF — Modal scaling factor.
LR — Location range.

1

Introduction

1.1 Background and motivation

Composite structures combine high stiffness and strength with a relatively low density, compared with traditional metallic structures. This makes composites the preferred material in applications where weight plays an important role. In the aircraft industry, weight savings in the so-called manufacturer's empty weight reduce the fuel consumption and thus the flight's environmental and economical costs [50]. Furthermore, in the wind energy industry, the generated power increases with the square of the rotor-blade diameter [48]. and for this reason, wind turbine blades (WTB) have experienced a significant increase in their dimensions, as displayed in Figure 1.1. However, at the same time, the blade weight scales with the third power of the rotor diameter, which limits the practical length of the blades. An increase in mass leads to higher cyclic bending and torsion loads in the root of the blade, which aggravate the fatigue-related damages, reducing the operational life of the blade [85].

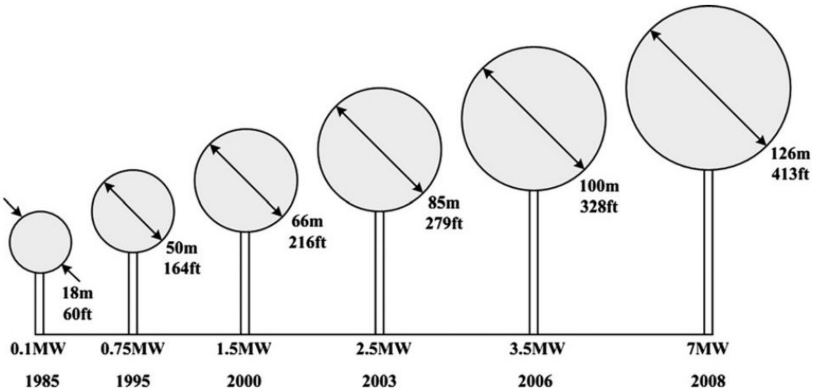

Figure 1.1: Changes in wind turbine power and rotor diameter [85]

One of the biggest disadvantages of composite materials is the unconventional and complex types of damage they exhibit. This makes the repair and maintenance of composite structures different from those of metallic structures. Furthermore, these damage scenarios are often non-visible with optical inspection but still can severely influence the structural performance decreasing its service life. For this reason, periodic inspection and maintenance are essential to guarantee the integrity of a component during its operational life [85]. Structural health monitoring (SHM) technologies are a promising alternative to the current visual inspections, which are often time-consuming, expensive, and require the structure to be readily accessible [52]. SHM, however, involves an integrated sensing network that allows the continuous and online monitoring of a structure performance and degradation [67].

A continuous and accurate estimation of the structure's health might encourage wider time spacing between subsequent inspections and prevent unnecessary replacement of components [10].
The use of SHM technologies will not only give safety benefits and enable new possibilities for maintenance concepts, but it can also have a significant influence on future design concepts, for instance, reducing safety factors [66] . The acquired data and knowledge about recurring damage locations and types might be one of the keys to further development of composite structures in the wind energy and aircraft industry [10].
Despite this, the number of successful practical applications of SHM technologies is still limited mainly as a consequence of the complexity of the composite structures, the variety of possible damage scenarios, and the requirements of high performance for the damage identification methods [52]. The objective of the present chapter is to introduce the concepts of and relation between SHM technologies and large composite structures with applications to aerospace and wind energy.

1.2 Structural health monitoring of composite structures

1.2.1 Composite structures

A composite material is created by a combination of two or more materials to obtain properties that the separate constituent materials cannot achieve [50]. Composite materials consist of a strong tensile-load-carrying material which is typically embedded in a shear-load-carrying material. The stronger material is commonly referred to as reinforcement and the host material is commonly referred to as the matrix. The reinforcement carries the structural load and the matrix acts as a load transfer medium between the reinforcement and maintains the position and orientation of the reinforcement. Composite materials are, therefore, heterogeneous in nature and often anisotropic or orthotropic at the macroscopic level [48].

Continuous fibre-reinforced polymer composites are the most commonly used type of composite materials in primary structures in the aerospace [50] and wind turbine [48] sector. This is due to their high specific strength and stiffness, high resistance against environmental corrosion, and the possibility to tailor the material properties. Moreover, reinforced polymers can be formed into complex shapes, which allows for the manufacturing of complex and large geometries such as curved panels and variable-section spars without the need for further assembly steps. From the aerospace sector, the Airbus A400M Atlas includes composite materials in most of the wings for the first time in history. Making the wing's skin panels the largest ever manufactured out of composite materials [50]. These innovations opened many possibilities for novel designs and set a path for the new generation of aircraft.

Glass fibre reinforced polymers (GFRP) represent the main type of composite when it comes to wind turbine blades. Additionally, there is sandwich core material present in a WTB typically made out of high-density foam or balsa wood [72]. The typical material layout in a WTB section can be seen in figure 1.2.

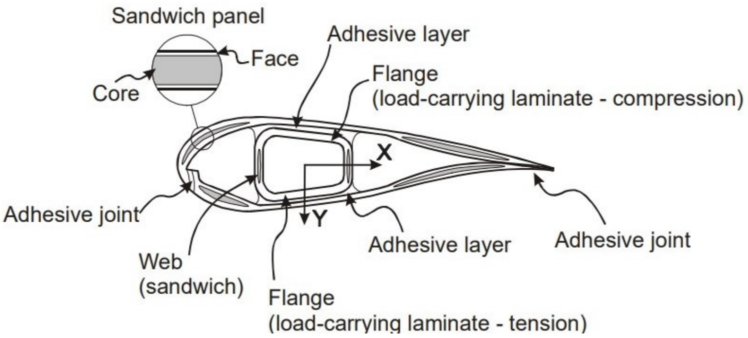

Figure 1.2: Wind turbine blade section and main construction materials [73]

Alternatively, the main trend in the aerospace sector is to use application-specific materials [50]. As a consequence, a wide range of composite materials are present in recent composite-dominated aircraft, from hybrid materials such as glass-reinforced fibre metal laminate (GLARE) for fatigue performance to quartz fibre reinforced plastic for temperature resistance in the aircraft tip [33] (see figure 1.3 for reference).

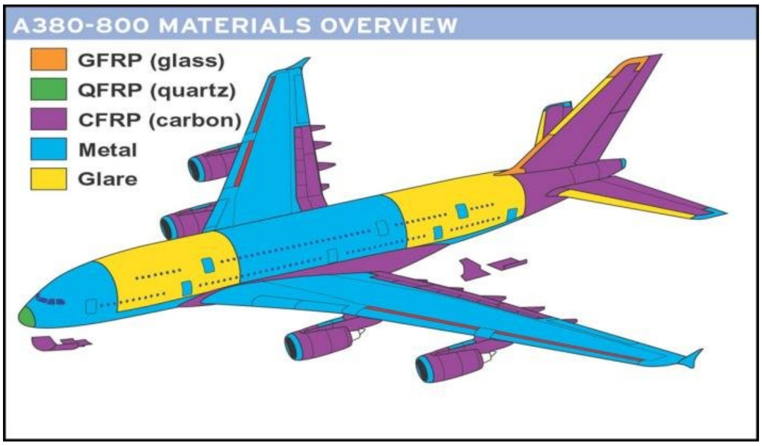

Figure 1.3: A380 main construction materials [33]

Despite the aforementioned advantages of composite structures, there are still many practical issues. The knowledge of fatigue performance of composites is still limited [51, 69] and consequently, the safety factors tend to over-design the components, making composite structures often heavier than the ideal design. This, together with the complex damage types present in composites and their intrinsically heterogeneous properties, creates the need to investigate novel structural health monitoring techniques specially tailored for large composite structures in the aerospace and wind energy sector.

1.2.2 Structural Health monitoring : Classification

SHM systems use in-situ continuous or scheduled measurements and analyses of structural elements under operating conditions [62]. Their main purpose is to bring on-time warnings about accidents or abnormalities and to support a well-founded maintenance and repair program. In the full definition of SHM systems by Li et al. [43], damage diagnosis is considered an essential part of the process. In SHM, damage identification involves the application of global or local non-destructive testing (NDT) methods to determine whether the damage is present in a structure, its location and evaluate the extent of that damage. NDT methods can be classified in multiple ways. The adopted classification in this thesis is based on the cost/benefit analysis approach of Sørensen et al. [74] regarding the use of sensors in wind turbine blades for damage identification. The key parameters in the analysis classification are the capability of the method or sensor to identify and characterize the damage, the minimum detectable damage size, and the ability to detect them through local or global measurements. This section is also based on the classification of NDT methods presented by Ooijevaar [52], which includes considerations about the structure accessibility and data about the undamaged structure, with a focused application in composite structures in the aerospace sector.

Damage identification levels

Rytter [63] classified the SHM damage assessment in the following four levels:

- Level 1: Verification of the presence of damage in the structure.
- Level 2: Determination of the location of the damage.
- Level 3: Estimation of the extent and severity of the damage.
- Level 4: Prediction of the remaining service life of the structure.

Levels 1 to 3 are associated with the damage diagnosis and can be achieved with non-destructive testing techniques. Level 4 is related to damage prognosis and requires analytic, numerical, or data-driven models of fracture mechanics and fatigue evolution to predict the expected residual strength and progression of damage.

Local and global methods

The classification of techniques by either local or global detection is based on the region that can be inspected at once with respect to the overall size of the structure [10]. Local methods focus on a relatively small part of the structure. These methods can detect small damages before they become a hazard to the structural integrity. However, their application involves prior knowledge of the damaged area which is not always available, so this approach requires a pre-evaluation of damage location.

An analysis of the whole structure or large regions of it, is possible through global methods. However, due to the limited spatial resolution and sensitivity to local damages of these methods, early damage identification is not possible, and the identification is restricted to relatively large damage sizes.

The exact damage size that can be achieved by local or global methods depends ultimately on the NDT technique and its accuracy.

Baseline and non-baseline approaches

In damage identification, the response or state of a structure measured before damage onset is considered as the pristine or baseline state [52]. This baseline state can be obtained experimentally (real specimen), numerically (finite element models), or analytically (mathematical models) for a specimen. Differences between the baseline and the current state of the structure provide information about the damage. The baseline state may be determined under different loading or environmental conditions. Some techniques do not require knowledge of the baseline response, as the detection is not based on a comparison of states. Non-baseline approaches are of preference in some applications, as information about the baseline state is often not available in SHM. This is due to the complexity of some mathematical models, the computational cost of numerical analysis in large composite structures, or the lack of experimental tests on the pristine state.
On the other hand, the baseline configuration of the structure (experimental, numerical or analytic) can be used to account for environmental and operational variations by comparing them to the real-application configuration.

Off-line and on-line inspection modes

SHM aims to provide information regarding the integrity of a structure, in near-real-time. The time devoted to sending the information of the structure and analyzing the data, ought to be minimized to reach in-situ monitoring. Nonetheless, this is not always possible due to several reasons. The time it takes to post-process the acquired signals to obtain structural information might be extensive or the procedure may not be automatized at an industrial level at the moment. Moreover, some techniques, such as ultrasounds or X-rays, require direct access to the structure while performing the damage assessment. This does not necessarily mean that the evaluation cannot be done online but that the set-up has to be mounted in the location of the structure or the structure has to be transported to an NDT laboratory. Some techniques, such as structural vibrations or acoustic emissions allow for online remote inspection with data from sensors and actuators previously installed in the structure.

1.2.3 NDT methods for SHM

Table 1.1 presents an overview of the most common NDT techniques applied in the wind energy and aerospace sector. The basic principles of the compared NDT techniques are described in the literature study written before this thesis [71], together with a recap of the most used sensors.

Besides the exposed classification in section 1.2.2, there can be many features that determine the feasibility of a detection technique, but in the end, the correct choice depends on the application and objectives of the damage assessment. Additionally, in practice, more than one inspection method is typically used in wind power plants and airplanes [18]. It is essential to determine the weaknesses and strengths in the practical application of these methods in order to identify the major technological gaps.

NDT technique	SHM Level	Inspected Area	Baseline State	Damage Size	Online Detection
Acoustic Emissions	1,2,(limited)3	locally	No	Small	Yes
Ultrasounds	1,2,3	locally	No	Small	No
Thermography	1,2,(limited)3	globally	Yes	Large	No
X-Radioscopy	1,2,3	locally	No	Small	No
Strain Measurements	1,2,(limited)3	locally-globally	No	Small	Yes
Structural Vibrations	1,2,(limited)3	globally	Yes	Large	Yes

Table 1.1: Overview of the most common NDT technologies [71]

From all the methods, vibration-based (VIB) damage identification methods show high potential for SHM in large composite structures. This is because VIB methods can analyze the health of complex structures globally. The sensors do not need to be placed in the neighbourhood of the damage but in a configuration such that the modal parameters are correctly captured. This often requires preliminary knowledge of the dynamic modes of the blade to optimally place the sensors [21]. In addition, VIB methods do not require the structure to be readily accessible to identify the damage, which is advantageous for offshore wind turbine fields and in-flight monitoring of aircraft.
One of the most noted drawbacks of VIB methods is their limited sensitivity to damages [21]. The size of the detectable damage relative to the structure size is large and additionally, giving an approximation of the damage severity is often not possible. There are multiple methods and detection algorithms in VIB techniques but all of them are incapable of detecting composite-related damages such as cracks or delaminations in the initiation stage. Damages that create a local drop-in stiffness that changes the structure's dynamic properties are relatively large. This is because modal parameters are quantities that characterize the global behaviour of a structure, especially the lower-frequency modes. Despite these shortcomings, VIB methods are continuously improved to reach a higher level of damage identification and to apply to large complex composite structures [82, 13, 88].

1.3 Major technological gaps

This section presents the most important technological gaps found during the literature research on VIB-SHM [71] but can be extended to the mainstream SHM techniques for composite structures:

1. Real-application for composite structures: Most SHM techniques are tested on metallic or concrete structures while the application on composite structures is limited to simple and relatively small beams and plates. For this reason, the test specimens

should be extended to real applications, so that the complexity of composite structures with several components can be studied.

2. Integrated sensing network: SHM systems require the implementation of an embedded or attached sensing network that is capable of continuously rendering information about the structure. The ideal sensor network must have an optimal sensor distribution, have low invasivity in the host structure, and resistance to failure and degradation.
3. Real experimental data: Plenty of novel SHM methods are based on simulated data or are tested in laboratory-controlled conditions. This approach does not consider the real environmental conditions hence it is often incapable of differentiating damage-related changes to environmental changes. In the case of simulated data, the potential effects of experimental noise in damage identification are not even considered. Hence, operational and experimental data should be used to validate and improve SHM methods.
4. Damage identification levels: As presented in table 1.1 most SHM techniques can detect (level 1) and locate (level 2) the damage. However, the damage severity evaluation is not matured in most cases despite its importance for life prognosis and damage evolution prediction.

1.4 General scope of the thesis

In view of the technology gaps identified in the literature review report [71]. The present research aims to aid in the development of SHM techniques based on changes in the structure's dynamic behaviour in the following ways:

1. Testing experimentally on a specimen which is a representative structure for the aerospace or the wind energy sector to study the effect of the composites anisotropy and variability. This thesis is focused on the identification of damages in primary beam-like composite structures, such as wind turbine blades or aircraft wings.
2. Integrating sensor network that does not interfere with the dynamic response of the specimen and that is capable of resisting its operational conditions. This involves using lightweight sensors with a low invasivity in composite materials, and with high resistance to environmental factors such as humidity or thunder (electro-magnetic immunity).
3. Enhancing the damage identification levels and its accuracy for VIB damage detection methods to move towards the development of autonomous SHM systems. Consequently reducing the inspection costs and potentially minimizing the damage diagnosis time.

The above statements represent the starting point for this thesis objectives, the next chapter comprises a literature overview of VIB damage detection methods, together with a short theoretical description of the working principles and recent applications of the FOSS used in this study. Followed by this theoretical background, the general scope of the thesis will be divided into explicit research questions and objectives.

1.5 Report Structure

Besides this introductory chapter, this report contains a total of five chapters, organized in the following way:

- *Chapter 2* consists of the theoretical background of the main concepts necessary for the development of the project: Vibration-based damage identification and principles of strain monitoring with optical fibres sensing technology.
- *Chapter 3* focuses on the validation of the modal parameters obtained from the optical fibre sensing system.
- *Chapter 4* describes the damage detection and location procedure, including the Matlab® built-in algorithm for damage detection and location and the experimental procedure.
- *Chapter 5* critically analyzes if the research questions have been successfully answered and includes a list of recommendations to improve and take this research topic further.

2

Literature study

2.1 Vibration-based damage detection

Structural vibrations are an extensively researched damage identification technique and this is proven by the large variety of detection algorithms and damage indexes proposed in literature since the 70's [17, 1, 49, 21, 13]. This is due to the ability of VIB methods to identify damages globally and continuously during operational conditions with a relatively low number of sensors [63]. However, the detectable damage size, as well as the evaluation of the damage location in these approaches, needs to be improved [21]. Moreover, most of these techniques are based and tested on concrete and metallic structures [44, 6]. These methods have been extended to simple composite beams and stiffened-plates accounting for the effects of orthotropy in damage identification [83, 52, 88]. However, the available literature on VIB methods applied, not only to sub-components, but to complex composite structures is relatively scarce.

Vibration-based or modal-based damage detection methods use changes in the dynamic behaviour of a structure with the objective of detecting, locating and quantifying damages [13]. The presence of a damage in a structure modifies its physical properties, such as stiffness and mass distributions. Stiffness and mass are related to the global dynamic response of the structure thus, damages alter its modal parameters. Changes in these parameters can be used as damage indicators.

The structure can be excited by ambient sources in the case of operational modal analysis (OMA) [5] or by an external source such as a shaker or bonded actuators, in the case of experimental modal analysis (EMA) [68]. Inertia or strain sensors are attached or embedded in the structure to monitor the dynamic response of the system before and after damage [52].

Natural frequency-based methods

The earliest studies on VIB methods focused on natural frequency shifts as a damage indicator. However, despite extensive studies of these methods, the frequency-based methods show several limitations. One of the most restricting ones is that damage is typically a local phenomenon, which means that the changes in strength and stiffness are more severe in the damage neighbourhood. The higher frequency eigenvalues suffer larger shifts than lower ones in presence of local changes, consequently, natural frequencies in the higher frequency range tend to be the most sensitive to the presence of damage. At the same time, these higher modes are the most sensitive to changes in frequency due to environmental and operational conditions. In [21] it was shown that in-situ computed eigenvalue shifts due to operational variations can be in the order of $5\% - 10\%$. Consequently, natural frequencies need to change more than 5% due to damage for it to be detected with confidence with natural frequency-based methods. During the literature review, it was found that most of these methods were tested in lab controlled conditions. So, in order to use these methods for operational applications, the effects of environmental conditions would have to be accounted for in the analysis.

Modal displacement shape-based methods

Modal displacement shapes (MDS) have been researched as a potential method to overcome issues concerning natural frequency-based methods. An extensive comparison of natural frequency and MDS-based damage identification methods has been made by Kim et al. [34], who concluded that MDS methods are more sensitive to damages. This is because displacement eigenvectors (MDS) contain local modal information and they are less sensitive to environmental effects than eigenvalues. However, experimentally obtaining MDS requires a higher number of sensors, as one sensor is enough to determine the natural frequencies but the minimum number of sensors necessary to obtain a MDS depends on the order of the studied mode [68], for instance, five sensors are necessary to obtain the fifth bending mode of a beam. In addition, MDS are more prone to inaccuracies due to noise contamination [21].
The first studies on MDS as damage indicators have used the modal assurance criterion (MAC) to correlate the measured modal shapes from the damaged and undamaged structures. It is also common to find a combination of MAC and coordinate modal assurance criterion (COMAC) with simulated finite element method (FEM) data [16]. COMAC is an indicator of how similar the amplitude and phase of one coordinate are among two computed eigenvectors and it is typically computed for several modes. The common formulations for MAC and COMAC are shown below:

$$MAC(\Phi_u, \Phi_d) = \frac{\mid \Phi_u^T \Phi_d \mid^2}{(\Phi_u^T \Phi_u)(\Phi_d^T \Phi_d)} \tag{2.1}$$

$$COMAC({\Phi^u}_L, {\Phi^d}_L, q) = \frac{\left(\sum_{L=1}^{L_{max}} \mid (\Phi_q^u)_L (\Phi_q^u)_L \mid \right)^2}{\left(\sum_{L=1}^{L_{max}} (\Phi_q^u)_L^2 \right) \left(\sum_{L=1}^{L_{max}} (\Phi_q^d)_L^2 \right)} \tag{2.2}$$

Where Φ represents the modal displacement shape and the superscripts u and d stand for the undamaged and damaged state respectively. In equation 2.2, L stands for the number of analyzed modes and q is the coordinate under study.

Multiple studies have focused on improving and developing methods and algorithms for damage detection based on MDS, by using wavelet transforms [76] or neural networks [44]. Nonetheless, MDS are still not sensitive enough to detect small damages and thus are ineffective for early damage detection. Additionally, the application of this technique in large composite structures is often not viable due to the large number of acceleration sensors necessary to extract high-spatial-resolution MDS [82].

2.1.1 Modal curvature shape-based methods

Higher-order derivatives of MDS can be used as an alternative because they show higher sensitivity to local damages. Rotation and curvature obtained from experimental mode shapes show discontinuities and sudden changes in slope at the damage locations as proved by Roy et al.[61].
Whalen [83] examined the second, third and fourth-order derivatives of MDS on a damaged beam-like structure, concluding that the most efficient MDS derivative is the modal curvature shape (MCS). The first investigation using this approach is from Pandey et al.[53]. The MCS is obtained from MDS using the central difference approximation (CDA), which is expressed as:

$$(\Phi_i)'' = \frac{\Phi_{i+1} - 2\Phi_i + \Phi_{i-1}}{h^2} \tag{2.3}$$

Where h is the element length or distance between measurement points and i stands for the mode number. This method was numerically applied to the first five MDS of a cantilever beam and a simply supported beam. The damage was detected by computing the MAC between the intact and the damaged MCS. Furthermore, the damage was located using the COMAC and the absolute difference method (ADM)[53]. The ADM takes the absolute variation in magnitude between each damaged $\kappa_{ij,damage}$ and undamaged κ_{ij} modal curvature shape as described by equation 2.4, where i stands for mode and j stands for coordinate.

$$\Delta\kappa_{ij} = || \kappa_{ij} | - | \kappa_{ij,damage} || \tag{2.4}$$

Wahab and De Roeck [80] applied this method to a real damage scenario in bridges, evaluating the accuracy of the CDA to compute the MCS. ADM is a simple method that evaluates each mode separately, so another damage index is introduced by Wahab and De Roeck to account for N modes at once; the curvature damage factor (CDF), which is defined as:

$$CDF = \frac{1}{N}\sum_{i=1}^{N} \Delta\kappa_{ij} \tag{2.5}$$

This index proved to concentrate the modal information and account for the dominant modes for damage detection. On the other hand, results showed that the CDA introduces unacceptable levels of numerical error in the MCS. In order to overcome this, an extremely fine spatial resolution for MDS should be used. The investigation also showed that for higher modes, the difference in modal curvatures displays spikes not only at the damage locations but also at random positions which lead to faulty damage detection.

Farrar and Jauregui [22] introduced the damage index method (DIM) and its multi-mode index expressed as:

$$\beta_{ij} = \frac{\left(\left\{\kappa_{ij,damage}\right\}^2 + \sum_{j=1}^{L}\left\{\kappa_{ij,damage}\right\}^2\right)\sum_{j=1}^{L}\left\{\kappa_{ij}\right\}^2}{\left(\left\{\kappa_{ij}\right\}^2 + \sum_{j=1}^{L}\left\{\kappa_{ij}\right\}^2\right)\sum_{j=1}^{L}\left\{\kappa_{ij,damage}\right\}^2} \tag{2.6}$$

$$\nu_j = \sum_i \beta_{ij} \tag{2.7}$$

Where β_{ij} is the damage index for the i^{th} mode at location j, L is the total number of beam elements, and ν_j is the damage index at location j for all the measured modes.
Hamey et al. [30] used several MCS-based indexes, including ADM and DIM, to locate delaminations in a carbon-epoxy composite beam. The research concluded that DIM detects and isolates the damages better than any other index. However, the sizes of the delamination constituted one-eighth of the total beam length. The identification of such a damage size is impractical when extrapolated to real applications such as a WTB. Overall, the modal curvature-based methods have shown great potential for damage detection and location in a high range of applications [6, 41, 82, 84, 87, 88].

Despite these advantages, the numerical errors introduced with the approximation of curvature are the main cause of concern regarding these methods [80] . The vast majority of research about MCS as damage indicators requires robust signal processing techniques to compensate for its susceptibility to noise levels and numerical error caused by second-order differentiation. Modern signal processing techniques such as wavelet transforms have proved to reduce this noise [6, 84, 88]. In addition to this, high-resolution measurement techniques are one of the proposed solutions to enhance damage diagnosis [82].

2.1.2 Strain-based methods

Strain readings have proved to be intrinsically sensitive to local defects [45]. For this reason, experimental strain modal analysis (ESMA) is an effective approach to use experimental data without introducing the numerical error from the derivation of the MDS.
In the Euler-Bernoulli beam theory the relationship between axial strain and curvature along the beam length under pure bending is the following:

$$\epsilon_{xx} = -z\frac{\partial^2 w}{\partial x^2} = z\kappa_x \tag{2.8}$$

Where the x-coordinate is aligned with the beam axis, z is the thickness coordinate, and w is the displacement in the thickness direction.

Accordingly, the modal strain shapes (MSS) can be obtained from strain sensors applied in the top or bottom surfaces of the beam. The modal curvature shapes are directly proportional to these MSS. This approach for beam-like structures can be applied to real large composite structures such as a WTB (see figure 2.1) or slim wings (see figure 2.2) that fit the Euler-Bernoulli assumptions. Strain sensing allows using the aforementioned MCS-based damage identification methods without introducing noise from the second derivation.

Figure 2.1: Haliade-X 12MW 108 meters blade from manufacturer GE renewable energy [23]

Figure 2.2: E1000 composite jet aircraft from manufacturer Epic Aircraft [2]

For beam-like structures, the modal strain energy (MSE) can be directly related to the modal curvature shapes, and thus, to the modal strain shapes. According to the Euler-Bernoulli beam theory, the strain energy U associated with the i_{th} mode shape of an isotropic beam of length l and inertia moment I can be computed as expressed in equation 2.9.

$$U_i = \frac{1}{2}\int_0^l EI\kappa_x^2 dx = \frac{EI}{2}\int_0^l (\Phi_i'')^2 dx \tag{2.9}$$

From this expression, a MSE-based index was considered by Cornwell et al. [12]. The method uses fractional modal strain changes to detect damaged sub-regions by assuming that strain energy remains relatively constant in the region away from the damage.

Assuming a beam with constant flexural stiffness along the length, the damage index is expressed as:

$$\beta_j = \frac{\sum_{i=1}^{m}(F_{ij}^{d} + 1)}{\sum_{i=1}^{m}(F_{ij}^{u} + 1)} \tag{2.10}$$

Where F_{ij} is the fractional strain energy for mode i and element j. The full derivation of the damage index for beam and plate structures can be found in the paper by Cornwell et al. [12]. F_{ij} is defined as:

$$F_{ij} = \frac{U_{i,j}}{U_i} = \frac{\int_j (\kappa_i)^2 dx}{\int_0^{L_{max}} (\kappa_i)^2 dx} \tag{2.11}$$

Where $U_{i,j}$ stands for the modal strain energy of mode i and location j, whereas U_i is the MSE of mode i for the whole beam. The authors also proposed a normalized damage index Z_j in a sub-region of element j, taking the mean $\bar{\beta}$ and standard deviation σ_β of the of values βj for the whole beam.

$$Z_j = \frac{\beta_j - \bar{\beta}}{\sigma_\beta} \tag{2.12}$$

Despite that the efficiency of this method was verified by the authors, the method relies on the assumption of an isotropic beam, which does not capture the orthotropy of composite beams. Nevertheless, this MSE method was tested by Li [45] on a composite beam, it was found to be capable of detecting and locating damages with a 10% stiffness reduction by using only a few modes for the computation.

This MSE method has been modified by several researchers to improve its robustness and performance. It is beyond the scope of this thesis to gather all the variants. The present work focuses on the original and most frequently used version of this MSE damage index for damage identification in a variable stiffness CFRP wing. The applicability of this method to complex composite beam-like structures is investigated during this project.

2.1.3 Conclusions on VIB methods

Given this overview on damage identification methods based on structural vibrations and modal parameter changes, several conclusions can be drawn. Natural frequency and MDS-based methods do not show enough sensitivity to the effect of local damages. This implies that factors such as variability in environmental conditions, or noise pollution reduce the quality of the data to an extent that the detected damage size is too large to be allowed in the structure and thus is more likely to remain undetected until the component is replaced. MCS and MSE show a bigger damage sensitivity but the derivation of these modal parameters based on MDS introduces a large numerical error and propagates noise through the differentiation. A solution for this consists of using strain readings and ESMA instead of displacement data and EMA. Furthermore, the maximum potential of these methods can be reached with the correct use of signal processing algorithms for modal analysis, a proper comparison of the different damage indexes, and an optimal selection of the sensor type and their location on the structure.

2.2 FOSS based on Rayleigh back-scatter

This section of the literature review aims to introduce optical fibres (OF) as an information channel, as well as to explain the working principle of the state-of-the-art fibre optic strain sensing technology used during this project.

2.2.1 Optical fibres as sensors

Optical fibres are a glass (or polymer) wave-guide for light propagation over long distances, with a low signal loss and dissipation [42]. Glass-based OF typically consist of an inner silica-based core ($8 \mu m$ diameter) where light is transmitted. Surrounding the core there is an annular silica-doped cladding ($125 \mu m$ diameter) which is protected by an external coating. The working principle of optical fibres is based on the change in the refractive index between the core and the cladding. Complete reflection of the signal allows the light to travel in the core while guarded by the cladding.

OFs are inherently immune to electromagnetic interference, they can be embedded or bonded to complex composite structures with a near-zero weight penalty and, they do not suffer from fatigue degradation [60]. These characteristics make fibre optic strain sensors ideal for SHM in large composite structures. The most relevant literature in this field is condensed in academic reviews. Ye et al. [86] explained the working principle of several optical sensors, together with their application in the field of civil engineering. Di Sante [15] focused the review on aerospace engineering applications, gathering the sensing techniques applicable to composite structures during flight conditions. A deeper overview of the advantages and applicability of FOSS to composite structures is given by Ramakrishnan et al. [60].

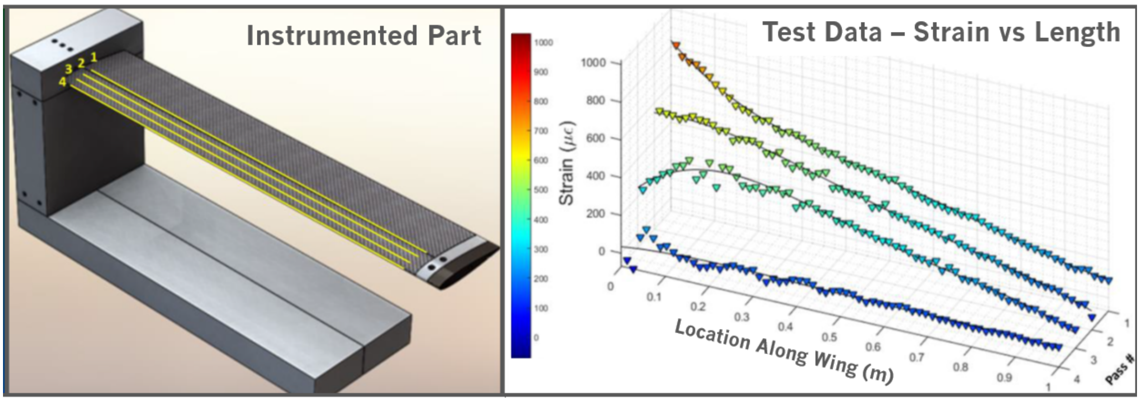

Figure 2.3: Strain readings from 4 distributed FOSS over a CFRP wing. *Picture courtesy of LUNA®* [32]

The most known and widely used FOSS in SHM is fibre Bragg grating (FBG) sensors [18]. Hundreds of FBG sensors can be inscribed in the same OF, also in a multi-core arrangement [64], providing strain readings at those locations of the fibre. However, multiple FBG inscriptions in one fibre raise the cost of the sensing network and additionally, the sensing locations cannot be modified once inscribed in the core [29, 86]. Alternatively, FOSS based on the spectral analysis of backscattered light via an OF, provide quasi-continuously distributed strain readings with tailored spatial resolution. Figure 2.3 shows the quasi-continuous strain field obtained by FOSS with the LUNA ® acquisition system.

The high-spatial-resolution provided by these sensors allows having an unprecedented number of mechanical strain or temperature measurements that, compared to FBG sensors, capture more spatial information from the structure [70]. This characteristic makes these FOSS a promising tool for dynamic damage detection, in fact, diagnosing the health of structures has been one of the driving forces for the development of distributed FOSS [3]. These distributed sensors have the potential to capture MSS with a spatial resolution as fine as 0.65mm, resulting in enhanced damage identification capabilities.

2.2.2 Distributed FOSS: Working principle

Given a light signal travelling through an optical fibre, the light interacting with the glass is partially spread in the form of Rayleigh, Brillouin or Raman back-scattering [3]. Local changes in temperature (T) or elongation (ϵ) in the fibre produce changes in this signal and, parameters such as strain can be extracted from the measured shifts in this signal. Rayleigh, Brillouin and Raman scattering happen at different frequencies and with different intensity [4] as illustrated in Figure 2.4.

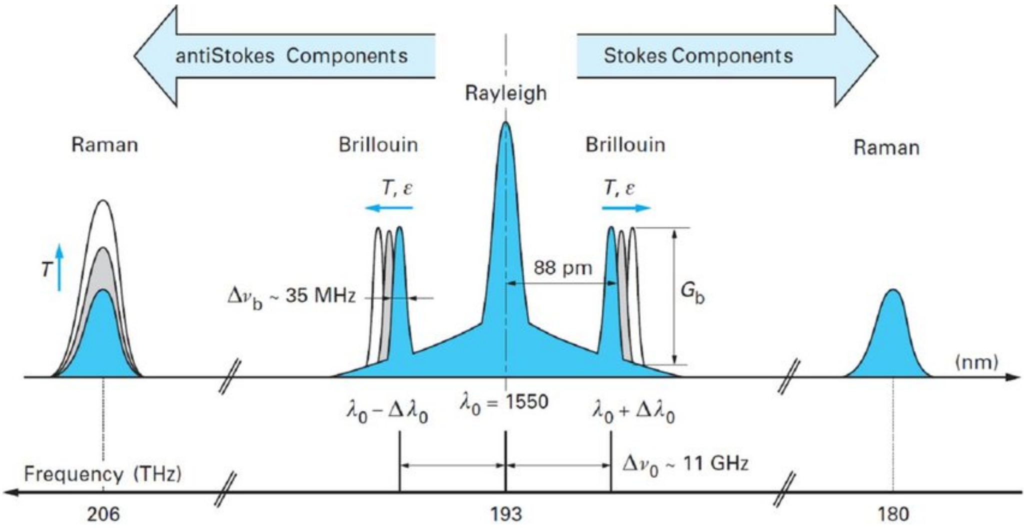

Figure 2.4: Rayleigh, Brillouin and Raman scattering [4]

A light signal of wavelength $\lambda_0 = 1550\ nm$ inside a fibre scatters elastically, resulting in intense Rayleigh back-scattering in the same frequency range. However, the inelastic Brillouin and Raman effects give rise to radiations characterized by a frequency (or wavelength $\Delta\lambda_0$) shift Δv_0.

This frequency shift is in the range of GHz for Brillouin scattering. The shifted frequency bandwidth Δv_b is in the order of MHz. The amplitude of the back-scattered signal remains constant G_b but the wavelength is shifted due to strain and temperature [3].

In the case of Raman scattering, the frequency shift is in the order of THz and changes in temperature modify the amplitude of the back-scattered signal. Bao and Chen [3] recap the key developments in distributed optical sensors. An extended explanation of the working principles of FOSS based on Brillouin and Raman back-scattering is also provided by the authors. The following part of the section is devoted to Rayleigh scatter-based sensors due to the large amount of recent literature exploring the potential of this technique for SHM in the aerospace and wind energy sector [40, 39, 55, 79].

The principles of strain field recognition in optical fibres using Rayleigh back-scattered light were first discussed by Froggatt and Moore [24]. These principles state that optical fibres have an unique spectral pattern of back-scattered reflections, which is due to the micro-scale non-homogeneity in the electromagnetic field through the glass. The non-homogeneous distribution in the OF core is random, which implies that the back-scattered signal is unique to each fibre.

When strain is applied to the optical fibre, its backward propagating Rayleigh scattered light has a time delay compared to the reference (or baseline) spectral pattern. This shift can be interrogated with an interferometric technique called optical frequency domain reflectometry (OFDR), where the optical fibre pattern is divided into different scattering regions from which light data is collected. The interrogation is possible because the spectral reflection signature from any particular location of the fibre uniquely identifies that position. The dimension of the differentiated regions can be customized to obtain the desired spatial resolution in the measurements with the finest resolution limited by noise. These differentiated regions are the sensing locations of this type of sensor and they are referred to as gauges. This technique allows for high-spatial-resolution strain readings in the millimetre scale.

Variations in strain or temperature are calculated by comparing the cross-correlated spectral content between the measured and reference state of a particular gauge. This spectral shift is converted into strain using empirically calibrated coefficients. An exhaustive description of the calibration of the Rayleigh spectral response in an optical fibre is given by Kreger et al. in [38].

2.2.3 Distributed FOSS: Applications in SHM

Several studies have demonstrated the potential of Rayleigh back-scattered signal based sensors for damage identification. A wide review of its applications in the aerospace and wind energy sector can be found in the literature reviews of Guemes et al. [29] and Kreger et al. [39]. However, the approaches described in these papers are reduced to SHM under static loads in scenarios where damage is already located so the distributed FOSS can be positioned close to the damage.

Sierra-Pérez et al. [70] developed a methodology based on real-time static strain measurements on a full-scale WTB to identify damages and non-linearities. The project included several types of strain sensors; strain gauges, FBG sensors and continuously distributed FOSS based on Rayleigh back-scattered signal. The experimental results of the three types of sensors showed good agreement between each other and the detection algorithms based on linear and non-linear principal component analysis were able to detect the pre-introduced damages.

Nevertheless, as mentioned before, the main issue with these detection techniques is that the accuracy and sensibility of the strain readings are dependent on the distance between the damage and the sensor location, such that further away from the sensor the damages remain undetected. This dependency from the distance between the sensor and the damage can potentially be solved using damage identification techniques based on dynamic strain data since VIB methods allow damage monitoring globally in the structure.

The literature on VIB damage identification using distributed FOSS technology is almost non-existing. Cheng et al. [9] used this sensing technique to detect damages on an isotropic beam. One FOSS was glued along the beam span and the damage was simulated by a mass attachment. High-spatial-resolution MSS could be obtained and its information could be used to detect the mass attachment, however, the damage location had unacceptably low accuracy.

To summarize, FOSS based on Rayleigh back-scatter provide continuously distributed strain measurements, which are expected to represent an improvement in the VIB damage identification methods. The dynamic data from these strain sensors is expected to detect local changes in modal curvature shapes and modal strain energy.

2.3 Thesis objective and scope

In section 1.3 the main technological gaps found during the literature study were summarized. Based on those gaps, a general scope was set for the project. In this section, specific research questions and sub-questions are stated, which are inspired by the literature study and the research gaps that were found. These questions define the methodology used throughout the project as well as its main objectives. The main question or objective to answer in this project is:

> ”Can high-spatial-resolution fibre optic strain sensors identify damages in beam-like composite structures?”.

The sub-questions completing the research framework are the following:

Q1 Are modal parameters extracted from high-spatial-resolution fibre optic strain sensors comparable to accelerometers and strain gauges?

Validation of FOSS modal parameters such as the high-spatial-resolution strain shapes will be performed by comparing them with modal results from conventional sensors.

Q2 What is the detectability threshold of the introduced damage?

  - **Q2.1** Can damages be detected and located?
  - **Q2.2** What is the probability of correct damage location over the wing span?
  - **Q2.3** How accurate is the damage location?
  - **Q2.4** How precise is the damage location?
  - **Q2.5** Where is it more likely to obtain a faulty damage location?

  Several damage scenarios must be analyzed in order to answer the above sub-questions. Eighteen mass experiments will be performed in which one location of the wing is perturbed with a mass attachment and the resulting modal parameters are compared to the baseline state.

- **Q3** Which is the most robust damage detection method or index, based on continuous strain readings?
  - **Q3.1** What is the achievable level of damage detection with each studied method?
  - **Q3.2** How precise is each damage index?

  The detection methods and indexes studied are based on MCS and MSE with high-spatial-resolution strain readings. The level of damage detection as stated in 1.2.2, attainable with each method as well as its precision must be found.

- **Q4** What are the effects of noise of FOSS measurements in the damage identification?

  This state-of-the-art sensing technique has many issues regarding data quality and noise levels during static, but especially during dynamic testing. Noise effects are evaluated by comparing real data to strain simulated data from NASTRAN

The above questions are intended to be answered, firstly, by validating the modal data obtained by the distributed FOSS on a composite wing, and secondly, by demonstrating the damage identification potential of these sensors with the aforementioned damage indexes based on MCS and MSE.

3

Validation of FOSS modal parameters

Validation of the FOSS dynamic response is a crucial step in the project, as it determines the degree to which the parameters extracted from this state-of-the-art FOSS technology are an accurate representation of the real structure from the perspective of the intended SHM application. Moreover, the modal parameters resulting from the analysis in this section are used later in the damage detection process.

Dynamic and static measurements are performed on a composite wing specimen to obtain the strain distribution over the wingspan during vibration and static testing. The FOSS test results are compared to those of inertia sensors (typically used in structural dynamics) and strain gauges.

3.1 Specimen under study

The structure investigated in this work is an aero-elastically tailored wing manufactured at the TU Delft Aerospace Structures and Materials Laboratory (DASML)[59]. The wing chord is 250 mm and the half-span extends to 1800 mm. The wing planform with the rib and spar layout is shown in figure 3.1. The different colours indicate the three distinct stiffness regions of the wing surface, the blue one is the closest to the root. The two spars are located at 25 % and 65 % of the wing chord. A total of 13 ribs is used, with spacing increasing from root to tip. The wing is made out of carbon fibre reinforced polymer (CFRP) and the material specification can be found in table 3.1.

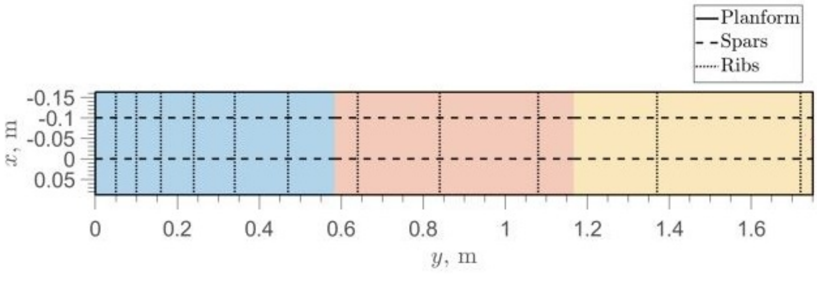

Figure 3.1: Wing layout [59]

The changes in stiffness along the span are due to the distinct layups and thicknesses of the three different regions of each surface. The polar properties of the wing, as well as the thickness of each region, are shown in figures 3.2 and 3.3. The zero-direction in the polar properties is aligned with the wingspan. The transition areas where the polar properties drastically change and composite ply-drops occur are a distinctive feature of the wing. This feature has a great impact on the curvature and strain modal shapes which will be discussed later.

Property	Value
E_{11} (GPa)	148.3
E_{22} (GPa)	9.3
G_{12} (GPa)	4.7
ν_{12} (-)	0.32
ρ (kg/m^3)	1,570

Table 3.1: CFRP properties [59]

Figure 3.2: Wing thickness distribution (mm) [78]

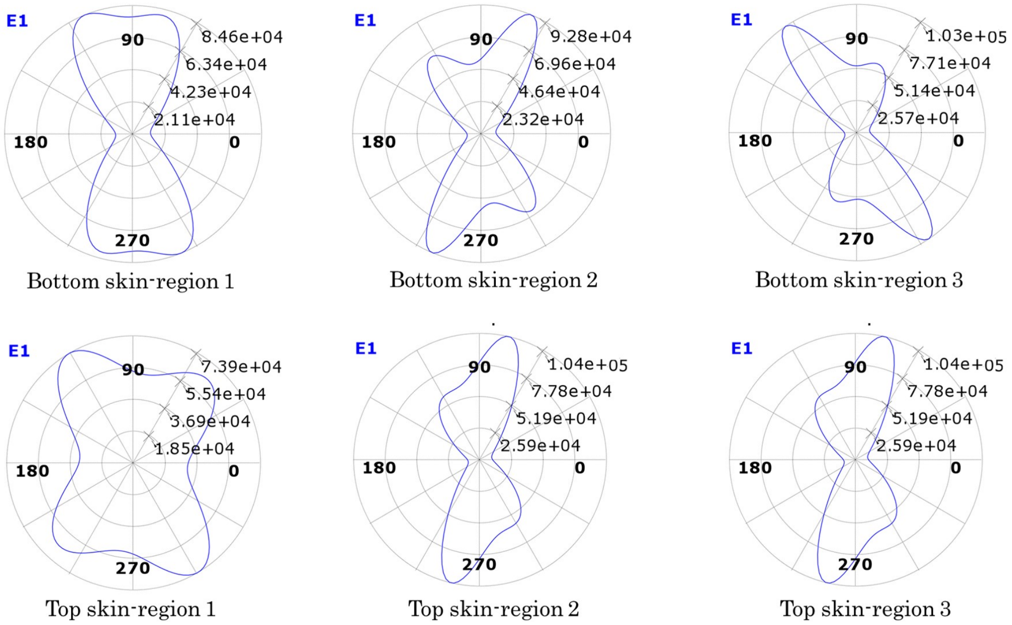

Bottom skin-region 1 Bottom skin-region 2 Bottom skin-region 3

Top skin-region 1 Top skin-region 2 Top skin-region 3

Figure 3.3: Wing polar properties (MPa) per region [59]

3.2 Experimental setup

Dynamic structural system identification is performed in the baseline (or *undamaged*) wing configuration to obtain its dynamic properties and validate the modal parameters obtained from the FOSS.

The wing boundary conditions resemble those of a cantilever beam, where one end is free to vibrate and the root is constrained with a bolted metallic clamp. This configuration can be seen in figure 3.4, where the wing span direction extends from root (left) to tip (right). The clamp is then attached to a 2 ton steel box which can be assumed to be infinitely stiff so the vibrational modes of the box would not affect the wing. This box can be seen in the background of figure 3.5.

Figure 3.4: Wing configuration: Top view

The dynamic tests were carried out with the shaker displayed in figure 3.5. A force cell (FC) was installed to monitor the force levels introduced in the structure and de-couple the shaker vibrations from the wing response. The excitation point was close to the leading edge, 225 mm away from the encased root of the wing.

The used acquisition systems for the vibration tests are the imc ® data analysis framework, which can be seen in the bottom part of figure 3.6 and the LUNA ® ODiSI 6100, which can be seen in the top part of figure 3.6. The imc ® system allows, among other functionalities, to load, synthesize, and output signals. It is also capable of acquiring signals as inputs, in the case of this research, the system acquires the sensor signals from the accelerometers, strain gauges and a force cell.

The LUNA ® ODiSI 6100 measurement system consists of a mainframe with the capacity to connect eight optical sensors as a multi-channel system. The channel of interest is connected to a 50 meters rugged stand-off optical cable that connects the ODiSI 6100 interrogator and the remote module (figure 3.6). The remote module is connected to the corresponding FOSS with the aid of a MU/LC optical connector. The LUNA ® ODiSI 6100 has a relatively low sampling frequency (ω_s) compared to the imc ® system.

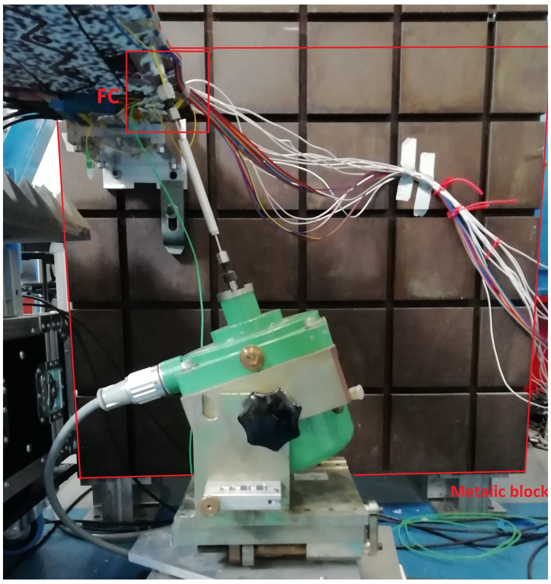

Figure 3.5: Shaker, force cell, and metallic block

Figure 3.6: Top: the LUNA® mainframe and remote module. Bottom: the imc ® mainframe

The maximum sampling rate of the LUNA ® system is $\omega_{max} = 250Hz$ and it is reduced depending on the number of simultaneous measuring channels (N_{ch}), and on the selected spatial resolution (R_s). The sampling frequency is reduced according to equation below:

$$\omega_s(N_{ch}, R_s) = \frac{1}{2^{N_{ch}-1} \cdot 2^{R_s-1}} \omega_{max} \tag{3.1}$$

There are five possible values for spatial resolution available with this optical system, ranging between $0.65mm$ and $5.2mm$. The selected spatial resolution during the study is $2.6mm$ which is the finest resolution possible with a sampling rate of 250Hz ($R_s = 1$). The sampling rate is chosen so that the maximum number of modes can be accurately extracted from the structure. This also means that all experiments have to be repeated four times to acquire data from each FOSS separately ($N_{ch} = 1$).

This state-of-the-art measurement system has great potential but also faces great challenges. A summary of the main issues discovered about the LUNA ® system can be found in Appendix B. The most relevant ones are the presence of Not-a-Number (NaN) entries in the strain measurements and the irregular sampling rate of the system. A description of the adopted solutions for these problems is also given in the same appendix.

3.2.1 Sensing network

One of the main objectives of this thesis resides in exploring the damage detection capabilities of high-spatial-resolution FOSS dynamic data. In order to do so, the FOSS modal data obtained in each dynamic and static test is validated with accelerometers and strain gauges.

Accelerometers are commonly used and studied for dynamic identification [68, 19, 5], thus they are a reliable tool to compare modal parameters such as natural frequencies and damping ratios. The most used accelerometers in the aerospace and wind-energy industry are uni-axial and tri-axial, high-sensitivity, capacitive sensors, given that the structural vibrations of interest are in the frequency range of $10^0 - 10^3$ Hz [76].

Eleven tri-axial accelerometers were attached to the leading edge of the wing. In addition, eleven uni-axial (Z-direction) accelerometers were attached in the trailing edge in the same span-wise location as the tri-axial accelerometers. The spacing between the accelerometers is 175 mm. This sensor distribution allows to capture bending, torsion, and combined modes, which were expected to be the modes in the frequency range of study. The measured magnitude in the case of accelerometers is the acceleration that can be converted to displacement by means of a double integration in the frequency domain and then the displacement modal shapes can be extracted.

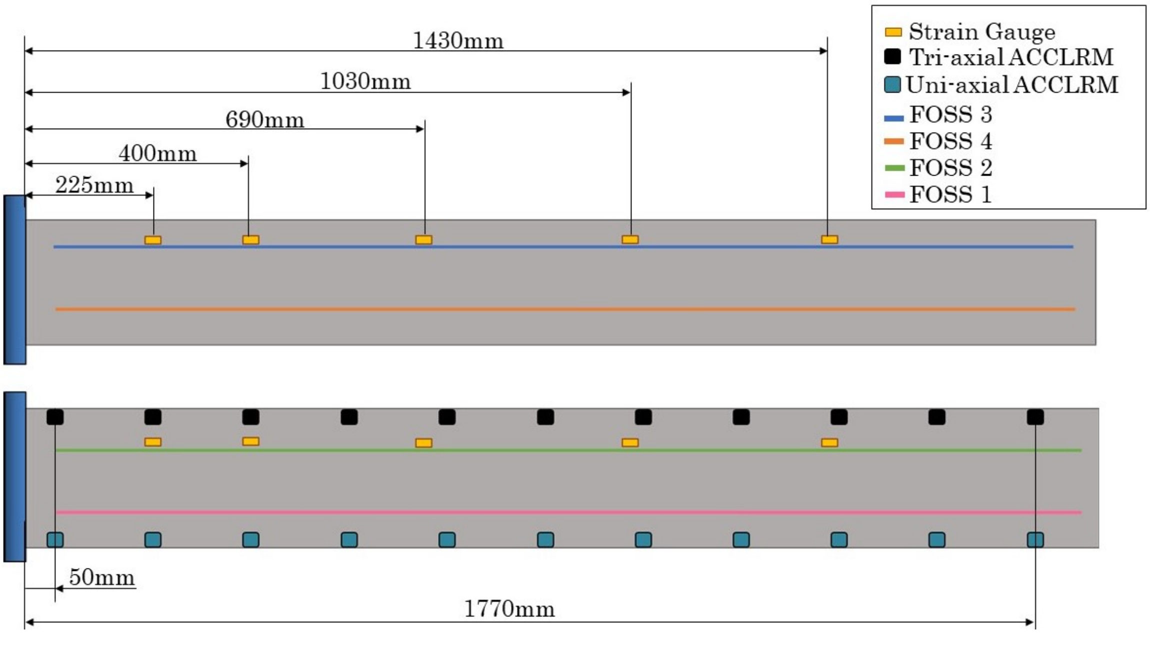

Figure 3.7: Sensing network of CFRP wing

However, FOSS measures strain and, therefore, strain modal shapes are extracted. In order to compare the FOSS strain levels and the strain modal shapes, 10 strain gauges have been added 1 cm from the FOSS towards the leading edge. The five DMS were bonded in each surface with the spacing progressively increasing from root to tip, as can be seen in figure 3.7. This spacing is chosen because the root is under larger strains and has higher density of components such as ribs. The top and bottom row of DMS are bonded at the same span position enabling the neutral axis to be computed (see Appendix C for reference).

Finally, four FOSS were bonded to the wing in the span-wise direction as shown in figure 3.7. The different OF-sensor lengths vary between 2.5 m and 2.1 m but the effective bond length is 1.7 m in all four cases. Given a spatial resolution of 2.6 mm, around 650 sensing gauges per FOSS are investigated.
As can be seen in figure 3.7, the FOSS are numbered from one to four. These identifications are used throughout the report. All four fibres are located right on top or below the spars, therefore FOSS1 and FOSS4 share the same position chord-wise. The same hold for FOSS2 and FOSS3. The chosen OF-sensor arrangement allows to compute the neutral axis of the wing, obtain quasi-continuous strain shapes along the span and reconstruct the displacement field using Ko's displacement theory [36]. The bonding methodology and materials for all three types of sensors are described in appendix A.

3.3 Experimental modal analysis

The wing was excited with a crest factor optimized random (CFOR) signal for 200 seconds, which is considered long enough to excite correctly all the frequencies and to fully dampen the transient response. In general, a signal with a high crest factor increases the probability of non-linear responses from the structure. The aim is often to minimize the crest factor of the signal [78]. The CF used during the experiments is 1.6, given that the minimum value is 1.41 for a pure sine.

The frequency range of the excitation signal was from 1 Hz to 150 Hz, however, only modes below the Nyquist frequency can be analyzed. This frequency was found to be $\omega_{Ny} = 97.65Hz$ as explained in appendix B due to the non-uniform time-stamps acquired by the LUNA ® system.
Four modes were detected in the described frequency range from 1 Hz to 97.65 Hz. These are the first, second, and third out-of-plane (OOP) bending modes and the first in-plane (IP) bending mode.

Experimental modal analysis is performed on the accelerometer data to extract the modal parameters of the structure [68]. The frequency response functions (FRFs) for the accelerometer signals were computed by referencing the input signal from the force cell. With this, the well-known least-squares complex frequency-domain (LSCF) [54] was used to compute the natural frequencies, modal displacement shapes and damping values.

The results for the modal displacement shapes of the wing are shown in figures 3.8, 3.9, 3.10, and 3.11.

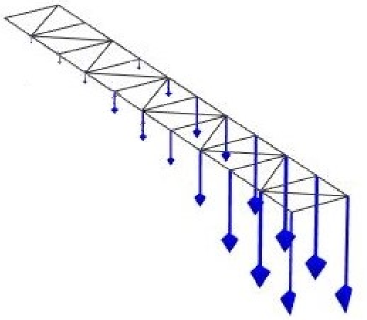

Figure 3.8: MDS: First OOP bending

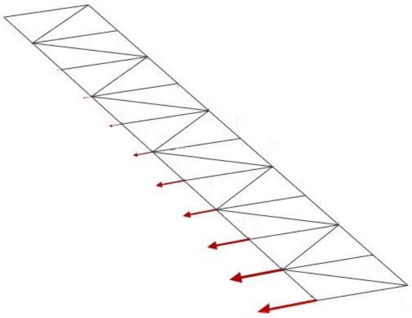

Figure 3.9: MDS: First IP bending

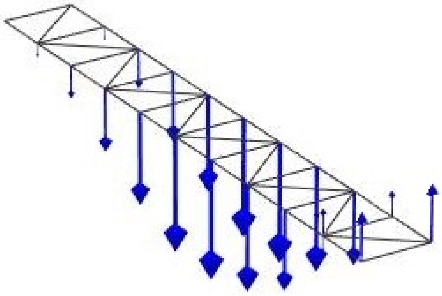

Figure 3.10: MDS: Second OOP bending

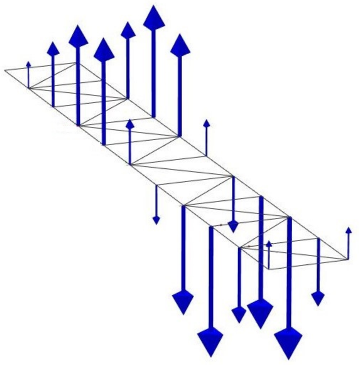

Figure 3.11: MDS: Third OOP bending

The natural frequencies and damping ratios for the first four modes are given in table 3.2 together with the position along the span of the absolute local maximums and positions of the nodes (null displacement) of the MDS. These values are obtained by fitting a polynomial to the discrete values of the displacement shape.

Mode	Natural frequency	Damping ratio	Local.Max. in MDS	Node in MDS
	(Hz)	(-)	(mm)	(mm)
1^{st} OOP	3.22	0.008	1800	0
2^{nd} OOP	19.62	0.021	932, 1800	0, 1495
1^{st} IP	25.51	0.013	1800	0
3^{rd} OOP	54.53	0.028	415, 1310, 1800	0, 965, 1630

Table 3.2: Modal parameters from accelerometers

3.3.1 Experimental strain modal analysis

Strain gauges are typically used in static and fatigue tests on wind turbine blades as a part of its certification process [67, 72, 70]. Besides this, their application has been extended to modal parameter identification using experimental strain modal analysis [27, 58, 7]. A comparison between EMA and ESMA is provided by Kranjc et al.[37] where accelerometers and strain gauges were used to obtain the modal parameters of a free-free supported beam. The results proved that the accuracy in the modal parameter estimation with strain sensors is comparable to the accuracy of classic EMA.

In this project, experimental strain modal analysis was similarly applied on strain transfer functions to transfer functions calculated from acceleration signals. Regarding the LUNA ® strain data, the inconsistent sampling frequency during measurements makes synchronization between FOSS data and any imc ® external analog signals not possible (see Appendix B for reference to these problems). For this reason, strain cross-power spectral densities (CPSD) were used to obtain the frequency responses of the DMS and the FOSS [28]. One sensing gauge in each FOSS was referenced for the analysis. This gauge was chosen such that it has a significant spectral amplitude in all four analyzed modes. The eigenvalues and eigenvectors were also estimated using the LSCF method. The stabilization diagram obtained from the strain modal analysis is shown in figure 3.12.

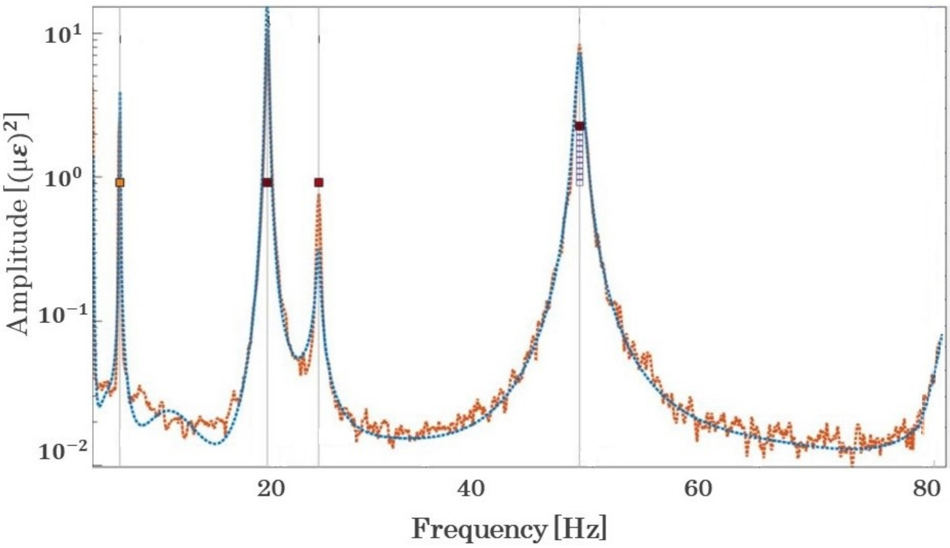

Figure 3.12: Stabilization diagram from ESMA in FOSS

As expected, four modes are observed in the studied frequency range; $1^{st}OOP$, $1^{st}IP$, $2^{nd}OOP$, and $3^{nd}OOP$ pure bending modes. A comparison between FOSS ω_n and DMS ω_n is gathered in table 3.3. The presented FOSS ω_n are obtained as an average of the four FOSS in seven different dynamic tests performed at different days and times. The relative error between FOSS and DMS resonance peaks in the seven averaged measurements is also included in table 3.3.

The natural frequency values obtained with ESMA and EMA (see table 3.2) differ. In the case of EMA, the shaker can be de-coupled from the wing using the force cell, whereas in the case of the performed ESMA the obtained modal parameters include the stiffness and mass modal properties from the shaker.

Mode	Natural frequency FOSS (Hz)	Natural frequency DMS (Hz)	Relative error (%)
1^{st} OOP	3.18	3.11	2.25
2^{nd} OOP	19.09	19.02	0.37
1^{st} IP	24.12	24.50	1.55
3^{rd} OOP	52.69	52.24	0.86

Table 3.3: Natural frequencies and error from strain data

The validation of the eigenvalues obtained with this FOSS technology is satisfactory. The values of ω_n in the EMA and ESMA are comparable and the error in the ESMA between DMS and FOSS is low enough to consider the natural frequencies extracted from FOSS as valid for further use.

For the validation of the eigenvectors obtained from the FOSS, a graphical comparison between FOSS and DMS strain shapes is presented in figures 3.13, 3.14 and 3.15, where the MSS are normalized between -1 and 1.

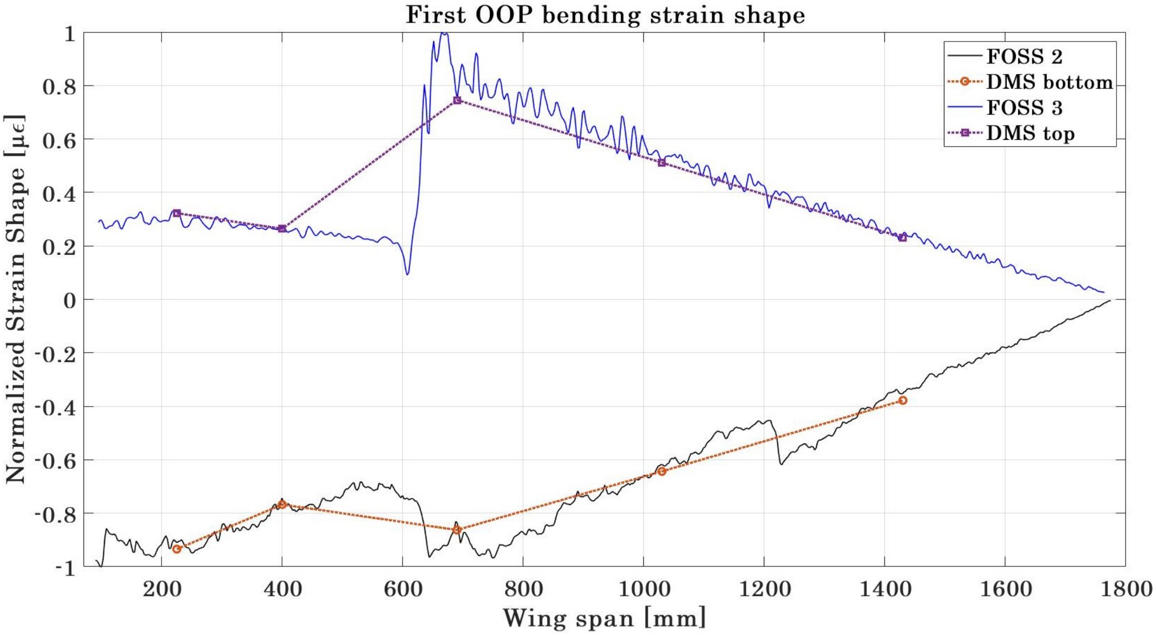

Figure 3.13: MSS from leading edge sensors: First mode

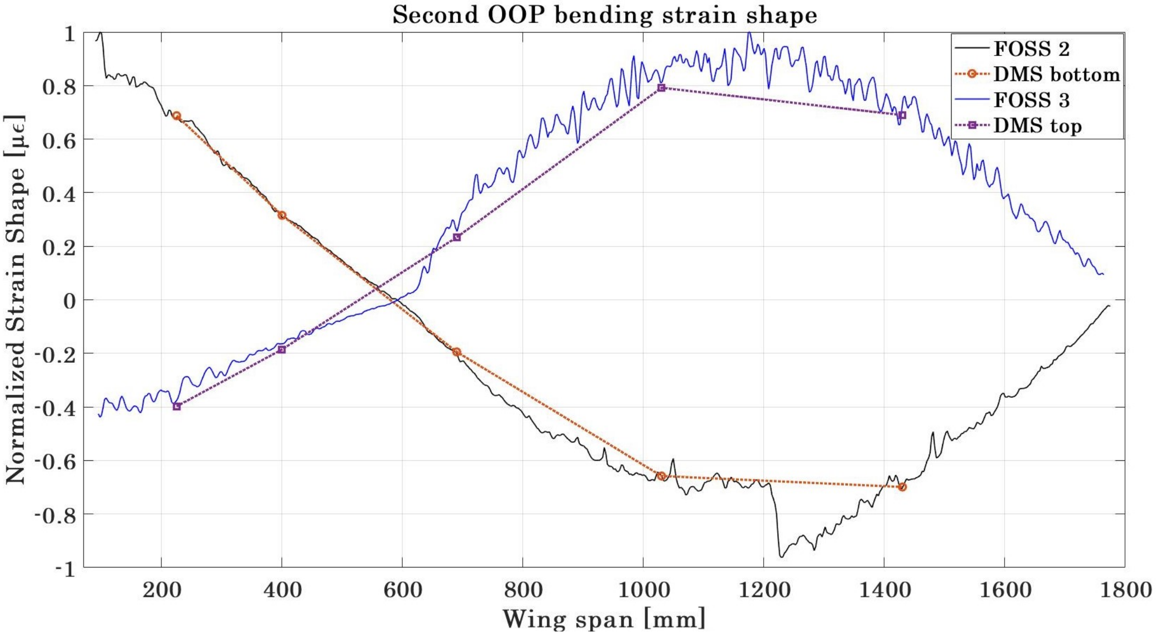

Figure 3.14: MSS from leading edge sensors: Second mode

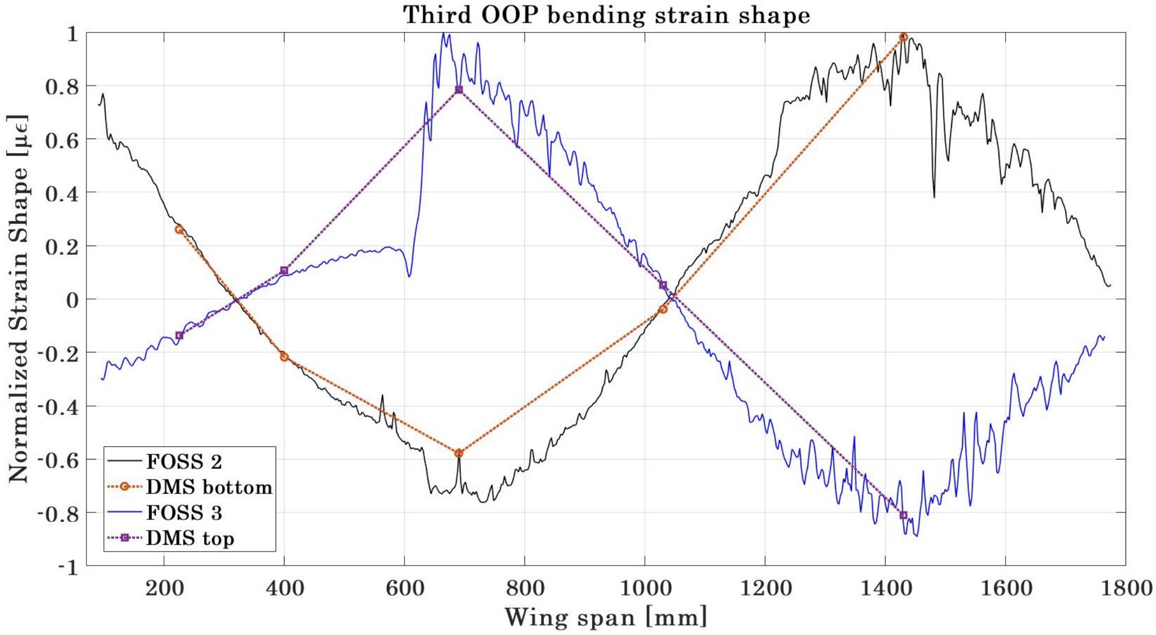

Figure 3.15: MSS from leading edge sensors: Third mode

The strain shape for the first in-plane bending mode $\omega_n = 25.5Hz$ is not presented in the report because of its poor quality. The poor quality is because the measured strain in the IP direction are much lower than those in the OOP direction since the IP bending stiffness of the wing is much higher than the OOP one. Moreover, the first IP resonance is rather close to the second OOP mode which has higher amplitude strains. This fact makes it difficult to de-couple the strain contribution from one mode and the other. Since the 2nd OOP is the dominating mode, the obtained 1st IP MSS is corrupted by it.

The approximate locations of the absolute local maximums and node positions for the MSS are given in the table 3.4.

Mode	Local.Max. in MSS (mm)	Node in MSS (mm)
$1^{st}\ OOP$	0	1800
$2^{nd}\ OOP$	0, 1250	600, 1800
$3^{rd}\ OOP$	0, 725, 1450	330, 1050, 1800

Table 3.4: FOSS MSS maximums and nodes

It is interesting to compare table 3.2 and table 3.4 since the local maximums of the MSS are relatively close to the nodal positions of the MDS, and vice-versa, meaning that the locations with small or no displacement are the most strained ones.

3.4 Validation of MSS by means of static test

The damage detection technique explored in this thesis relies on the modal strain shapes and their derived magnitudes, such as modal curvature shapes and modal strain energy, to locate damages. For this reason, it is necessary to validate the MSS. In the above section, it is shown how the DMS MSS have a good correspondence with the FOSS MSS. However, the spatial resolution of the FOSS is two orders of magnitude finer than that of the DMS, this means that the DMS data can be used to check the general trend of the MSS but not to discard errors in the FOSS MSS.

On account of that, the validation procedure must ensure that the MSS obtained from the EMA of the FOSS vibration data are indeed a manifestation of the structural features of the variable-stiffness wing. Static tests have been performed on the wing to confirm that the variations of strain along the wingspan are not due to noise created during the dynamic excitation or errors introduced during the modal analysis.

Three static tests were performed, one representing each OOP bending mode. The first mode was obtained with a point load located at the tip of the wing as figure 3.16 shows. In the case of the second and third mode, two and three-point bending tests were performed, where the load is introduced in the local maximums according to table 3.2.

However, the results for the second and third bending mode are not conclusive so only the results for the first mode are discussed. The modal shapes for the second and third

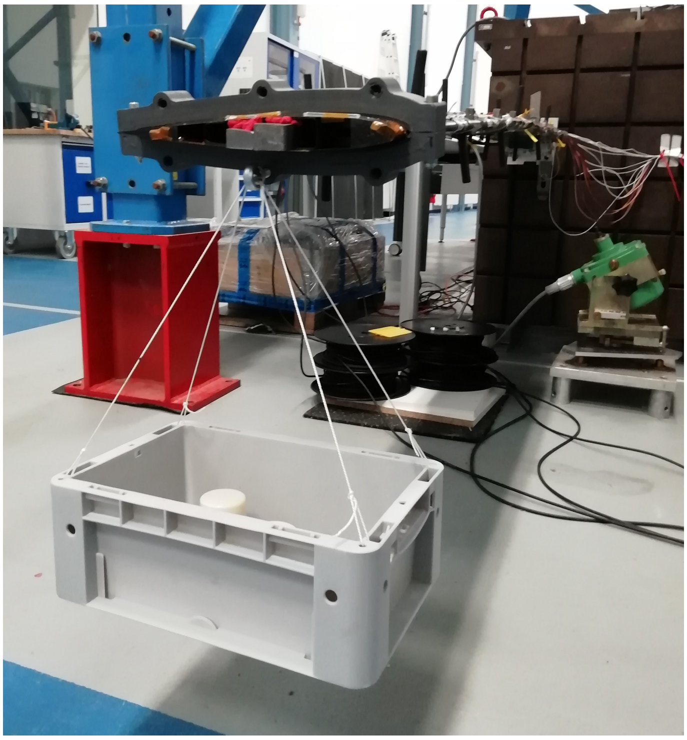

Figure 3.16: Tip load introduction with attachment for static test

bending modes did not correspond to the ones obtained with the static testing because the higher order modal shapes are more difficult to capture statically. The MAC between modal and static shapes for these two modes mode are as low as 0.5, so it is concluded that the shapes are not comparable.

In order to introduce the tip load during the test, an attachment for the wing is designed and produced by means of additive manufacturing. The main purposes of this attachment are to distribute the tip load along the wing chord to avoid twisting and to ensure that the load introduction does not lead to material failure in the wing. More information about the attachment and the static testing can be found in appendix C.

The first OOP bending MSS obtained from vibration testing was compared with the results from the static test shown in figure 3.16. The strain readings are scaled with the modal scaling factor (MSF) and normalized between 0 and 1 in order to have visually comparable results. The MSF is defined by Ewins [19] as the complex or real number that relates two or more modal shapes. MSF is used to normalize all modal shapes of the same vibrational mode to a common level for comparison and subsequent manipulations.
The MSF between two modal strain shapes Ψ_s and Ψ_d is defined as:

$$MSF(s,d) = \frac{\sum_{j=1}^{N} \Psi_{si} \Psi_{dj}^{*}}{\sum_{j=1}^{N} \Psi_{dj} \Psi_{dj}^{*}} \tag{3.2}$$

Where N is the number of degrees-of-freedom for each MSS and superscript * indicates the complex conjugate of the shapes.

In addition to this, the MAC between modal and static shapes is computed for each FOSS and displayed under the legend of figures 3.17, 3.18, 3.19, and 3.20.

The results from the static tests show high correspondence between static and dynamic experiments, as can be seen by the high MAC values, leading to the conclusion that the strain variations captured along the wingspan by the high-spatial-resolution optical sensors belong to real features of the composite structure. The large peaks or strain discontinuities present in the MSS can be used to locate the ply-drops.

For FOSS 1 and 2, two ply-drops are visible at around 600 and 1200 mm from the wing root. In the case of FOSS 3 and 4, there is only one ply-drop which is located at around 600 mm from the root. Even the local effect of the attachment can be seen at the end of the static shapes, at around 1770 mm.

The above-mentioned result reinforces the hypothesis that this FOSS technology is sensitive to local stiffness and mass changes and therefore suited for SHM. It is also possible that the strain changes observed at the ply-drop positions as well as the overall strain distribution span-wise are created by the LUNA® system when transforming light readings into strain and therefore is related to errors in the acquisition system itself. It was not possible to test this second hypothesis because of the encoded binary format in which the raw LUNA® data is given before transforming it to strain.

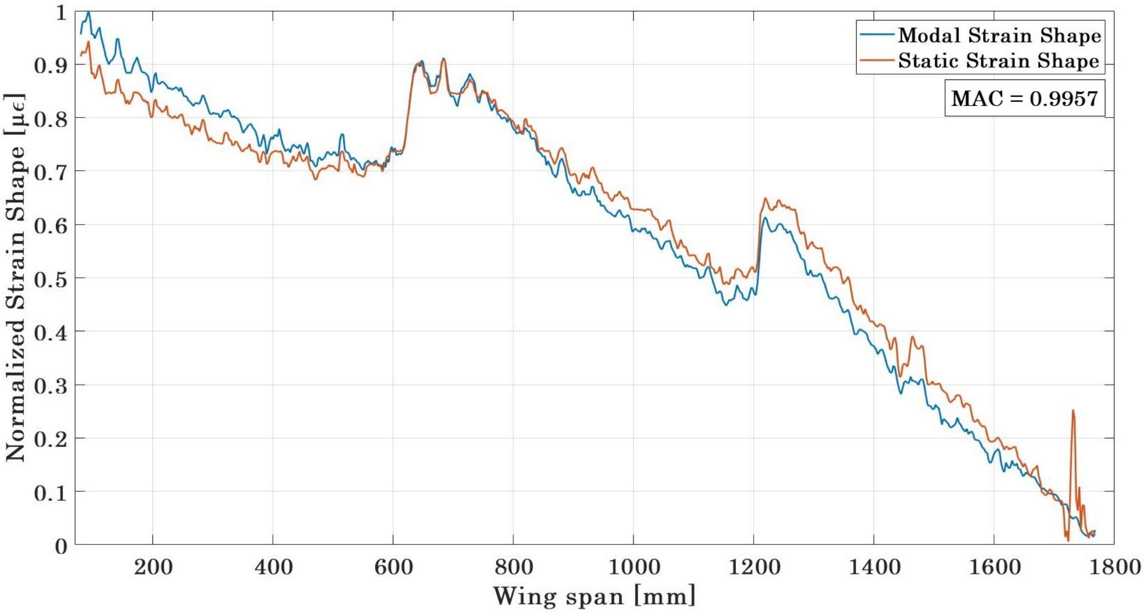

Figure 3.17: Modal and static strain shape comparison for FOSS1

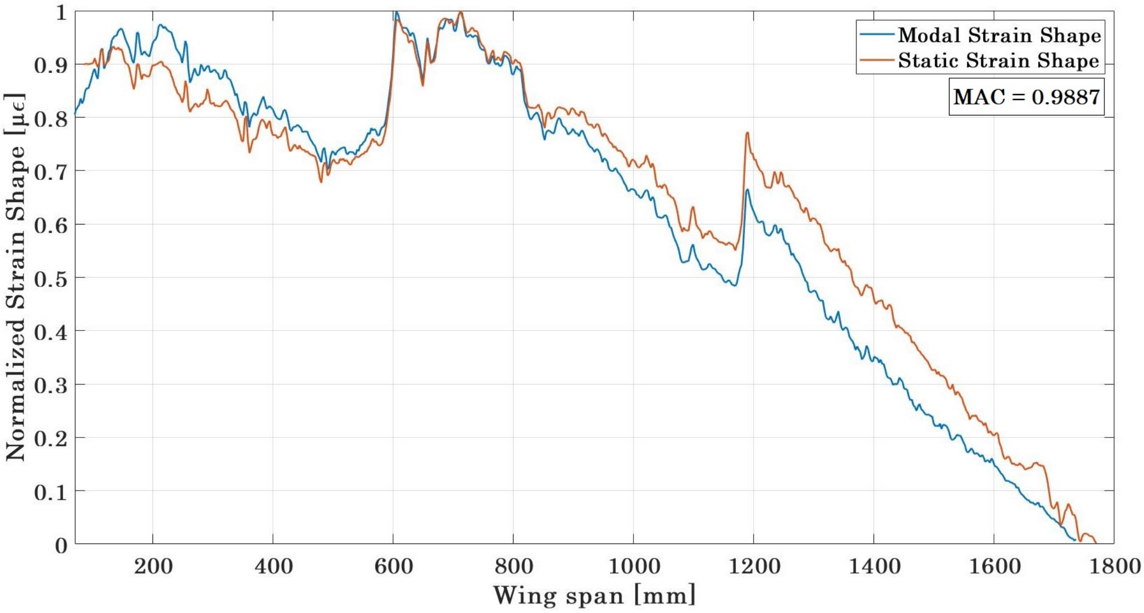

Figure 3.18: Modal and static strain shape comparison for FOSS2

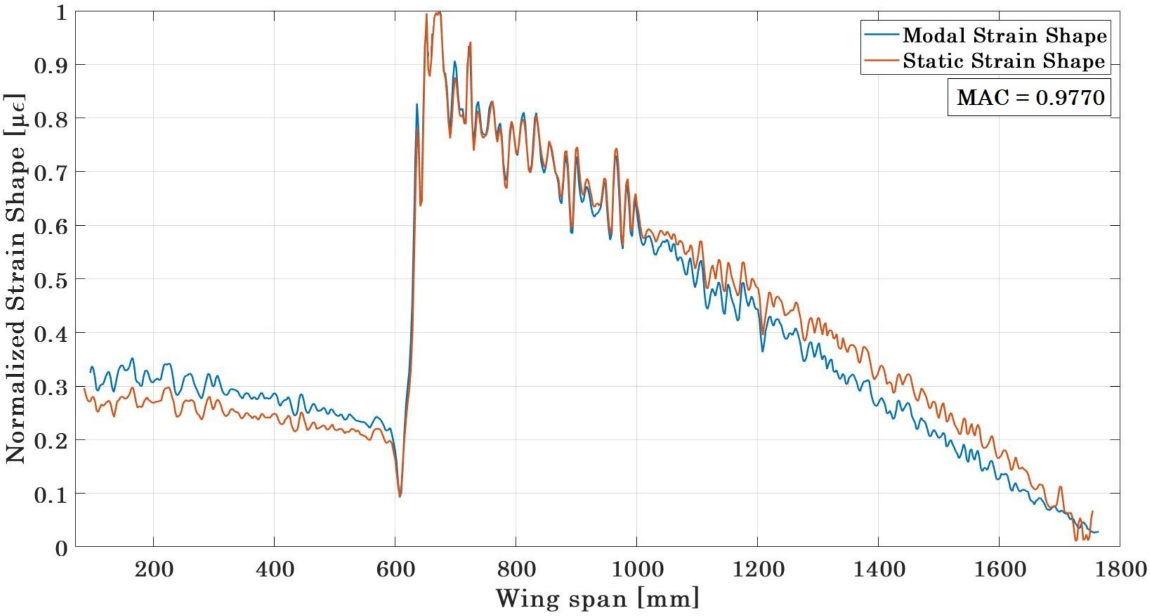

Figure 3.19: Modal and static strain shape comparison for FOSS3

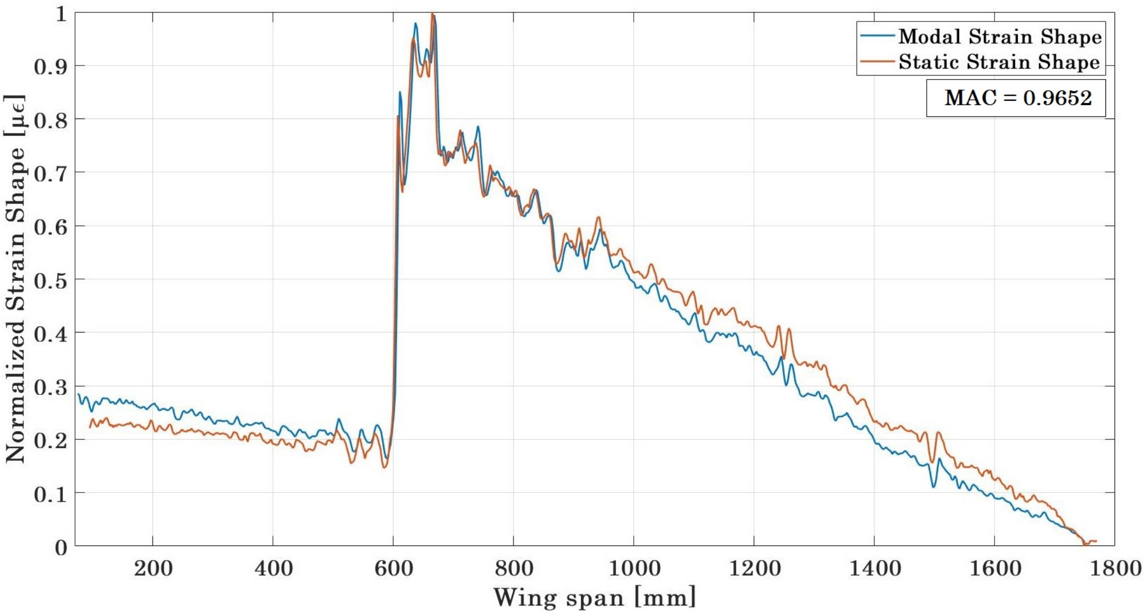

Figure 3.20: Modal and static strain shape comparison for FOSS4

3.5 Repeatability of the testing set-up

The final step for validation of the used FOSS as dynamic continuous strain sensors consists of analyzing the potential error and noise from the experimental set-up. The repeatability of the testing approach and experimental set-up is studied by performing seven dynamic tests at different days and times. The resulting variations in the measured spectral response, natural frequencies and strain shapes give an indication of the repeatability of the testing method. Figure 3.21 shows the frequency response of one sensing gauge in FOSS1 for all seven measurements.

The standard deviation over the mean of the measured peak values is shown in table 3.5 for all four FOSS and all three OOP bending modes. The average standard deviation over all peaks is 0.46%. The largest standard deviation is found for mode 1, with an average natural frequency of 3.18 Hz and an average standard deviation of 1.32%. This mode shows the largest deviation because it is excited less, the amplitudes of strain captured in this mode are relatively lower than the rest and thus the signal to noise ratio is lower than for the higher modes. The repeatability on the MSS is assessed in terms of the modal assurance criterion, standard deviation over mean strain measurement per gauge, and relative error between repetitions.
The MSS are computed for each repetition and the results from FOSS1 and FOSS4 (trailing edge spar) in all seven cases are scaled with the MSF and plotted for the second OOP bending mode (for modes 1 and 3 see appendix D).

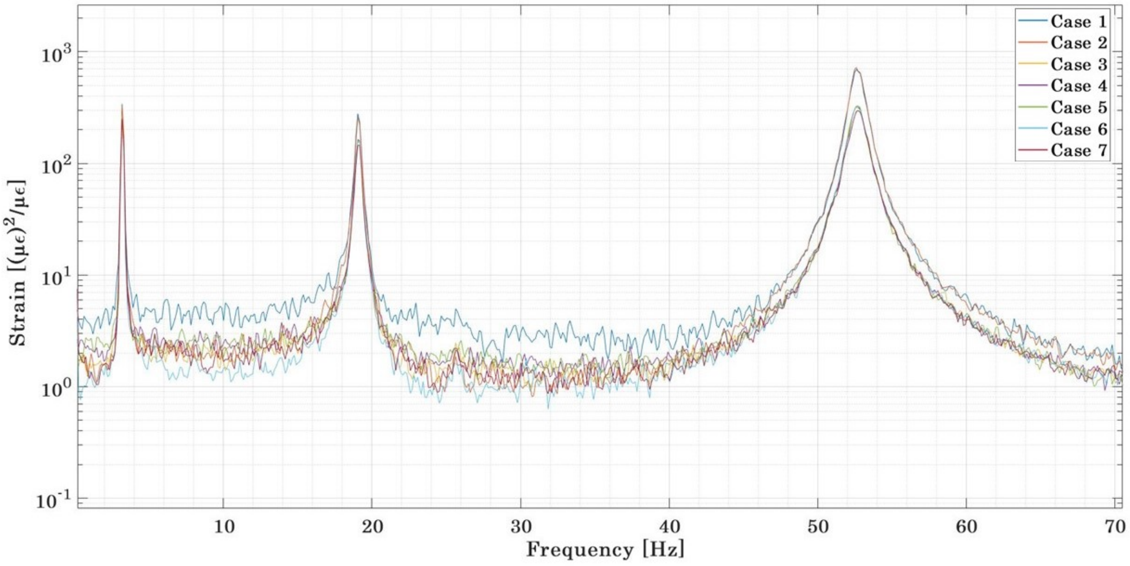

Figure 3.21: Repeatability of the spectra peaks from seven case measurements

	FOSS 1	FOSS 2	FOSS 3	FOSS 4
1^{st} OOP	1.52%	1.40%	1.31%	1.03%
2^{nd} OOP	0.03%	0.03%	0.05%	0.03%
3^{rd} OOP	0.02%	0.02%	0.04%	0.03%

Table 3.5: Standard deviation over mean peak value

The MAC is computed for all seven repetitions, modes, and fibres. The minimum MAC value obtained in the analysis is 0.987, with the average MAC value being 0.998.

The standard deviation and relative error for each sensing gauge of FOSS1 in the three bending modes are shown in figures 3.23, 3.24, and 3.25. The graphs for the remainder of fibres can be found in Appendix D.

Figure 3.23 shows that the error and standard deviation are higher at the tip of the wing. These distributions are partially a consequence of a known feature of the LUNA ® measurement system and is because the data quality at the end of any FOSS is lower due to the weakening in the intensity of the back-scattered signal. As a consequence, the presence of 'NaN' measurements increases in this region. Another reason for this distribution is that the wing tip is the less strained region of the wing causing the measured strains to be in the same order of magnitude as the noise measured by LUNA, which is $\eta = \pm 5\mu\epsilon$. The effect of this low signal to noise ratio is visible in the increase of standard deviation over mean strain from root to tip.

Figures 3.24 and 3.25 show one and two large peaks in the error and standard deviation,

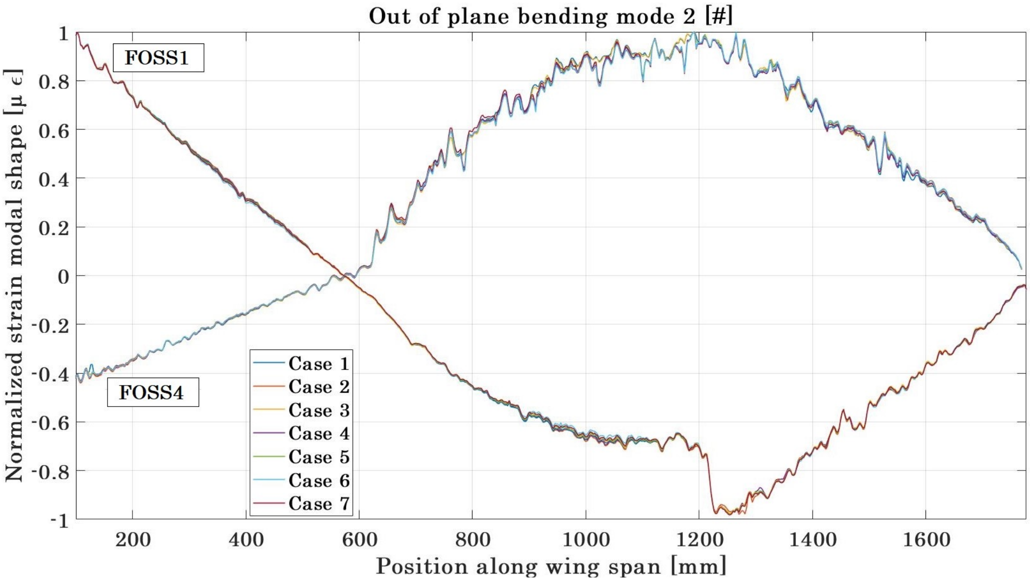

Figure 3.22: Repeatability of MSS from seven case measurements: Mode 2, FOSS 1 and 4

respectively. The location of these peaks over the wingspan corresponds almost exactly to the node positions of the MSS, which have been given in table 3.4. The large values for standard deviation in these nodal positions might lead to a faulty detection of damages in those locations. In order to avoid this faulty detection, the above error functions are considered in the damage location algorithm as will be explained in chapter 4.

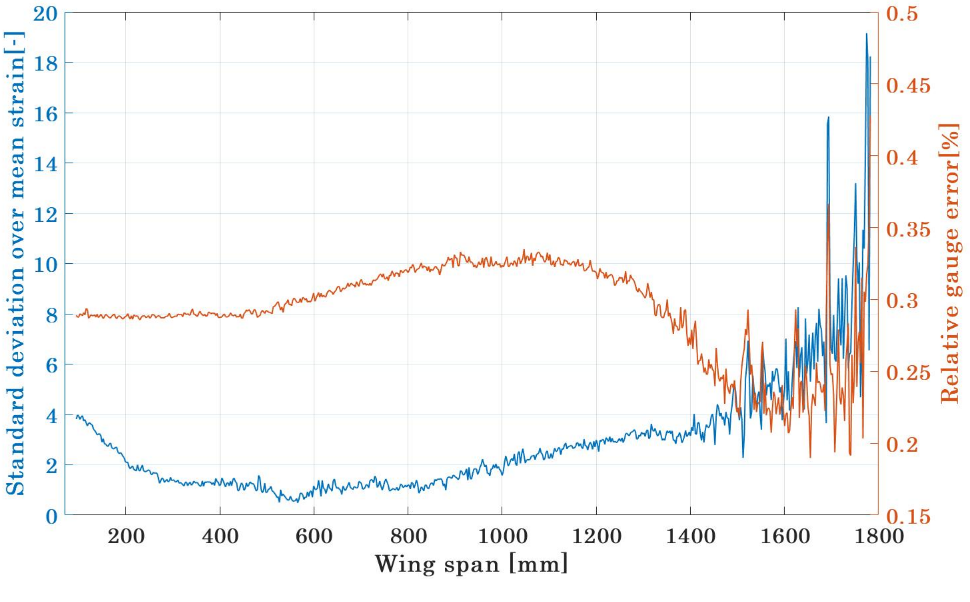

Figure 3.23: Standard deviation and error over wing span for 1^{st} mode, FOSS1

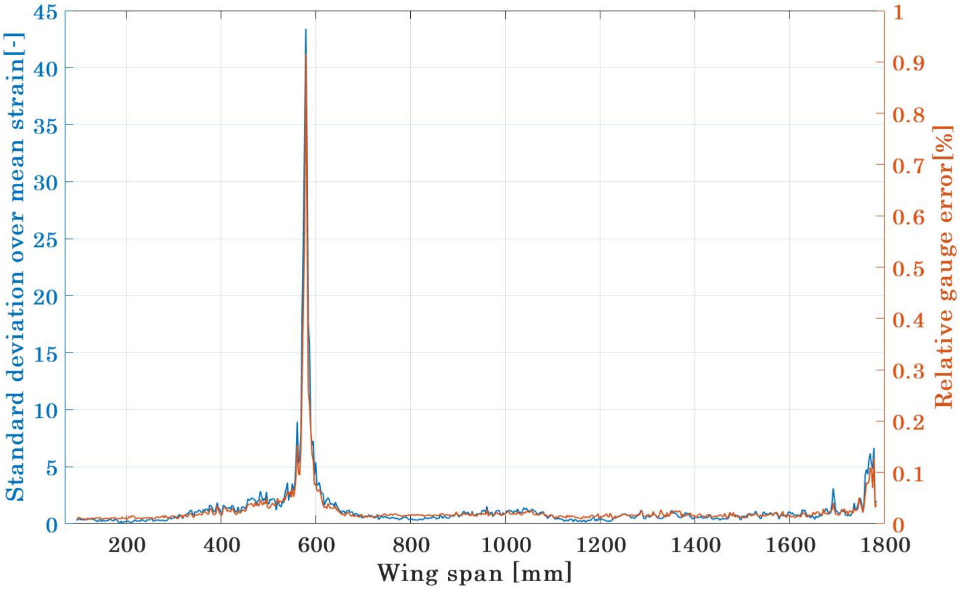

Figure 3.24: Standard deviation and error over wing span for 2^{nd} mode, FOSS1

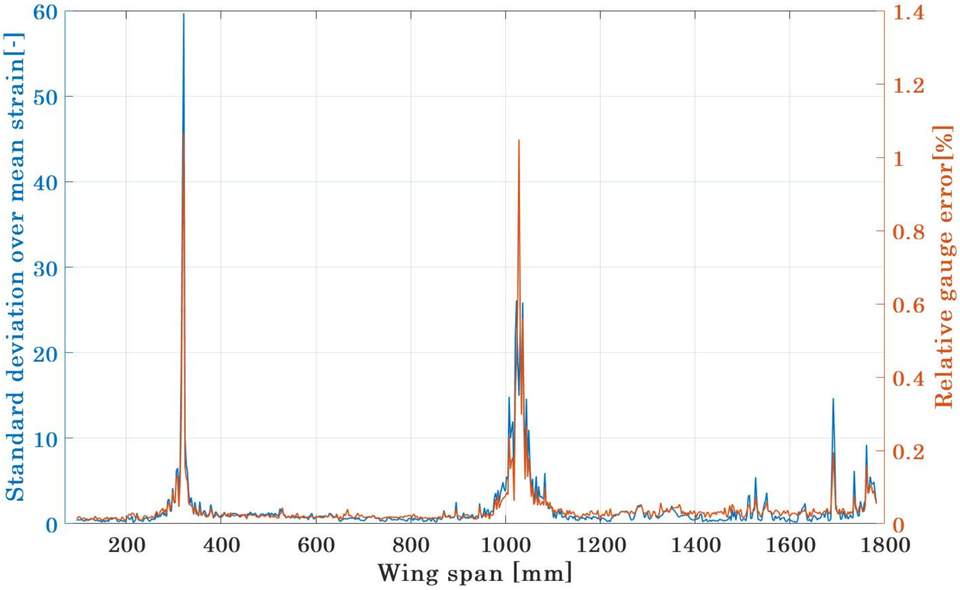

Figure 3.25: Standard deviation and error over wing span for 3^{rd} mode, FOSS1

The distributions of standard deviation over mean frequency peak do not exceed 1.52 % and the error and standard deviation distributions for the MSS are relatively close to zero except in the node positions. These results conclude that the MSS and natural frequencies can be considered to fulfil the repeatability criteria. Moreover, the static testing exhibited that the MSS obtained dynamically capture correctly the orthotropic features of the composite surface over the wingspan, as can be seen in the MAC values close to 1 between modal and static shapes. The natural frequencies and modal strain shapes obtained in the ESMA from the four FOSS were compared to the accelerometer and DMS results showing high level of correspondence. The methodology and results obtained in this chapter are considered successful and thus, the validation of FOSS modal parameters is completed. In the following chapter, the used methodology and experimental set-up for dynamic continuous strain sensing for modal parameter extraction was used for damage identification. The modal parameters obtained in this chapter from the seven repetitions serve as the baseline or undamaged configuration of the wing specimen.

4

Damage identification

The modal parameters extracted from high-spatial-resolution fibre optic strain sensors are comparable to the accelerometer and strain gauge modal data as proved and dicussed in section 3.3. The repeatablity of the experimental setup for dynamic testing showed low standard deviation and error of the modal parameters among the seven repetitions. With the stated conclusions in chapter 3, the validation of FOSS modal parameters is considered successful. The subsequent steps focus on answering the research questions related to damage identification. The first section of this chapter describes the design of experiments for damage identification, including the experimental setup. The second section consists of a bridge between the experiments and the results. There, the procedure for damage detection and location based on modal shapes is explained. Then, the synthesized results of the experiments are given, together with a discussion on them regarding the research objectives. Finally, an evaluation of the effect of noise from the ESMA in the damage identification results is performed.

4.1 Design of experiments

The specimen described in the previous Chapter is used in the experiments for damage identification. VIB-methods require a baseline approach (1.2.2), which means that they rely on the comparison between undamaged and damaged configuration. The modal parameters previously obtained are used as the pristine or undamaged state of the wing. The damaged state of the wing is obtained for different damage scenarios on the wing.

It is a common practice in VIB damage identification to introduce damages in a structure through local mass changes [8, 9, 83]. The reason for this is that the modal parameters defining a structure's dynamic behaviour are determined by its mass and stiffness. It is easily exemplified in the expression of the natural frequency of a single-degree-of-freedom system:

$$\omega_n = \sqrt{\frac{k}{m}} \tag{4.1}$$

Where k is the stiffness and m is the mass of the system. Structural damages such as delaminations, reduce the stiffness locally, reducing the resonance frequency. In like manner, a local increase in mass creates a decrease in ω_n. Many researchers have proven this hypothesis not only experimentally but also through analytical models which can predict the changes in displacements or curvature shapes due to stiffness drops or mass changes. The analytical derivation of the mass 'damage' scenarios lies beyond the scope of this project and the reader can refer to the following studies for more details: [46, 83, 14, 52, 6, 8].

Additionally, using a concentrated mass as damage instead of a real damage allows higher control over the damage severity, as it can be directly weighted. On top of that, concentrated mass is a reversible damage scenario, enabling the different damage experiments to be repeated and easily interchanged. The biggest drawback of this mass approach is that real damage scenarios involve a stiffness reduction, not a mass increase, which might cause the results from the mass experiments to not be directly comparable with a structural damage scenario. Consequently, the outcome of the experiments has to be modified before practical applications.

Several damages scenarios have to be evaluated to answer the proposed damage identification questions. For this reason, damages must be introduced all over the wing, in several span and chord directions, as well as in both surfaces equally. In order to design the experiments (DOE) for damage diagnosis the parameters or variables relevant for the study must be determined. The damage detectability span-wise, chord-wise, and in both surfaces of the wing are the main output of the damage experiments so the parameters of this DOE are: span, chord position, and top or bottom surface.

The chord-wise locations where damages are introduced correspond to the leading edge, trailing edge, and the wing mid-chord. These three locations have different characteristics such as the bond-line in the leading edge or the non-stiffened region between spars in the mid-chord. The span-wise locations are chosen according to the stiffness and modal characteristics of the wing. The wing has three distinct stiffness regions (see figures 3.2 and 3.3 for reference) which lead to jumps in the strain distribution along the wingspan (see figures 3.13, 3.14, and 3.15 for reference). One damage location is considered necessary before and after each stiffness region change in order to evaluate the effect of abrupt strain changes in the damage diagnosis. Additionally, one experimental location is set approximately in the middle of the three stiffness regions in order to analyze the damage identification capabilities without the effect of abrupt strain changes.

Overall, three damage locations are chosen per stiffness region, giving a total of 9 span-wise experimental locations. The last parameter to consider in the design of experiments is the surface of the wing under study, which is a binary variable; top or bottom. The design of experiments can be carried out once the parameters and levels of each analyzed parameter are set.

4.1.1 Taguchi method

The full factorial DOE requires a minimum number of experiments equal to:

$$N_{min}^{ff} = \prod_{i=1}^{NV} L_i = 9 \cdot 3 \cdot 2 = 54 \tag{4.2}$$

Where NV represents the three different parameters and L represents the levels of each parameter. The full factorial DOE requires 54 mass experiments, meaning a total of 216 dynamic experiments in the wing. This is because each damage scenario has to be tested 4 times as the LUNA ® system can acquire data from only one FOSS at a time with the maximum sampling frequency.

This amount of experiments is considered too large for the scope of this thesis, so the Taguchi method for DOE was used [75] to reduce the number of experiments. Taguchi methods are robust design statistical methods developed to improve the quality control and efficiency during manufacturing. Moreover, these methods have been applied to DOE in engineering and academic research.

Taguchi methods for DOE include the so-called outer arrays, which are often orthogonal. Orthogonal arrays are balanced to ensure that all levels of all parameters are considered equally. For this reason, the effect of the parameters can be evaluated independently of each other despite the fractionality of the DOE.

The minimum number of experiments required to conduct the Taguchi method is given by the expression below [11]:

$$N_{min}^{T} = 1 + \sum_{i=1}^{NV} (L_i - 1) = 1 + (9-1) + (3-1) + (2-1) = 12 \tag{4.3}$$

Therefore, the minimum number of experiments with the Taguchi method is found to be twelve.

An outer array of L18, meaning 18 experiments is chosen. The reason for this is that the FOSS are bonded span-wise because the maximum information in this direction needs to be extracted. This implies that at least one experiment is required in each span-wise location. In addition to this, the top and bottom surfaces have different stiffness distributions, then, both surfaces must be evaluated span-wise. Two surfaces and nine span-wise experimental locations give a minimum number of 18 experiments. The L18 outer array for the design of experiments used in this project is given in table 4.1.

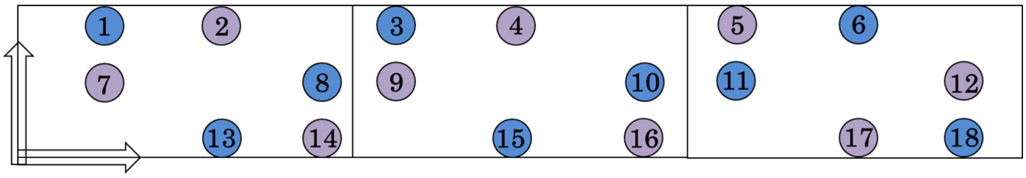

Figure 4.1: Experiments number and location

A sketch showing the approximate position of the 18 experiments numbered in table 4.1 is displayed in figure 4.1. The position on the wing for the mass or 'damage' experiments is given in figure 4.2. All the chord-wise damage locations are 50 mm away from the FOSS positions. This robust design of experiments allows investigating the three parameters in all their selected levels with only 18 experimental damage scenarios.

L18			
Experiment	Chord	Spar	Top\Bot
1	1	1	1
2	1	2	2
3	1	4	1
4	1	5	2
5	1	7	2
6	1	8	1
7	2	1	2
8	2	3	1
9	2	4	2
10	2	6	1
11	2	7	1
12	2	9	2
13	3	2	1
14	3	3	2
15	3	5	1
16	3	6	2
17	3	8	2
18	3	9	1

Table 4.1: Outer matrix L18

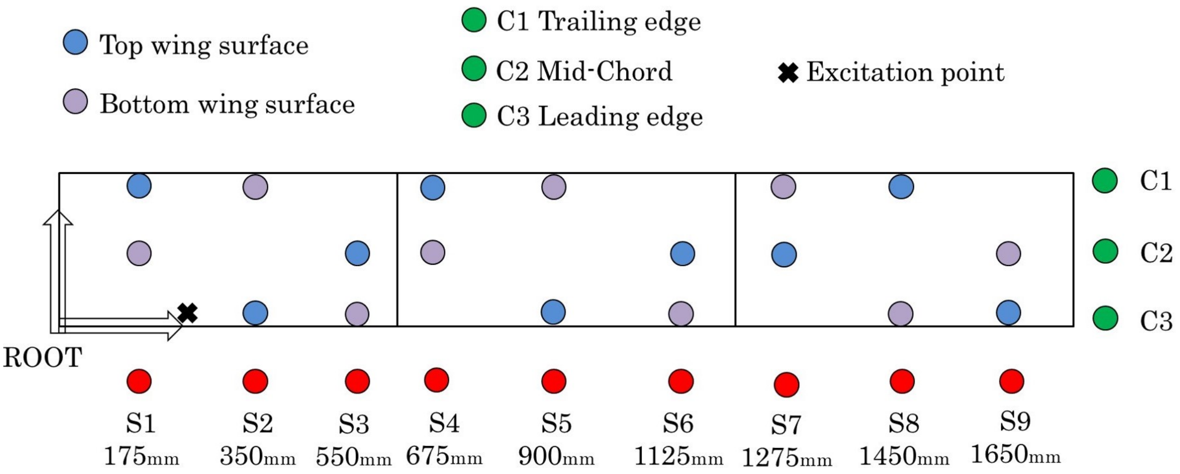

Figure 4.2: Sketch of design of experiments: Taguchi method

4.2 Experimental setup for damage detection

The dynamic tests for damage identification were carried as described in Chapter 3 section 3.2. The shaker, together with the force cell, was attached in the same excitation point as before, as shown in figure 4.2. The initial configuration of the boundary conditions and shaker should not be modified during the mass experiments because that would affect the modal parameters of the baseline state previously obtained.

The same acquisition systems and signals are used in this part which is done to reduce as much as possible the variability of external parameters.

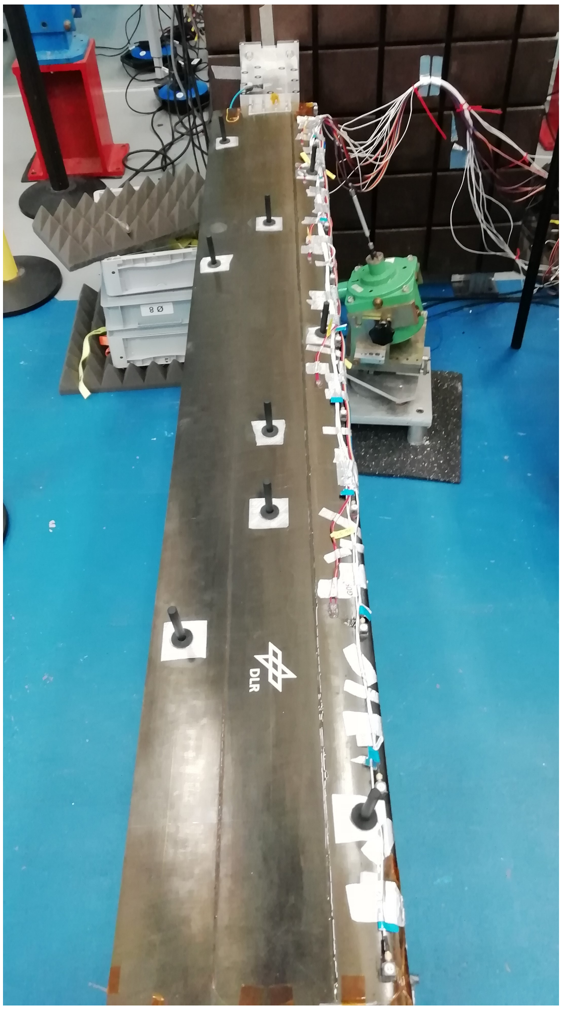

Figure 4.3: Mass damage scenarios in top surface

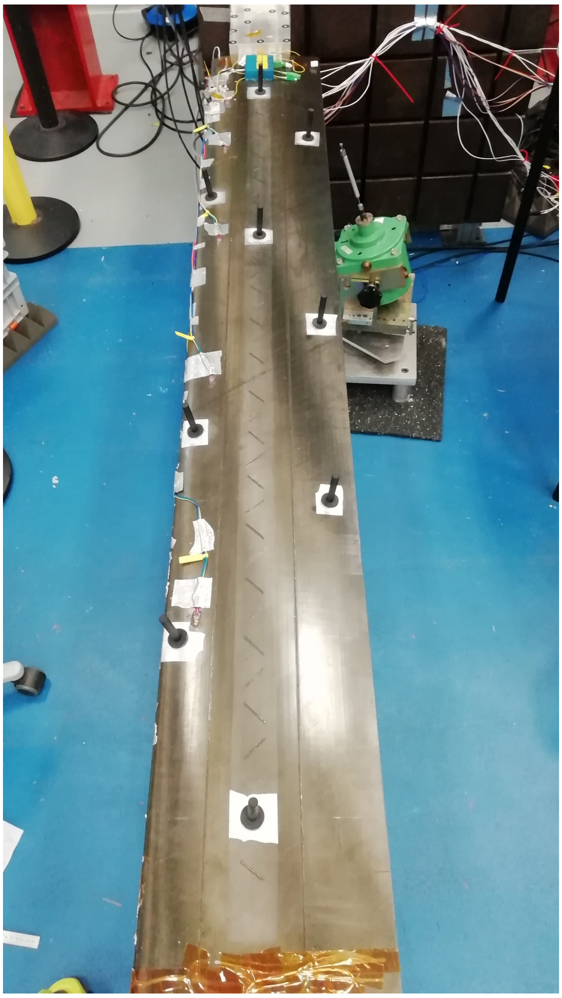

Figure 4.4: Mass damage scenarios in bottom surface

The weight representing a damage was introduced in the wing by means of a bolt-shaped attachment that can be seen in figures 4.5 and 4.6. One bolt was bonded to each of the 18 damage scenarios described in the previous section. The bonding technique consisted of sanding and cleaning the 'damage' position. Straightaway, a square piece of aluminum tape was bonded to the sanded position. Finally, the bolt is glued to the aluminum tape using a hot-silicone gun. Figures 4.3 and 4.4 display the top and bottom surfaces of the wing with the bolts bonded in the designed positions.

Figure 4.5: Close-up of a mass-simulated damage

Figure 4.6: Close-up of a 3D-printed bolt

The bolts were printed by employing a UV-resin-based additive manufacturing technique. The design of the bolts mimics the shape of an M6 bolt, as can be seen in figure 4.6. However, the dimensions of the bolt head were modified to increase the bolt head area in contact with the wing.

The main objective was to make the bolts as lightweight as possible such that their extra weight does not affect the wing modal parameters. Each bolt weighs 5 grams, so a total of 90 grams is introduced to the wing by the bolts. The modal parameters were re-evaluated after bonding the plastic bolts. It was concluded that such small weights distributed almost uniformly over the wing do not significantly affect its modal parameters.

The damages were simulated by adding weights to these bolts. The mass experiments were carried out using a weight of 180 grams. This weight was achieved by adding several iron nuts to the bolt as can be seen in figure 4.5.

One mass experiment was performed at a time, so this is a single damage identification approach. Later, the synthesis of all experimental results gives the overall conclusions of this chapter.

4.3 Damage identification procedure

The damage scenarios to be identified have been determined with the Taguchi method for DOE. Then, the setup for the dynamic damage experiments has been described. Now, this section is devoted to connecting these vibration tests with the results extracted from them. The diagnostic part of the damage identification procedure consists of three steps. Obtaining the modal parameters, computing the selected damage indexes, and identifying the damage. For this last step, the used algorithm for detection and location of mass 'damages' is described.

In the first step, the modal curvature shapes and the modal strain energy are obtained from the strain shapes. This process comprises the estimation of the MSS by utilizing ESMA, as performed in the before chapter, and the calculation of the MCS assuming the wing behaves as an Euler-Bernoulli beam. The local behaviour of the spars where the FOSS are bonded is considered to be mostly similar to a beam.

With these assumptions, the neutral axis of the wing for the two spar locations is calculated following the procedure explained in appendix E. According to equation 2.8, the MCS are directly proportional to the MSS (Ψ) in the case of pure bending modes. This relationship can be expressed as:

$$\kappa_i(x) = \frac{\Psi_i(x)}{NA_i(x)} \tag{4.4}$$

Where $NA(x)$ is the function for the neutral axis of any of the two spar locations over the wingspan.

The MSE can be derived from the MCS, as expressed in equation 2.9. The relationship between measured MSS and the MSE is, therefore:

$$MSE_i = \frac{1}{2}\int_0^l EI\kappa_i^2 dx = \frac{EI}{2}\int_0^l \Big(\frac{\Psi_i(x)}{NA_i(x)}\Big)^2 dx \tag{4.5}$$

Nonetheless, the MSS obtained experimentally are not a continuous function that can be directly squared and integrated over x. In order to compute the square of MSS, a linear polynomial is fitted in the segment between two adjacent gauges (segment length is equal to the spatial resolution $R_s = 2.6mm$). Then, this polynomial is squared. The combination of all the polynomials from the segments gives $(\Psi_i(x))^2$.

The function $NA(x)$ is a step-function, as described in appendix E, so integrating $1/(NA(x))^2$ is straightforward.

The numerical integration of $(\Psi_i(x))^2$ was carried by using the classical trapezoidal rule to each segment separately. This integration is expected to lead to minimum error levels because the nodes (gauges) are closely spaced [81]. With this technique, the area under each segment is obtained and the sum of all segments is calculated to obtain the overall area under the curve.

Chapter 2 gave an overview of the damage indexes that showed potential in the detection and location of damages with strain sensing. Four different methods have been selected and analyzed in this project: COMAC (eq. 2.2), ADM (eq. 2.5), DIM (eq. 2.7), and MSE (eq. 2.10).

These four damage indexes were coded as Matlab functions following the stated equations. The functions take the baseline and damaged modal parameters as well as the FOSS number as input. The output is the damage index over the span for each mode as well as the combined damage index. The DIF function is given below as an example.

$$[\beta\_\text{ij},\nu\_\text{j}] = \text{DIF\_func(baseline,damaged,FOSS)}$$

These functions also plot the damage index over the wingspan as can be seen in figures 4.7 to 4.10. These damage indexes correspond to FOSS1 from experiment 5, where the mass is located in the trailing edge and at 1275 mm spanwise. COMAC ranges between 1 and 0, being equal to 1 where the coordinate modal curvatures are equal. The larger the damage in one location the lower the COMAC value. CDF index has a minimum value of 0, in the case of no damages. There is no upper limit for this index and it can be normalized. DIM and MSE indexes have a baseline value of 1, in which case, no damages are detected or located.

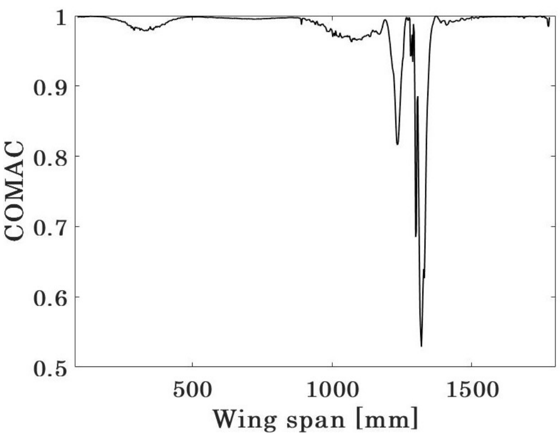

Figure 4.7: COMAC for experiment 5 (FOSS1)

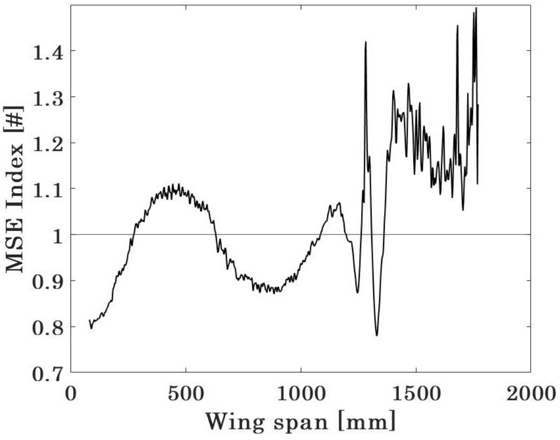

Figure 4.8: MSE index for experiment 5 (FOSS1)

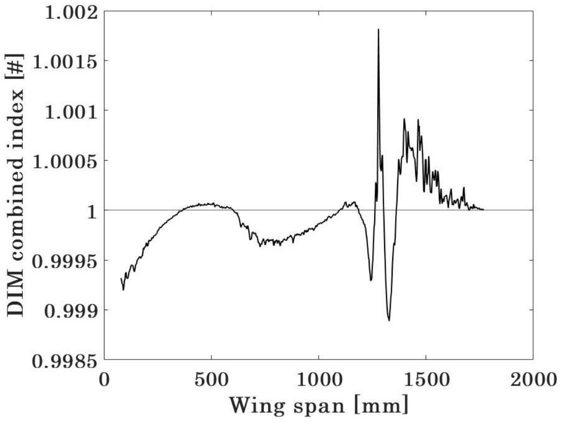

Figure 4.9: DIM combined index for experiment 5 (FOSS1)

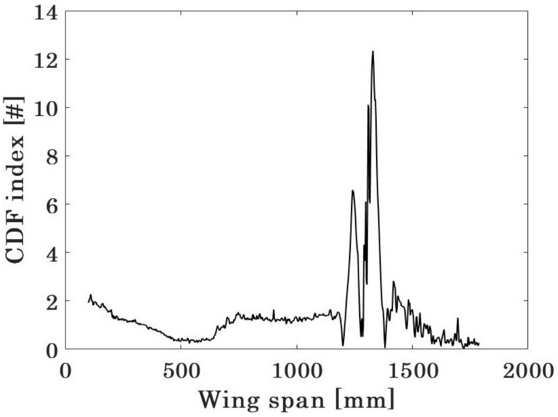

Figure 4.10: ADM combined index for experiment 5 (FOSS1)

4.3.1 Damage detection and location algorithm

Once the damage indexes have been obtained, the final step is to perform a damage identification with them. The damage diagnosis carried out in this project involves level 1 and 2, that is, detection and location of the damages.

Damage detection

MAC is the most commonly used magnitude for detecting damages based on modal shapes. However, in many cases it has been found not to be specific enough for precise detection of damages [16, 34]. For this reason, two criteria were used for damage detection. The flowchart summarizing the damage detection algorithm is shown in figure 4.11.

Firstly, the MACXP criterion proposed by Vacher et. al. [77] was used. This considers not only the shapes but the shifts in natural frequencies. The MACXP was computed for all 18 damage scenarios. In case of MACXP < 0.7, which is an assumption conservative enough [47, 19], the damage is considered as detected.

Secondly, the four aforementioned damage indexes were computed for each damage scenario. If at least 2 DI exceeded a certain threshold, then it was considered a damage detection. This threshold is unique for each damage index because they have different ranges.

The damage detection threshold ($Dthr$) was obtained in the following way: The seven vibration tests performed to the undamaged wing configuration (see section 3.5) were compared to each other. The four DI were then computed for the seven repetitions. Following that, the absolute difference between the computed DI and the baseline value of each DI was calculated. The maximum variation (ΔDI^{n}_{max}) for all repetitions in one

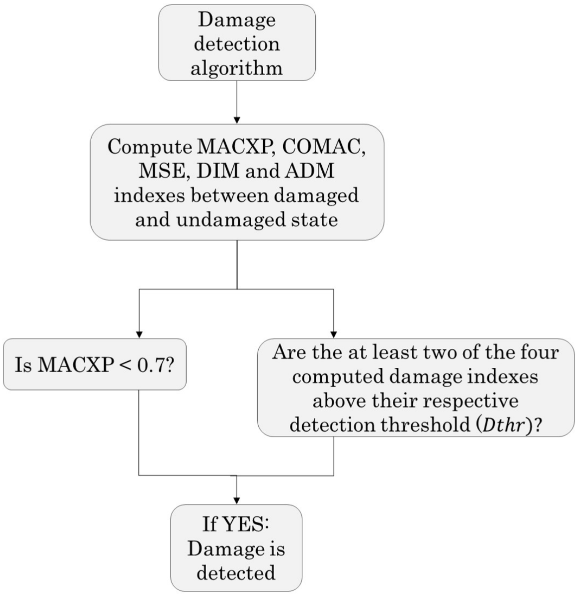

Figure 4.11: Damage detection flowchart

index ($DI = n$), was taken as the double of the detection threshold.

$$Dthr = \frac{1}{2}\Delta DI^{n}_{max} \tag{4.6}$$

Any variation of DI larger than this set threshold was considered as a damage detection in the algorithm. The results of this analysis are expected to answer question Q2.1 regarding damage detection.

According to the stated research questions, the step after damage detection is to determine the location of the damage (questions Q2.2 until Q3.2).

Damage location

The damages were located using the four damage indexes computed from the high-spatial-resolution MCS and MSE.

The algorithm for damage location consists of the detection of the peaks and valleys present in the damage indexes over the wingspan. These peaks and valleys are considered potential damage positions. The Matlab function *findpeaks.m* from the signal processing toolbox was used for this purpose.

This function inputs the resulting DI individually and outputs the peak position, prominence and width. The function is set in a loop in which several variables are modified. The changing variables are listed below:

1. Minimum peak prominence (MPP): Peaks or valleys which have a vertical drop of more than the minimum peak prominence from the peak on both sides. The MPP

is computed in every iteration as:

$$MPP_m = \sigma_{DI} \cdot f_m \tag{4.7}$$

Where σ_{DI} is the mean DI value in an experiment and f is a weighting factor for iteration m. The higher the f value, the higher the MPP, therefore, fewer peaks and valleys are detected.

2. Width of the peaks: The only peaks and valleys considered have a width in the restricted range [MINwidth, MAXwidth]. MINwidth is defined as twice the spatial resolution $MINwidth = 2 \cdot R_s$ because the mass damages affect more than one FOSS gauge. Peaks with lower width than MINwidth are considered spikes and outliers. MAXwidth is defined as $MAXwidth = 20 \cdot R_s$ for the first iteration. It is modified in every iteration to match the mean width of the detected peaks and valleys.
3. Minimum peak distance (MPD): A minimum distance between detected peaks and valleys is defined to avoid multiple detections in one particular location. Noise in the strain signals creates peaks in the DI which do not represent damages. These peaks are usually densely packed and can be differentiated from the real damages by the mean distance between them. In the first iteration, MPD is set to zero and is increased step-wise.

This loop was created to enhance the damage location and to limit the number of peaks and valleys detected in the DI. Figures 4.12 and 4.13 show the first and fourth iteration for the damage location algorithm. The CDF damage index is plotted together with the detected peaks and valleys (blue triangles). The results belong to experiment number 9 (location 900 mm in the wingspan and mid-chord) from FOSS2.

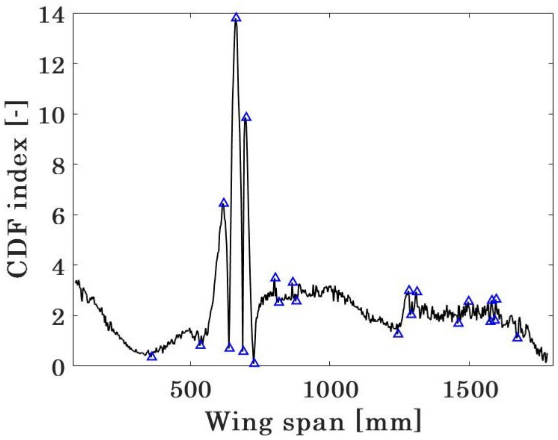

Figure 4.12: CDF index, peaks, and valleys for experiment 9 (FOSS2): First iteration

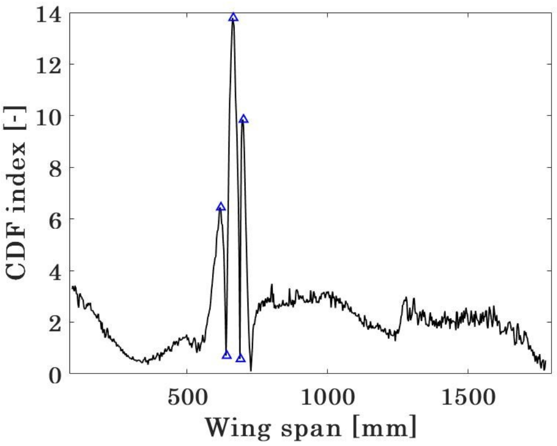

Figure 4.13: CDF index, peaks, and valleys for experiment 9 (FOSS2): Fourth iteration

Once these peaks and valleys are located, the amplitudes of the peaks are normalized from 0 to 1 with respect to the highest peak (or lowest valley). In the locations where no peaks nor valleys are detected, the DI function is set to zero. With this normalization, the DI function is transformed from 4.12 and 4.13 to 4.14 and 4.15, where only peaks and valleys are considered.

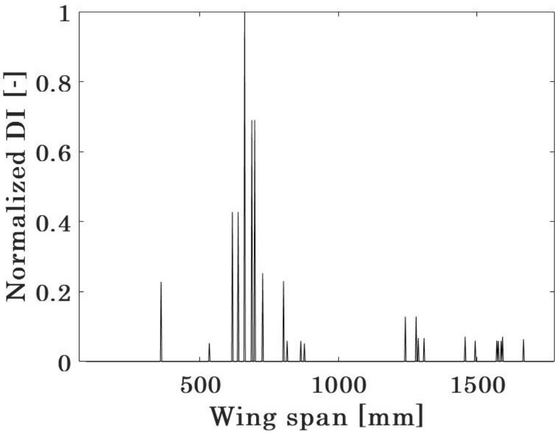

Figure 4.14: Normalized damage index for experiment 9 (FOSS2): First iteration

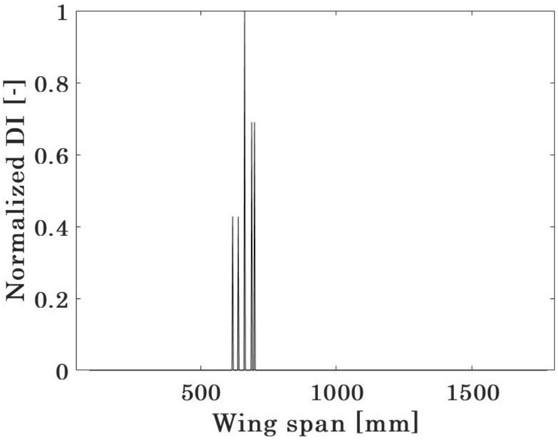

Figure 4.15: Normalized damage index for experiment 9 (FOSS2): Fourth iteration

Section 3.5 and appendix D discuss the error and standard deviation of the MSS for each mode in each fiber. It was concluded that the largest error and standard deviation are located around the nodal positions of the MSS and close to the fibre tip, where strains are the lowest. Gauges with higher error and standard deviation are most likely to have faulty detections. For this reason, the error and standard deviation distributions are considered in the damage identification procedure.

To do so, a Blackman window function was used to reduce the amplitude of the located peaks and valleys in a range near the nodal points and fibre tip. Podder et. al. analyzed the performance of three tipical windowing functions incuding the Blackman one and concluded that the Blackman window showed the best outcome in this type of scenarios [57]. This is achieved with a weighting factor that diminishes the amplitude of the normalized DI according to the error and standard deviation of each FOSS gauge in each mode.

4.4 Experimental results

4.4.1 Damage detection

The two used criteria for damage detection, according to subsection 4.3.1, were compared. In both cases, the damage was detected in every experiment. This leads to the conclusion that the MACXP as well as the selected damage indexes are capable of level 1 damage identification.

4.4.2 Damage location

One normalized damage index (NDI) (see for example figure 4.15) is obtained for every FOSS and every DI, per experiment. This gives a total of sixteen NDIs per experiment. These results are saved in matrix form, called the matrix of located damages. The matrix dimensions can be seen in the left of figure 4.16. The analysis of these matrix results is defined by the stated research questions in section 2.3.

The damage location success was determined per experiment. To do so, the sixteen NDIs of each damage scenario are summed up and combined as exemplified in the sketch below:

Experiment	FOSS 1	FOSS 2	FOSS 3	FOSS 4
1	4DIx650	4DIx650	4DIx650	4DIx650
2	4DIx650	4DIx650	4DIx650	4DIx650
...	...	...	...	...
N	4DIx650	4DIx650	4DIx650	4DIx650
...	...	...	...	...
18	4DIx650	4DIx650	4DIx650	4DIx650

⟹

Experiment	All FOSS
1	4DIx650
2	4DIx650
...	...
N	4DIx650
...	...
18	4DIx650

⟹

Experiment	All FOSS
1	1x650
2	1x650
...	...
N	1x650
...	...
18	1x650

Figure 4.16: Matrix of located damages: Initial and reduced version

The reduced matrix of located damages is formed by 18 arrays of 650 gauges. These arrays contain the damage information of the four DI and the four FOSS.

Damage location success

In order to find the damage location three methods are considered:

1. Position of the maximum value in the combined NDI in each experiment.
2. Position of the maximum value in the combined NDI in each experiment after a median filter is applied.
3. Position of the maximum of the sum of the four adjacent values to a gauge.

The positions of these three maximums were compared to the real damage location over the wingspan (see figure 4.2 for reference). If at least two of these values are within the location range (LR) of the damage, the damage location is considered as successful. This location range is taken as twice the 'damage size'. The 'damage size' is equal to the bolt diameter with which the weights are introduced in the wing. According to figure 4.6, the diameter is 25 mm, ergo, the LR or accuracy range is taken as $LR = 50\ mm$.

The minimum accuracy (or maximum error) for damage location is set, hence, damages located further than LR distance to the real damage location are considered incorrect damage location.

Figure 4.17 is a graphical representation of the damage location success in each damage scenario. A red dot containing a zero means that the damage could not be correctly located and a green dot containing a one means the opposite. According to these results, damages were successfully located in 83.3% of single damage scenarios.

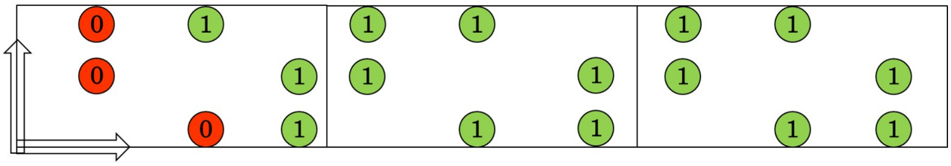

Figure 4.17: Damage location success per experiment

Damage location accuracy

How accurately each damage scenario is located is given in table 4.4. The accuracy is taken as the absolute difference between the real position of the damage and the computed one. The computed position is taken as the average of the three maximum values calculated, as explained above.

Experiment	Accuracy(mm)	Experiment	Accuracy(mm)	Experiment	Accuracy(mm)
1	558.2	7	1327.8	13	1064.4
2	3.6	8	9.2	14	24.8
3	6.2	9	12.0	15	3.0
4	5.6	10	6.0	16	8.6
5	6.8	11	4.2	17	1.8
6	4.4	12	6.2	18	11.4

Table 4.2: Accuracy in each experiment : Absolute error

Table 4.4 highlights that experiments 1, 7, and 13 could not be located with enough accuracy to consider them as correct locations. This is directly visible in figure 4.17.

Probability of correct damage location

The probability of correct damage location per experiment was calculated using the initial matrix of located damages (see figure 4.16). In this matrix, sixteen values of NDI were obtained per experiment.

The procedure to determine the damage location success is repeated but with the sixteen results per experiment. The probability of correct location was computed as the number of successful locations divided between sixteen.

The probability of correct damage location is higher in the tip of the beam where stiffness and mass are lower. When weight is added, the relative change of mass in the tip is much larger than in the root. The same conclusion can be extended to stiffness. This explains

Experiment	Probability	Experiment	Probability	Experiment	Probability
1	25%	7	31.25%	13	37.5%
2	43.75%	8	37.5%	14	43.75%
3	50%	9	62.5%	15	56.25%
4	56.25%	10	37.5%	16	62.5%
5	43.75%	11	68.75%	17	56.25%
6	81.25%	12	81.25%	18	62.5%

Table 4.3: Probability of correct damage location per experiment

why the tip of the wing is more sensitive to the presence of damages, as it is lighter and less stiff. The boundary conditions also affect the damage location. In the case of WTB and wings, the degrees of freedom at the root are highly constrained. This further increases the stiffness around the root area consequently reducing the detectability of damages.

The Taguchi method allows condensing experimental information with fewer experiments than the classical full factorial formulation. Therefore, the conclusions from the eighteen experiments were extended to the whole wingspan. The wing was meshed with square elements of size 25 mm (bolt diameter) where only the values of the eighteen known probabilities were introduced, the rest of the elements are filled with NaNs.

The probability of correct location was extrapolated using a spring metaphor. It assumes springs (with a nominal length of zero) connecting each element with every neighbour experiment. Each NaN element tries to become like its neighbours so the values of probability for the experiments are extrapolated as a constant function consistently with the neighbouring positions.

Figure 4.18 reinforces the conclusions stated above. The root of the wing is stiffer and heavier, therefore the probability of locating damages is lower than in the tip. The detectable damage size in each location is relative to the stiffness and mass of that region. Smaller damages are expected to be successfully located in the tip than in the root.

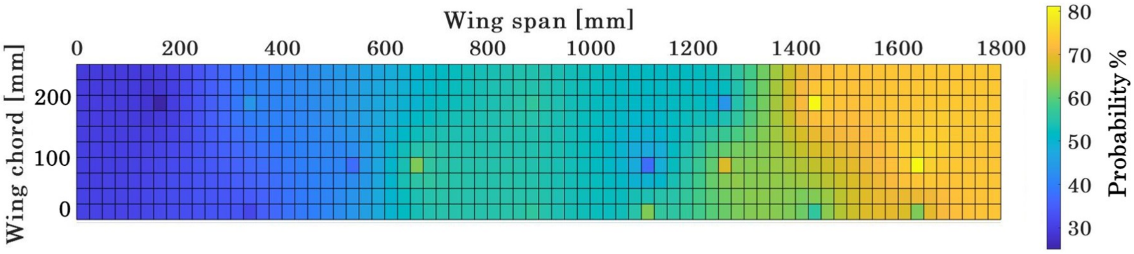

Figure 4.18: Probability map of correct damage location

This interpolation was performed for the top and bottom wing surfaces independently.

Results are shown and discussed in Appendix E. It was found out that similar conclusions can be drawn from that analysis.

Damage location precision

The precision of location in each experiment is given by the standard deviation of the combined NDI. It is computed only for those experiments with a correct damage location. A Hanning window is applied to the reduced matrix of located damages where the damage is located. The width of this window function is equal to LR. All index values away from this range are set to zero.
The next step is to fit a normal distribution into the windowed NDI function. The standard deviation of this distribution gives precision in the detection of each experiment.

Experiment	Precision(mm)	Experiment	Precision(mm)	Experiment	Precision(mm)
1	[N.A.]	7	[N.A.]	13	[N.A.]
2	12.1	8	8.7	14	8.5
3	8.9	9	8.6	15	9.9
4	1.3	10	11.1	16	11.1
5	8.9	11	10.6	17	1.3
6	11.2	12	12.3	18	12.0

Table 4.4: Precision of each experiment : Standard Deviation

It is out of the scope of this thesis to find out which distribution fits better each damage index distribution in each experiment. This is why a normal distribution was fitted in for all eighteen cases. Nevertheless, this distribution may not be suited for all damage scenarios. To check if a normal distribution works for an experiment, the value of the mean and median of the fitted distribution are compared. If the difference between mean and median did not exceed one-fifth of the mean (20%) then it was assumed that the normal distribution fits the data.

Figure 4.19 displays a 0 over a red dot in the experiments where a normal distribution could not be fitted, and a green 1 otherwise.

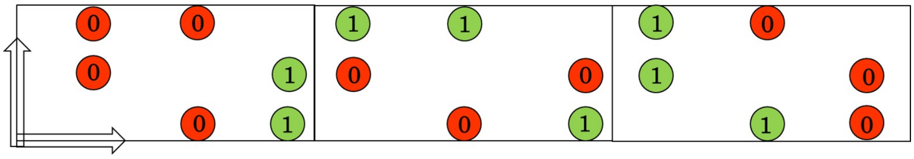

Figure 4.19: Normal distribution fitting success per experiment

The precision over the wingspan can be visualized following the same procedure as with figure 4.18. The precision or standard deviation in each experiment was extrapolated to the whole wing.
The average precision of the analyzed experiments is 8.3 mm. However, the computed

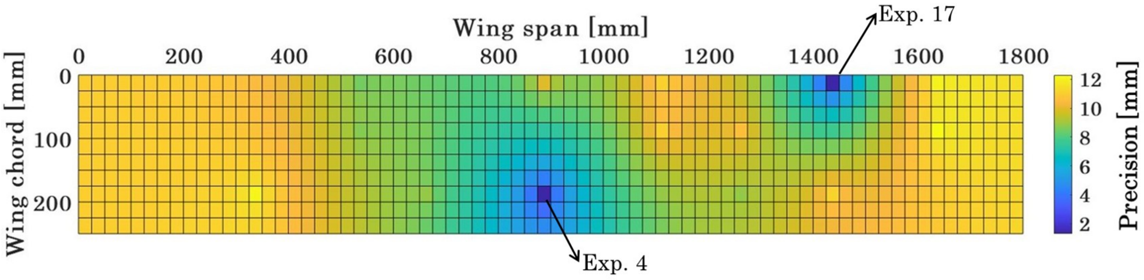

Figure 4.20: Damage location precision map (experiments 1, 7 and 13 excluded)

standard deviation in the case of experiments 4 and 17 is much lower, as can be seen in figure 4.21. This value is 1.3 mm which is one half of the used spatial resolution in the FOSS. For this reason, the precision results for experiments 4 and 17 are considered outliers. The damage location precision is mapped again over the wing. This time, experiments 1, 4, 7, 13, and 17 are not considered as explained above.

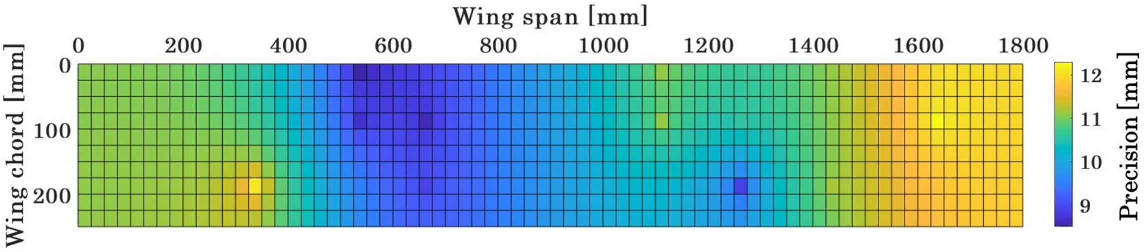

Figure 4.21: Damage location precision map (experiments 1, 4, 7, 13, and 17 excluded)

The average precision of these experiments is now 9.5 mm which is roughly 4 times the spatial resolution. The results highlight that 99% of the located damages with this algorithm and sensing technique are within 3 standard deviations to the exact damage location. On average, all damages could be located within 30 mm of the damage region.

The conclusions point out that the precision is more or less the same over the wingspan. It can be seen that the mid-span has the highest accuracy. The root region was expected to have the lowest precision and the wing tip the highest, following the results of accuracy and probability over the wingspan. However, this is not the case. This deviation might be due to two reasons:

1. Not all experiments could be used to determine the precision of the location technique and in addition, half of the experimental NDI could not be fitted into a normal distribution. For these reasons, the results for the precision of located damages should be taken as reference, not as evidence applicable to every composite beam-like structure.

2. The higher standard deviation in the tip region might be due to the lower signal to noise ratio of the FOSS at the tip. The number of faulty damage locations is expected to be higher in the tip region of the wing, where gauge error and standard deviation are higher (see section 3.5). This creates a wider normal distribution which is translated into a higher standard deviation and lower precision than expected in this region.

Faulty damage diagnosis

Once the accuracy and precision of damage location over the wingspan are known, it is important to determine where along the wingspan is more likely to have faulty damage identification. Faulty damage diagnosis in the present thesis refers to the scenarios in which a damage is detected but the location of such damage is not certain. Multiple positions in the wingspan are determined as possible damage locations. It is necessary to know where these faulty damage locations are more prone to happen and explain why.

For this purpose, a Hanning window was applied to all the NDI arrays in the initial matrix of located damages. The position where it was applied corresponds to the position of the located damage in each scenario. The width of this window function is equal to LR. All index values inside this range are set to zero, so only damages outside the location range were evaluated.

A detection threshold was established for these remaining indexes. The threshold is equal to a factor (Fa) times the amplitude of the maximum NDI in each experiment (this is where the damage is located). All values of NDI below this threshold were set to zero, and the rest were normalized. Additionally, the NDI outside the location range were considered faulty damage locations. The density of these faulty locations over the wingspan gives an idea of the areas where it is more likely to have a faulty diagnosis.

All the data in the matrix of located damages is combined and the result is an array of size 650 elements. The combination is achieved by summing all the arrays. Each element in this array is the combination of the faulty locations of all experiments, all DI, and all FOSS.

The results for faulty damage location distribution over the wingspan were computed for three different factors and shown in figures 4.22, 4.23, and 4.24.

From the plots, it can be concluded that faulty damage locations are more likely to occur at the tip of the wing, which is in concordance with the error and standard deviation of the MSS obtained with FOSS data. The data quality is lower at the tip of the FOSS, so it is more likely that noise is interpreted as damage there.

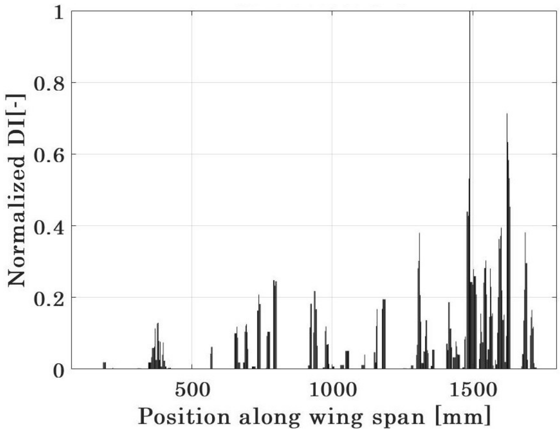

Figure 4.22: Faulty damage location distribution. Fa = 0.25

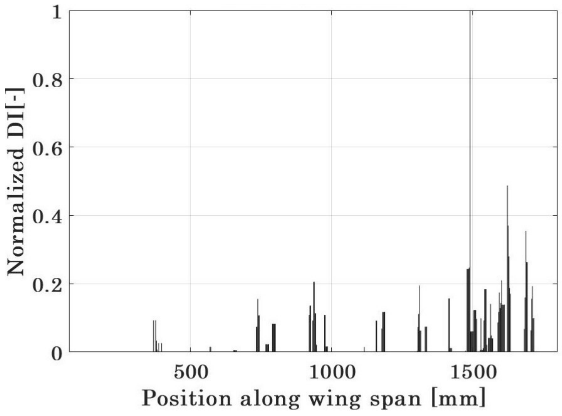

Figure 4.23: Faulty damage location distribution. Fa = 0.5

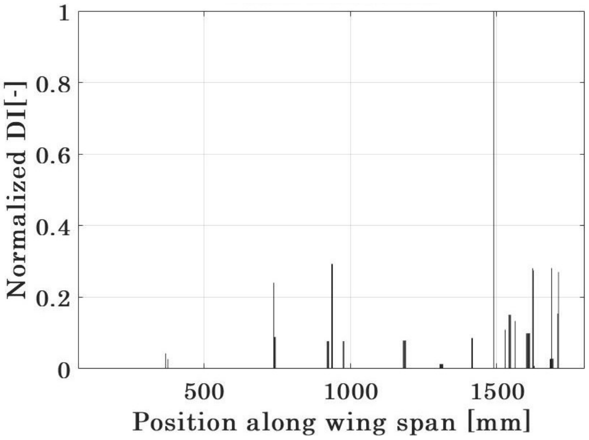

Figure 4.24: Faulty damage location distribution. Fa = 0.75

4.5 Numerical results

An FEM model of the composite wing was used to answer research question Q4. The main objective of this section is to evaluate the effect of experimental noise in the damage diagnosis capabilities of the studied methods and sensing technique. A comparison between the damage identification results obtained with experimental and simulated dynamic data gives the answer to the research question. The software NASTRAN and its dynamic solver SOL103 is used for this purpose [26].

4.5.1 NASTRAN model

A layout of the NASTRAN model without the top skin is displayed in figure 4.25. The top and bottom surfaces of the wing are modelled with CQUAD4 elements of approximately

6.7 mm. The ribs and spars are modelled according to the wing layout and material properties described in section 3.1. The boundary conditions are set like those of a cantilever beam, where all the degrees of freedom from the nodes at in span position 0 are constrained. The modelled boundary conditions differ from the real case scenario because the metallic clamp at the wing root is not modelled, nor is the attached shaker. The metallic clamp used to support the wing adds stiffness, but mainly mass to the wing root. These differences between the model and the real structure modify the modal parameters of the structure.

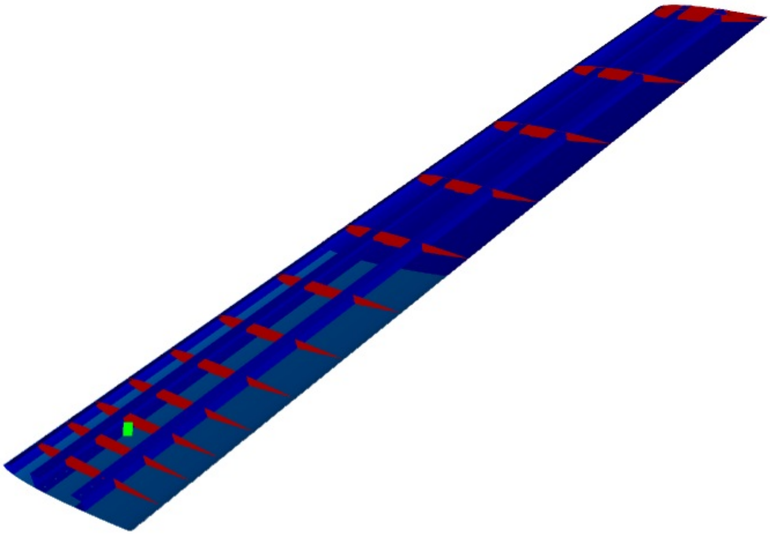

Figure 4.25: Isometric view of the wing model in NASTRAN: ribs and spars layout

Solver SOL103 gives the modal properties of the structure such as natural frequency, damping ratio, modal displacement and strain shapes. Validation of the natural frequencies for the analyzed modes is given in table 4.5 by means of a comparison between simulated and experimental results. The natural frequencies obtained with the three types of sensors are compared to the NASTRAN model and it was found that the natural frequencies of the model are higher. This is because the mass at the root of the wing model is lower than the real one because the metallic clamp is not modelled and, according to equation 4.1, the eigenvalues of the FEM model are higher.

Structural Modes	**Accelerometers**	**FOSS**	**DMS**	**NASTRAN Model**
1^{st} OOP	3.22	3.18	3.11	3.45
2^{nd} OOP	19.62	19.09	19.02	22.45
1^{st} IP	25.51	24.12	24.50	27.01
3^{rd} OOP	54.53	52.69	52.24	65.10

Table 4.5: Natural frequencies comparison [Hz]

A comparison between MSS of simulated and experimental data of FOSS2 is shown in figures 4.26, 4.27, and 4.28. The MSS obtained from the noiseless NASTRAN data, are smoother than the experimental ones, as would be expected. The overall modal shapes follow the same trend as the experimental ones, despite this, there are some visible differences. The location of the ply-drops is not the same. This leads to the conclusion that the model does not have exactly the same differentiated stiffness regions as the real wing. This deviation between real and modelled wing is added to the list of aforementioned differences. Moreover, the effect of the ribs stiffness can be seen clearly in the FEM MSS and not in the experimental ones.

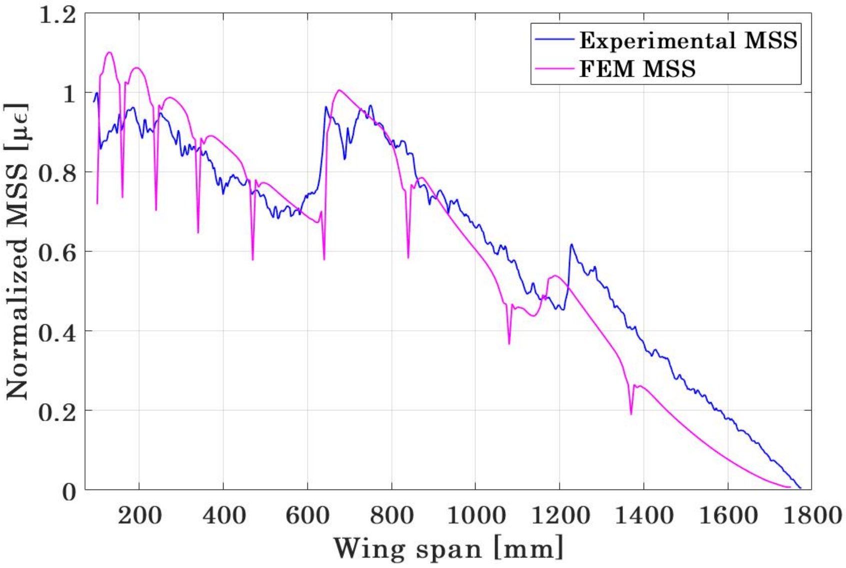

Figure 4.26: MSS for 1^{st} OOP bending mode (FOSS2)

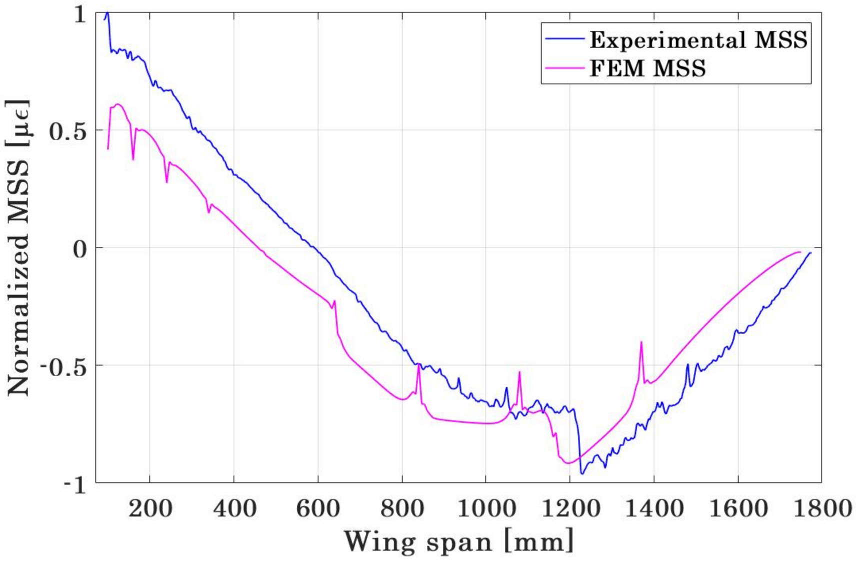

Figure 4.27: MSS for 2^{nd} OOP bending mode (FOSS2)

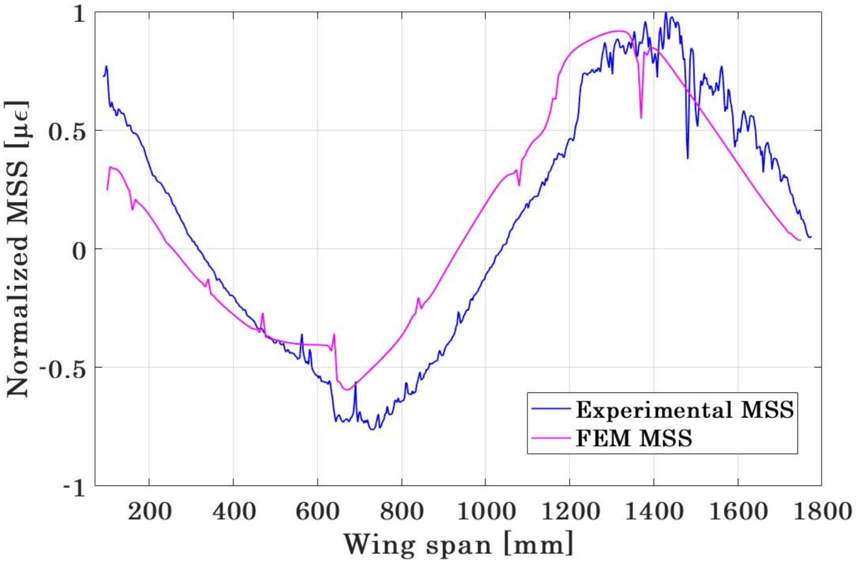

Figure 4.28: MSS for 3^{rd} OOP bending mode (FOSS2)

4.5.2 Effects of noise in damage diagnosis

The influence of experimental noise in the damage identification results is discussed in this section. The same damage diagnosis procedure explained and used for the FOSS experimental data was followed for the dynamic simulated data in NASTRAN.

The mass was introduced in the model by employing the element type CONM2 [25]. This element acts as a concentrated mass in a node. A total of 180 grams (the same weight used in the experiments) was added to the node closest to each of the 18 damage scenarios. The centre of gravity of this weight is 3 cm away from the surface of the wing, so this eccentricity is added to the analysis. A total of 19 simulations were performed, one for the baseline state of the wing and the remaining 18 for the different damage scenarios.

The strain data corresponding to the MSS was extracted from the nodes closer to the experimental locations of the four FOSS. From this simulated data, the MCS, MSE, and the previously used damage indexes are computed.

Using the damage detection criteria previously explained, the damage is detected in all damage scenarios. The results for damage location accuracy per simulated experiment are shown in table 4.6. The accuracy obtained with the noiseless data is of the same order of magnitude as the experimental one. However, it is interesting to see that the damage scenarios 1, 7, and 13; which could not be accurately located in the experimental part; can now be located with relatively high accuracy. Additionally, the lowest accuracy was found to be at the tip of the wing, with experiments 6, 12, and 17 having the lowest accuracy of approximately 40 mm. This value is higher than any location error from the experimental results (only correct damage locations are compared, so experiments 1, 7, and 13 are ignored). However, this is most likely due to the difference in spatial resolution from both analyses. The experimental resolution given by the LUNA ® system is 2.6 mm and the spatial resolution in the NASTRAN analysis is equal to the element size in the model surfaces that is 6.7 mm.

Experiment	Accuracy(mm)	Experiment	Accuracy(mm)	Experiment	Accuracy(mm)
1	10.0	7	10.0	13	15
2	15.0	8	0.6	14	24.6
3	10.0	9	3.8	15	21.3
4	0.7	10	6.7	16	20.0
5	18.3	11	11.6	17	48.0
6	43	12	38	18	3.0

Table 4.6: Accuracy in each experiment : Absolute Error

Table 4.7 displays the probability of correct damage location per experiment. The probabilities are, overall higher than the experimental case but the trend is inverted. This can be easily seen in figure 4.29 where the root region has a considerably higher probability of correct damage location than the tip. The contrasting results between experimental 4.18 and FEM 4.29 probability of correct damage location can be related to the divergences in the FEM model. It fails to correctly model the boundary conditions, the stiffness changes in the different regions along the wingspan, the clamp, and the shaker.

The faulty damage location distribution over the wingspan is also computed with the FEM data. Figures 4.30, 4.31, and 4.32 show the results from this analysis. In the case

Experiment	Probability	Experiment	Probability	Experiment	Probability
1	87.5%	7	81.25%	13	75%
2	68.75%	8	81.25%	14	25%
3	75%	9	75%	15	81.25%
4	31.25%	10	87.5%	16	75%
5	68.75%	11	68.75%	17	43.75%
6	25%	12	62.5%	18	43.75%

Table 4.7: Probability of correct damage location per experiment

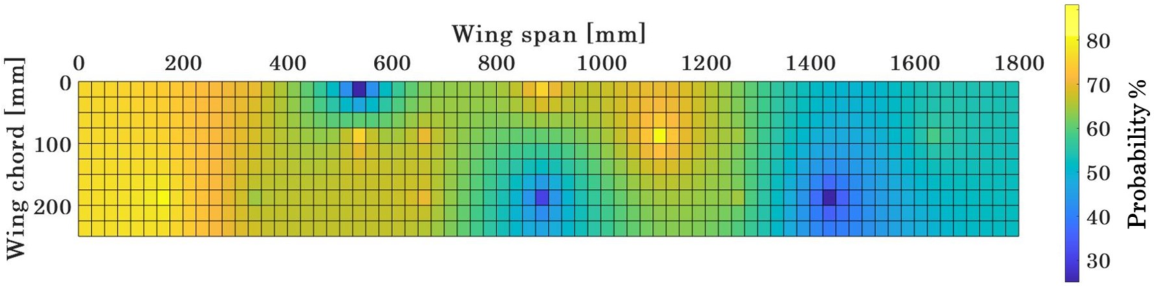

Figure 4.29: Probability map of correct damage location

of simulated data, similar concussions can be drawn. If damage is correctly detected but incorrectly located, the faulty damage locations are likely to be around the tip of the wing.

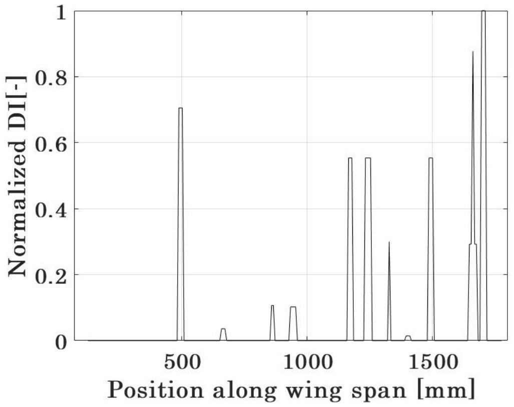

Figure 4.30: FEM Fault damage location distribution. Fa = 0.25

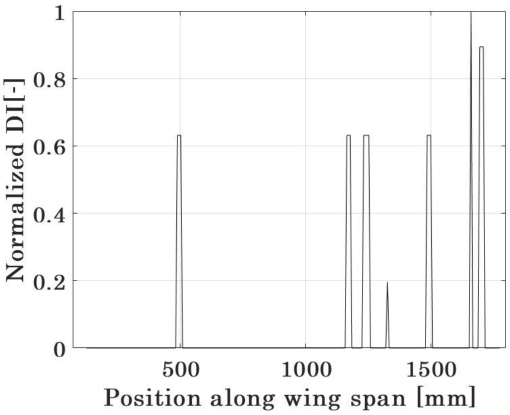

Figure 4.31: FEM Fault damage location distribution. Fa = 0.5

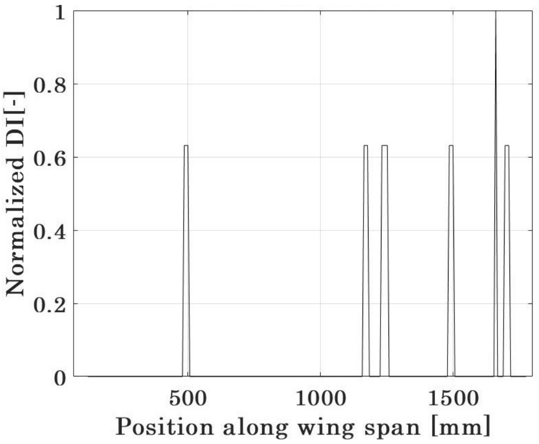

Figure 4.32: FEM Fault damage location distribution. Fa = 0.75

4.6 Damage indexes comparison

Given the results above, this section is devoted to analyzing the precision in damage identification of the four different damage indexes used in this project.

The precision of each damage index per FOSS is obtained as the ratio of correct damage locations with each DI divided by the total number of experiments. This ratio is shown as a percentage in table 4.8, in the case of experimental data, and figure 4.9 in the case of simulated data. The average percentage of correct damage location in all FOSS is also computed.

	FOSS 1	FOSS 2	FOSS 3	FOSS 4	Average
COMAC	56%	39%	39%	50%	45%
ADM	78%	61%	56%	67%	66%
DIM	61%	50%	33%	61%	51%
MSE	78%	33%	33%	39%	46%

Table 4.8: Percentage of correct damage locations with experimental data

	FOSS 1	FOSS 2	FOSS 3	FOSS 4	Average
COMAC	44%	39%	28%	50%	40%
ADM	72%	78%	67%	72%	72%
DIM	83%	67%	61%	72%	71%
MSE	83%	72%	61%	78%	74%

Table 4.9: Percentage of correct damage locations with simulated data

The COMAC index shows the lowest probability of correct damage locations amongst the four methods. The ADM index has the highest probability in the case of experimental data, with only a 6% difference between this one and the simulated results. These results demonstrate that these two indexes are the least affected by noise in the damage location probability.

On the other hand, the MSE index was found to be highly sensitive to data quality. This probability rises from a 46% to a 74% in the case of noiseless data.

As explained in Appendix A, the bond quality of FOSS3 reduced the strain transfer capabilities between the sensor and the host structure, leading to a poorer modal data quality in FOSS3, which is illustrated by the fact that this fibre has the lowest percentage of correct damage locations in all four damage indexes.

Overall it is found that no damage index works in all cases. For this reason, damage diagnosis should be enhanced by using more than one identification method at once. This can be concluded by comparing the percentage of correct damage location obtained independently with each method (Table 4.8) to the percentage obtained with the combination of all methods and FOSS which was found to be 83.3%. Similar conclusions can be drawn for the simulated data by comparing table 4.9 to the 100% success rate in damage location.

5

Conclusions and Recommendations

The objective of the present master project is to improve the current SHM techniques for global damage identification of beam-like composite structures. The studied damage diagnosis method is based in structural vibrations from which the modal parameters are obtained. The literature study provided an overview of the most common vibration-based damage identification methods. The modal curvature shape- and modal strain energy-based methods are selected due to their higher sensitivity to local damages. These methods are applied on a CFRP wing from which high-spatial-resolution modal shapes are obtained with a state-of-the-art fiber optic strain sensing technology.

The main research question of this dissertation is:

> ”Can high-spatial-resolution fibre optic strain sensors identify damages in beam-like composite structures?”.

In the following sections, the main conclusions of the chapters discussed in this thesis are summarized and the answers to the proposed research questions are reflected upon. Finally, recommendations for future research are provided.

5.1 Conclusions

The first research sub-question to be answered was:

> ”Are modal parameters extracted from high-spatial-resolution fibre optic strain sensors comparable to accelerometers and strain gauges?”.

The third chapter of this report was devoted to answering this question. The modal parameters from the FOSS are validated first by a comparison of its modal results to those of accelerometers and DMS. The good agreement in the dynamic results from the different sensors highlighted that the used optical sensing technique was suitable for vibration testing and experimental modal analysis.

The high-spatial-resolution modal strain shapes obtained form the FOSS are validated by means of a two step approach. The MSS of the fist out-of-plane bending shape are compared to the strain distributions obtained from a tip-load static test. Static and dynamic shapes showed great similarity. Proving that the MSS with these FOSS are able to capture the finest stiffness changes over the wing.

The last step in the validation consists of a study on the repeatability of the experimental approach used to obtain the FOSS modal parameters. This was achieved by analyzing and comparing the dynamic data of seven experiments on the baseline state of the wing, performed at different days and times.

The natural frequency peaks from the seven studied cases had an average standard deviation over mean peak value of 0.42%. The MSS of the three studied bending modes were plotted for graphical comparison and the MAC between them computed. The average MAC value of the repetitions was found to be 0.998, a value high enough to consider the repeatability analysis successful.

With these results, the validation of this state-of-the-art FOSS is regarded as accomplished.

The second research sub-question to be answered was:

> ”What is the detectability threshold of the introduced damage?”.

The fourth chapter of this report was devoted to answering this sub-question and its sub-sub-questions.

The detection of the introduced weight, acting as a damage, was successful in all eighteen damage scenarios. The location of the damage was successful in 83.3% of the experiments. The error in location of three experiments closer to the root was considered to be too high to be regarded as a correct identification. The probability of correctly locating a damage with proposed methodology and sensing technique is much higher in the wing tip than in the root. This is due to the stiffness and mass differences between both regions. The detectability of a damage by VIB methods depends on the relative damage severity. The root is stiffer and heavier so the damage, or mass attachment, have to be larger in absolute terms to be located correctly.

The precision of this technique is given as the standard deviation of the normalized damage indexes of all the methods and fibers. This precision is found to be, on average, around 4 times the spatial resolution of the optical sensor. In addition, it is found that the precision is the lowest in the wing tip region. This result might, at first, seem inconsistent with the previous conclusions. However, the fault detection analysis demonstrates that this region is most likely to have faulty damage locations. This high density of fault locations creates a wider distribution of damage indexes around this area, and consequently the computed standard deviation is higher, so precision is lower.

The third research sub-question to be answered was:

> ”Which is the most robust damage detection method or index, based on continuous strain readings?”.

The last section of chapter four is dedicated to compare the four used damage indexes. All four methods proved to reach a level 1 and level 2 damage diagnosis. The robustness of each method is given as the ratio between the experiments that have been correctly located and the total number of experiments.

It could be concluded that the COMAC index has the lowest probability of correct location. The methods ADM and DIM proved to provide correct locations in more than half of the cases, reaching more than a 70% of accurate damage identifications in the case of simulated noiseless data. In the case of the MSE-based index, the strain data quality showed to be a key parameter in its damage diagnosis capabilities. The relatively high noise of the FOSS strain readings is the reason why the percentage of correct locations is so low with experimental data, compared to the 74% of accurate locations with noiseless data.

Summarizing, none of the studied damage indexes could detect and locate the damages in all of the single damage scenarios. However, the combination of the four methods allowed to detect a damage in 100% of the cases and to locate it correctly in 83.3% of the cases.

The fourth and last research sub-question to be answered was:

> ”What are the effects of noise of FOSS measurements in the damage identification?”.

Section 4.5 from chapter 4 is devoted to analyze the effects of the experimental noise in the detection capabilities. This is evaluated by comparing real strain data to the simulated one from NASTRAN. The modal parameters of the FEM model are extracted and then validated by comparing them to the experimental ones. The model and the real wing are found to have several differences, especially concerning the boundary conditions and stiffness variations along the wingspan.

Level 1 and 2 damage identification are obtained for all eighteen simulated damage experiments. The accuracy of the detection is found to be around the same as in the experimental results. The probability of correct damage location is overall higher with the noiseless data. Nevertheless, this probability of correctly locating a damage is lower in the tip than in the root. These results are in opposition to the experimental ones. The reason for this can be related to the aforementioned deviations in the FEM modal from the reality.

The fault damage location over the wingspan shows similar distribution to the ones obtained in the experimental results. This leads to the conclusion that it is more likely to find fault damage identifications in the wing tip irrespective of the signal to noise ratio of the strain measurements.

The conclusions concerning noise effect in the different damage indexes have already been discussed in the previous sub-question.

In conclusion, the use of the proposed VIB damage identification methods together with strain data from continuously distributed FOSS is capable of level 2 damage identification in composite beam-like structures. The obtained results and conclusions from these project are expected to assist in the improvement of SHM techniques for large composite structures. This SHM technique can extend the lifetime of structures by preventing the unnecessary replacement of its components or detecting early damage progression. An accurate and precise, damage identification in operating WTB and airplanes can justify for longer inspection periods and lower safety factors in the design. This is expected to reduce the overall cost of maintenance in wind farms and hangars.

Moreover, another asset provided in the project is that the proposed technique is based on sensors that can be bonded or even embedded in the structure during manufacturing. These FOSS have high life-expectancy, electro-magnetic immunity and are fatigue resistant, so the health monitoring can be potentially carried out continuously and on-line from the manufacturing stage until the component replacement.

5.2 Recommendations

The findings and conclusions of the present thesis might support further development of the wind energy and aircraft sector by improving the designs for the next generation of composite structures making use of the information regarding damage progression and common damage locations. To take the presented framework a step further, several recommendations are enumerated in this section.

1. The present project proved that the sensing technique and VIB methods used together with the methodology followed, were able to reach level 2 damage diagnosis. The next step is to improve the SHM diagnosis to level 3 consisting of determining the severity of the damages present in the structure.

   It was found that the detectability of damage in a beam-like composite component depends on the damage position along the beam span. This means that larger damages can be found in the tip than in the root. With this information, the author suggests performing subsequent single damage experiments with different weights following the methodology presented in this thesis.

   The amplitude of the damage indexes obtained in the same experimental location but with different weights attached may be correlated with the introduced mass to obtain a relationship of DI amplitude and damage severity. This relationship is expected to be different along the wingspan.

2. The biggest drawback of the mass-damage experimental approach is that real damage scenarios involve a stiffness reduction, not mass changes, which might cause the results from the mass experiments to not be directly comparable with a real structural damage scenario. Consequently, the outcome of the experiments has to be modified before practical applications. The author suggests that a relationship between added mass and local damage can be achieved by finding a correlation between modal mass and modal stiffness for a beam-like structure. The fluctuations created in the modal matrices from the reduced-order model might be used to create an empirical cross-correlation between mass and stiffness. This step is considered after the severity of the mass damages can be evaluated (level 3 damage diagnosis).

3. The effect of the spatial resolution on the damage identification parameters such as precision and accuracy in location may be an interesting study. The analysis of this effect can be achieved by performing the damage experiments with different spatial resolutions available in the LUNA ® system. As mentioned in Chapter 3 section 3.2 the spatial resolution ranges between 5.2 mm and 0.65 mm. A parametric analysis

of this feature of the sensing technique would not only give information about the effect of modal parameter spatial resolution on the damage identification but would also bring insight into the noise levels derived from each spatial resolution and its effects.

A similar study is carried out by Sazonov and Klikhachorn [65] with modal displacement shapes and it shows the effect of this resolution in the central difference approximation used to derive the modal curvature shapes.

4. One of the advantages of this type of sensing technique and SHM technology is that the monitoring of damages can potentially be performed online. For this purpose the author recommends developing an online monitoring tool that connects the LUNA ® acquisition hardware with an external PC from which the measured strains can be analyzed right away. The online monitoring tool would use the LUNA ® ODiSi measurement streaming protocol such that, ODiSi 6100 acts as the data-streaming server and publishes online data of the LUNA measurement system through a TCP connection. The LUNA ® ODiSi software provides a remote interface to control the measurements, this remote interface can be installed on any computer, and it brings utilities such as preparing the system for measuring and allowing to start and stop a measurement remotely.

5. Pennachi et. al. [55] employed a neural network to find the optimal positioning of continuous optical fibre sensors for the modal analysis of wind turbine blades. The used OF sensors use the same back-scatter reflectometry technology as the ones used in this project. The FOSS path was optimized to capture 8 modes of interest in a simple plastic plate. The authors could successfully analyze all the modes and extract the modal strain shapes from the dynamic testing.

   Applying the methodology used by Pennachi et. al. is a good suggestion for future researchers using this sensing technique. With an optimal distribution of these FOSS, the modes in the range of interest, such as the $1st\ IP$ bending mode could potentially be captured correctly.

6. The wing structural response was modified by the fact that it was attached to a 2 tons metallic box and a shaker. The modal parameters and therefore the damage diagnosis results obtained with the experimental strain modal analysis differ from those extracted during operational conditions. The author suggests performing operational modal analysis for damage identification by dynamically testing the specimen with alike-operational conditions (e.g. in a wind tunnel).

   Moreover, the dynamic tests completed during this project were carried out in laboratory-controlled conditions. The effect of humidity, temperature and even thunder must be evaluated in order to further validate the applicability under real operating conditions.

A

Attachment of sensing network

As described in Chapter 3 the sensing network installed on the wing consists of accelerometers, FOSS and strain gauges. The application of those sensors in the wing is described in this appendix.

A.1 Accelerometers attachment

The accelerometers were mounted to the chosen locations at the leading and trailing edge above small 3D-printed attachments. These attachments adapt to the curvature of the wing, as shown in figure A.1 and are designed to align the measuring Z-direction of the sensors with gravity. Then the accelerometers were attached with petro wax, model 080A109 [56]. This wax is mainly used for quick mounting of light sensors at room temperature and low acceleration, and the wax model can be seen in figure A.2. The wax was softened with the fingers, applied thinly onto the 3D-printed attachments and then the sensor was softly pressed onto the wax.

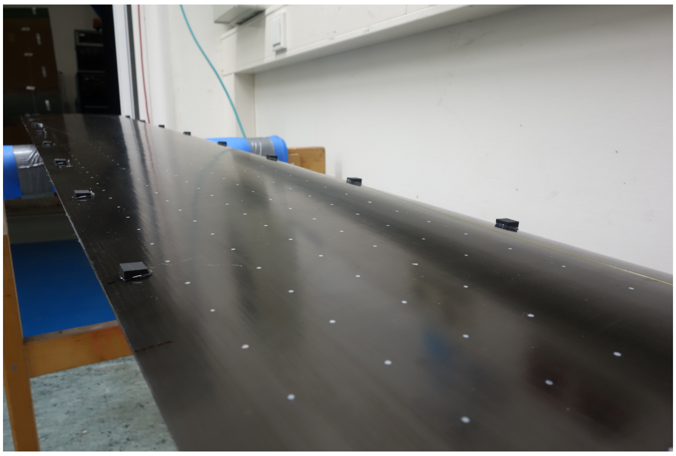

Figure A.1: 3D-printed edge attachments [78]

Figure A.2: Petro wax, model: 080A109 [56]

A.2 DMS bonding

The bonding process of the strain gauges to the wing started by smoothly sanding the composite surface at the locations of the strain gauges (DMS) with sanding paper P180, as per te Federation of European Producers of Abrasives (FEPA) standards. The sanded areas are cleaned with ethanol and a cross was drawn in the position where the DMS has to be bonded. A small amount of super glue was spread in the DMS bottom surface and the sensor was placed in the wing while applying a slight pressure until the glue was cured. Two short cables were soldered to the DMS and a room-temperature curing liquid silicon is applied to the bonded DMS for protection purposes. Finally, the short cable ends were soldered to 4 meter cables which were then connected to the measuring system.

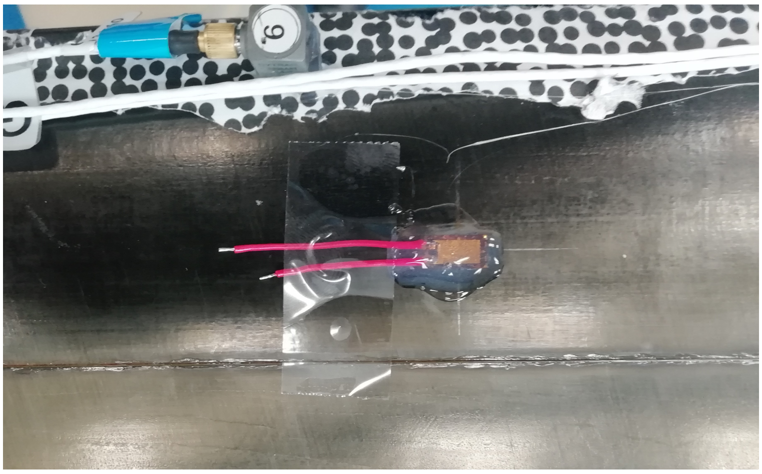

Figure A.3: Bonded strain gauge with silicon protection

A.3 FOSS bonding

For the bonding of the optical fibers, a very narrow width above the wing spars was sanded by taping the sides as shown in the figure A.4.

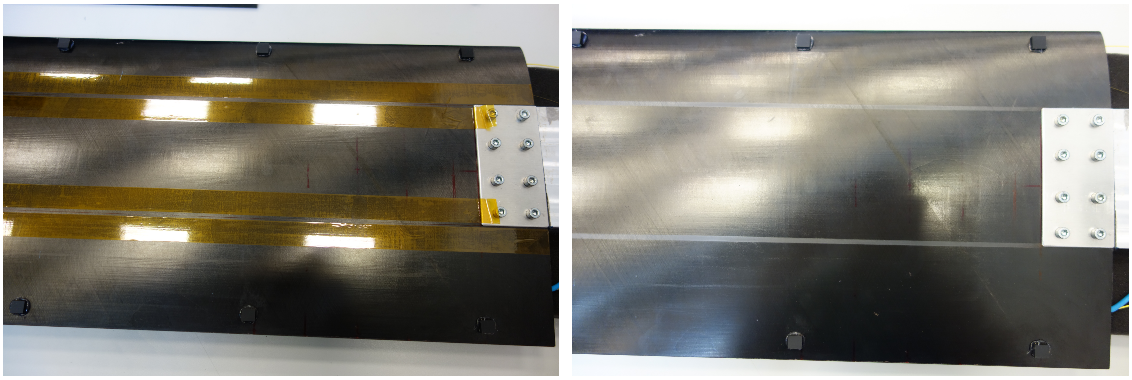

Figure A.4: Taping (left) and sanding (right) of the fibre path [78]

In many applications, for instance large structures, it is often not possible to insert the structure with the fibers in an oven to cure the bonding epoxy. For this reason, two different bonding materials were tested. Regular super glue was used to bond the FOSS1, FOSS2 and FOSS4, and a high-performance epoxy customized for optical applications used for bonding FOSS3. The epoxy model is EPO-TEK 353ND, and it is a high-temperature curing resin (between 80 and 180 degrees Celsius).

As curing the resin at such temperatures was not possible, it was left at room temperature for 48 hours until hardened. The load transmission capabilities of this epoxy with such unusual curing cycle are unknown. This bonding technique had visible effects in the strain reading quality of FOSS3. Figures and show the strain during a static test for FOSS3 and FOSS4, both located in the top wing surface. The strain readings from FOSS4 show a smoother shape compared to those of FOSS3, where large peaks and valleys are present, and these were especially large after strain concentrations such as ply drops. At first, it might seem as if the signal from FOSS3 has higher levels of noise, whereas in reality, it was mostly due to the bonding method. Previous studies on the effect of adhesive type and bond length point out that the strain measured by the optical fiber should be modified in order to reflect the influence of the adhesive and consequently, improve the accuracy of the measurements. Her et. al [31], investigated the effects on FBG sensors and developed a theoretical model to establish a more accurate relationship between the strains in the host structure and the surface bonded optical fiber.

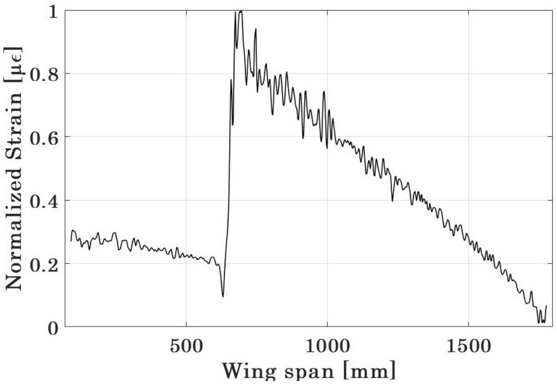

Figure A.5: Strain reading from static test with tip load in FOSS3

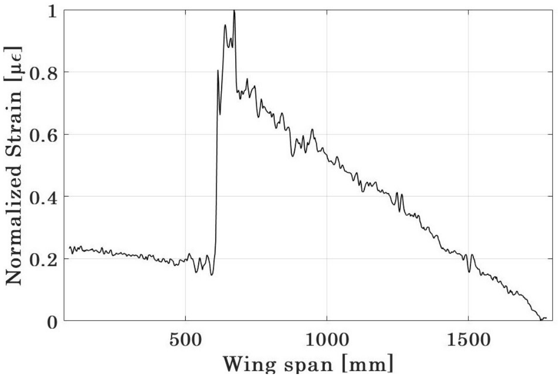

Figure A.6: Strain reading from static test with tip load in FOSS4

The poor bond quality of FOSS3 compared to the other 3 fibers has negative effects on the strain reading, and consequently on the modal parameters obtained from this fiber. The changes in strain modal shapes due to local damages are therefore, less likely to be able to be used to detect the damage compared to the changes in strain modal shapes under ideal strain transfer between structure and fibre.

B

LUNA ® system problem analysis and solutions

The different issues found during dynamic experiments with the LUNA ® system are listed below, although most of them are found to be interrelated.

B.1 Dropouts in data

The LUNA® ODiSI system relies on a correlation between reference and measured gauge data to calculate the strain or temperature along the sensing fiber. Several sources such as environmental disturbances can lead to a degradation in the signal which makes the correlation light to strain unreliable and, in these situations, the system rejects the unreliable measurement and replaces it with a NaN (not a number). These NaNs are present in the raw data files from the ODiSI along time and space.
These dropouts in data are found to be related to the frequency and the amplitude of the excitation signal. This relationship is visible in the graphs below, which show the losses in data from the wing (FOSS3) excited with a linear sweep up of frequencies between 15 and 55 Hz, this frequency band contains the second and third out-of-plane bending modes of the wing. The strain signal from the fiber shows a higher percentage of dropouts in data while exciting close to or with the resonance frequency when displacements and accelerations are much higher in amplitude. In addition, it can be observed in figure B.1 that a larger amount of data per time stamp is lost during the second resonance peak which occurs at a higher frequency.

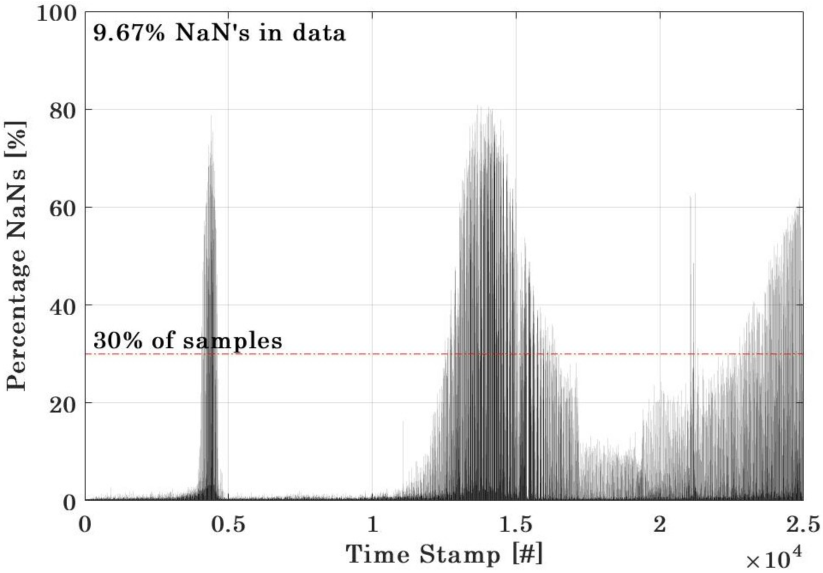

Figure B.1: Losses in data per sensor

In figure B.2 one red dot is displayed in every position where a NaN is found in the raw data file from LUNA ®. The total percentage of data loss is shown in the right side graph. The clusters of red-dots in the graph correspond to the time-stamps when resonance takes place.

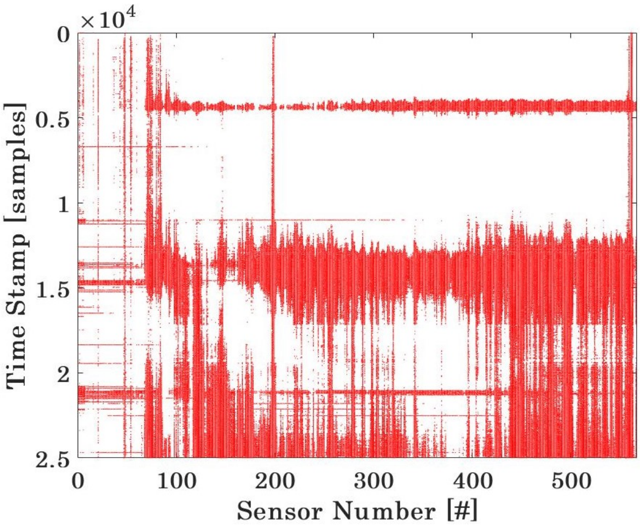

Figure B.2: Overall losses in data Time Stamp vs Sensor Number

Another problem often met while post processing LUNA ® data is that sometimes random FOSS positions measure spikes, this means, an outlier in the strain measurements normally several orders or magnitude greater than the rest of measurements from that sensor or adjacent ones. These spikes are considered as incorrect strain or temperature calculations due to weakening of the back-scattered signal. These outliers are set to zero when its value is one order of magnitude above the mean value of the absolute of the strain readings.

B.2 Non-uniform sampling rate

The time vector directly decoded from the raw data of LUNA ODiSi shows that the time stamps are non-uniformly sampled, thus the sampling frequency changes during the experiment. Nevertheless, it is important to mention that the acquisition system up-samples and down-samples even when the FOSS is under no excitation.

Wrong time stamps from the signal are related to the presence of NaNs in the strain data. The relationship between losses in data and wrong time stamps can be seen in the figures below B.3, B.4. The data from these plots belongs to an excitation signal with constant frequency equal to the third bending frequency of the wing (52.5 Hz) but the amplitude of the signal is linearly increased. Consequently, the amplitude of the displacements in the wing increases over time.

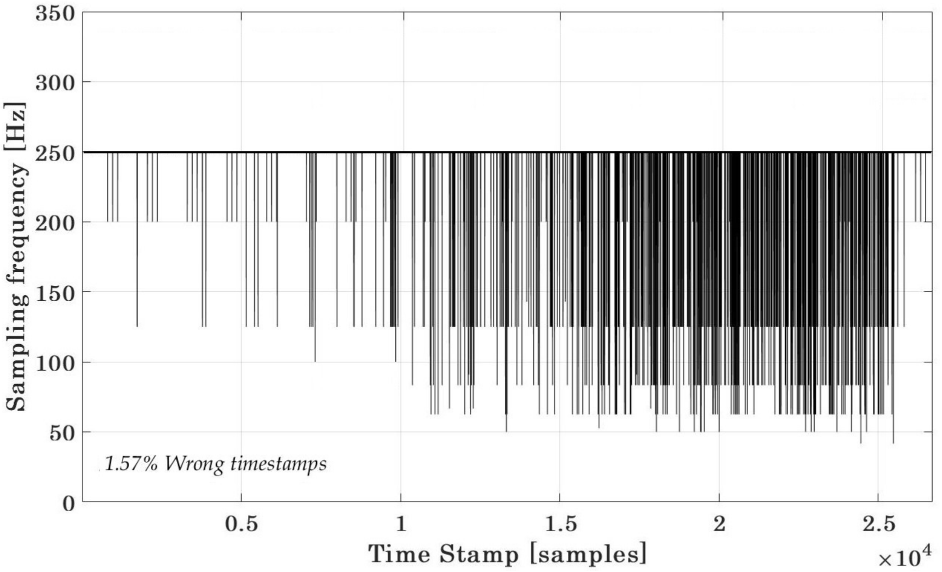

Figure B.3: Sampling frequency while increasing amplitude

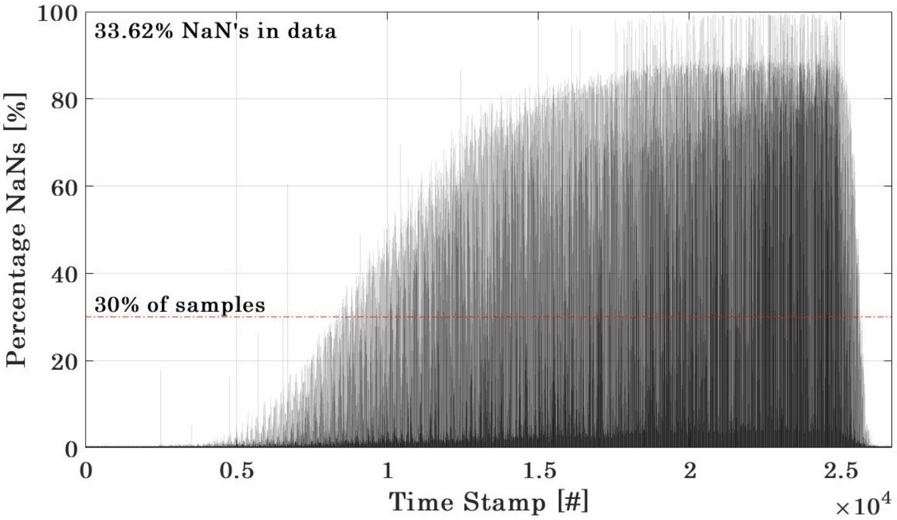

Figure B.4: Data losses while increasing amplitude

According to the provider company, the reason for the non-uniform time steps has to do with run-time of the laser-light, especially, the back-scattering effect.

B.3 Proposed solution

Given the fine spatial resolution of the LUNA ® system, interpolation in time and space is performed. An open source 2D interpolation scheme called *inpaintnans.m* was used for this purpose.

This function takes the strain data matrix with the NaN values and creates a grid equal to the size of this matrix, then, the NaNs are detected. When the locations in the matrix to be interpolated are known the function uses a spring metaphor. It assumes springs (with a nominal length of zero) connecting each gauge with every neighbor (horizontally, vertically and diagonally, in time and space). The function tries to make each gauge like its neighbors, so extrapolation is as a constant function where this is consistent with the neighboring gauges.

This function is found to be capable of fully reconstructing the strain response signal from the LUNA ® ODiSi 6100 acquisition system.

The down-sampling and up-sampling inaccuracies of the acquisition system prevent the LUNA ® system strain data from being correctly analyzed. Fos these reason, the time vector from the raw data must be re-sampled at a uniform sampling frequency. For this purpose, the function *resample.m* from the Signal Processing Toolbox in Matlab, is used to resample the signal at a specified uniform sample rate. This functions takes the non-uniform time vector and the fully interpolated data matrix without NaNs, and interpolates the strain data onto a vector of uniformly spaced instants with the specified sampling frequency.

The main issue found while working with this function is that the polyphase antialiasing filter used in the function introduces an attenuation in the amplitude of the signals. Thus the measured amplitude during vibration testing is attenuated during post-processing.
Moreover, the reconstructed signal might show some aliasing in higher frequencies, specially those close to the Nyquist frequency. Nyquist frequency is theoretically half of the sampling frequency $\omega_{Ny} = \frac{1}{2}\omega_s$, however Eyer and Bartholdi [20] have proved that in case of irregular time sampling the Nyquist frequency is lower. For the present study the following relationship is considered conservative enough:

$$\omega_{Ny} = \frac{1}{2.56}\omega_s = 97.65Hz \tag{B.1}$$

C

Neutral axis calculation

The calculation of the neutral axis is performed according to Ko's theory for in-flight deformed shape predictions of aerospace structures [36, 35]. Ko's theory uses an approximation to compute the neutral axis variation in tapered beams such as aircraft wings, although this is not the case for the wing understudy, the variable-stiffness regions have a similar effect in the neutral axis variation over the wingspan. This approximation works better for symmetric profile wings which is the case of the wing used in this project.

According to Ko's theory, the distribution of the neutral axis along the span is computed using strain readings from the wing surface. Strain sensors must be applied to the top and bottom surfaces of the wing in the same chord position.
As it was discussed in chapter 3 section 3.2 the wing sensing network includes four high-spatial-resolution FOSS bonded at two different chord positions (the reader can see figure 3.7 for reference). The distance from these four fibres to the neutral axis of the wing can be computed with the following equation:

$$NA_{FOSS1}(x) = -h_{TE}\frac{\epsilon_{FOSS1}(x)}{\epsilon_{FOSS1}(x) - \epsilon_{FOSS4}(x)} \tag{C.1}$$

$$NA_{FOSS2}(x) = -h_{LE}\frac{\epsilon_{FOSS2}(x)}{\epsilon_{FOSS2}(x) - \epsilon_{FOSS3}(x)} \tag{C.2}$$

$$NA_{FOSS3}(x) = -h_{LE}\frac{\epsilon_{FOSS3}(x)}{\epsilon_{FOSS2}(x) - \epsilon_{FOSS3}(x)} \tag{C.3}$$

$$NA_{FOSS4}(x) = -h_{TE}\frac{\epsilon_{FOSS4}(x)}{\epsilon_{FOSS1}(x) - \epsilon_{FOSS4}(x)} \tag{C.4}$$

Where $h_{TE} = 19mm$ and $h_{LE} = 24mm$ is the distance in the thickness direction (z-axis) between the trailing edge fibers and the leading edge ones respectively. The functions $\epsilon_{FOSSN}(x)$ stand for the strain measurements along the wingspan (x-axis) or fibre number N. These strain readings are obtained with a bending static test using a tipping load. The procedure for the static testing is described in chapter 3 section 3.4 where a figure 3.16 shows the test-setup.

The load is introduced employing a 3D-printed attachment whose shape and main dimensions can be seen in figures C.1 and C.2. The inside surface of the attachment follows the same airfoil shape as the wing, whereas the outer surface includes three holes for M6 bolts. These bolts are used to connect the attachment with the ropes that hold a plastic box that contains two half-kilo weights, as can be seen in figure C.3.

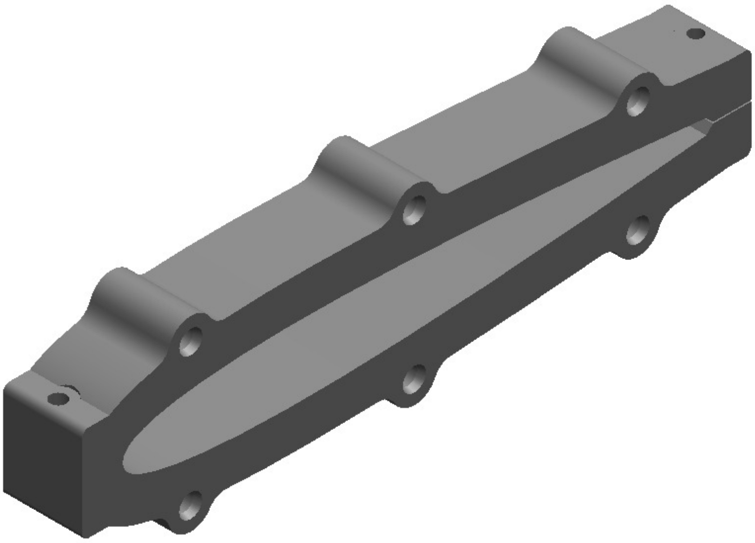

Figure C.1: Isometric view of 3D-printed attachment

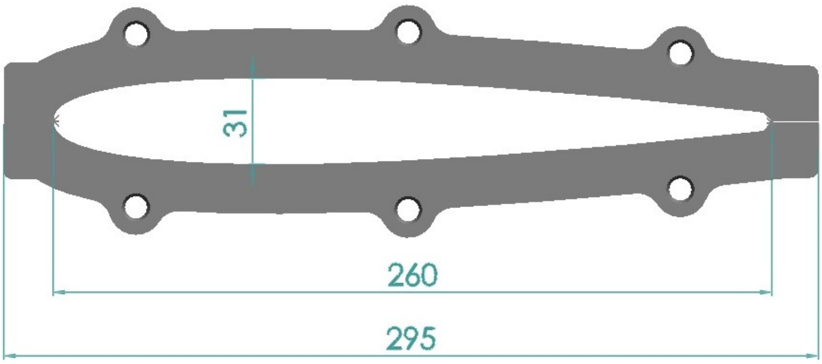

Figure C.2: Front view for the 3D-printed attachment including main dimensions (in [mm])

The distance between the neutral axis and the four FOSS has been computed and the results are displayed in figure C.4. It can be observed that the distance is almost constant along each of the three differentiated stiffness regions, so the function along the wingspan has a piece-wise distribution. The large noise values present in the LUNA ® system together with the variability of stiffness, and therefore strain, of the composite surface are the main causes of these wavering distributions of the neutral axis along the wingspan. Figure C.5 displays an approximation for the piece-wise function along the span. This approximation is computed averaging all the neutral axis values in each of the three stiffness regions.

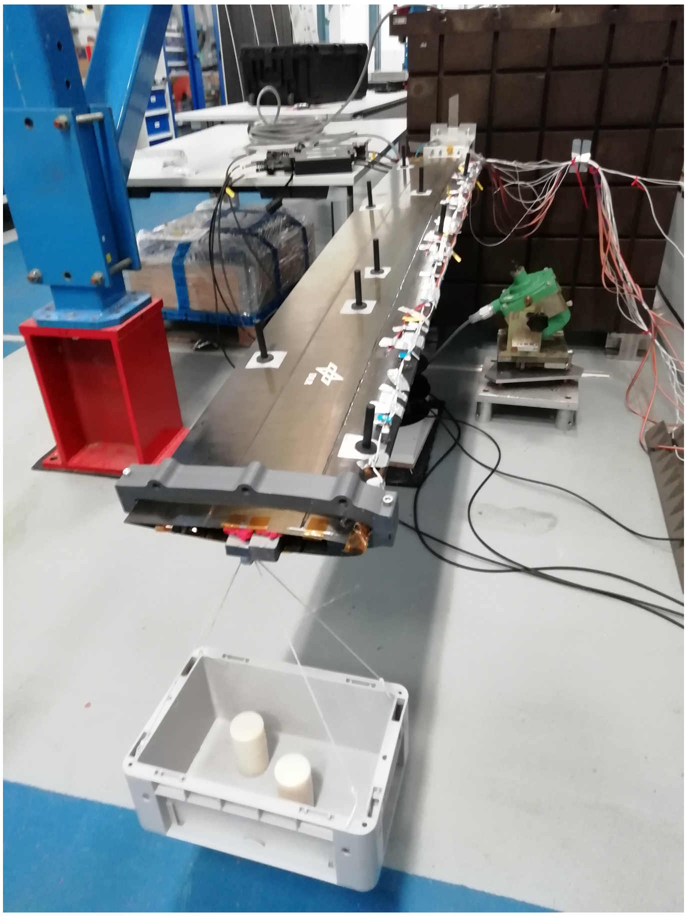

Figure C.3: Tip load introduction with attachment, ropes, and plastic box with the weights.

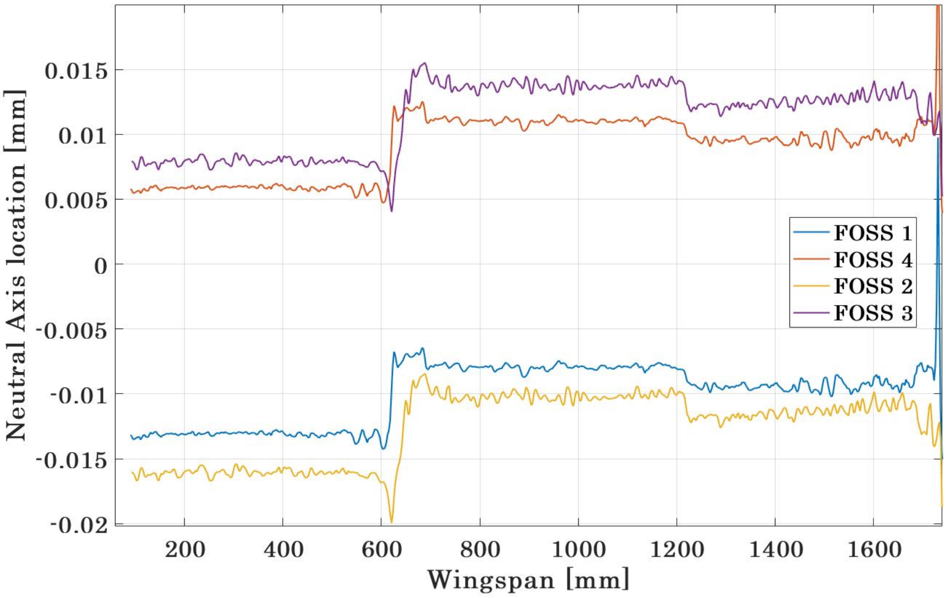

Figure C.4: Distance from FOSS to neutral axis of wing

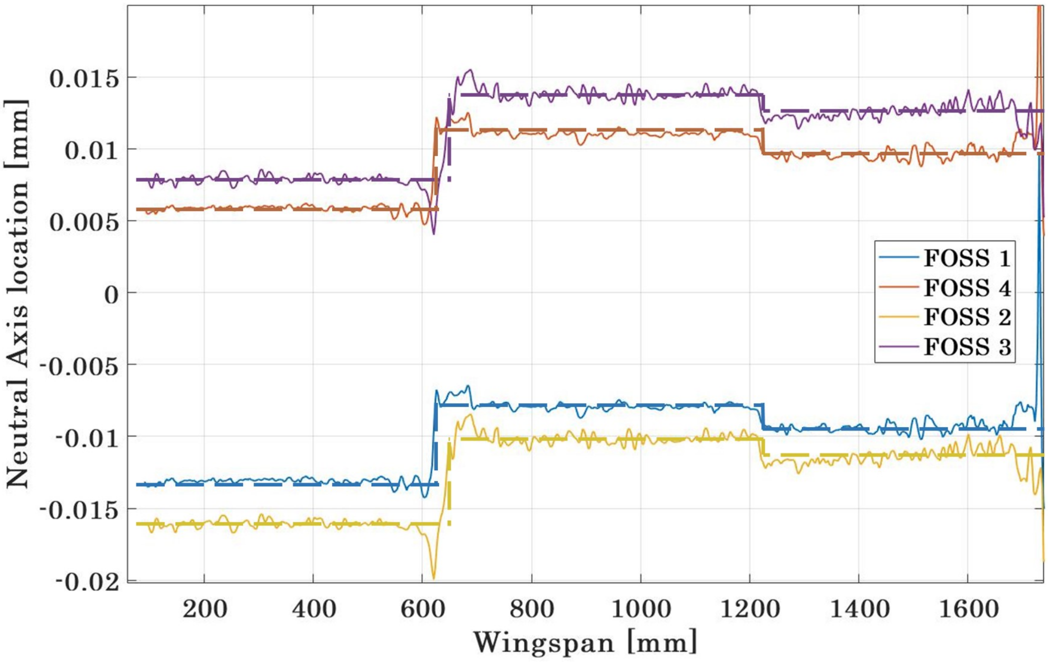

Figure C.5: Distance from FOSS to neutral axis of wing: Piece-wise approximation

D

Repeatablity of MSS: A further graphical analysis

Hereby, the MSS from FOSS1 and FOSS4 for the first and third OOP bending modes are shown. The results from the seven vibration tests overlap, showing great similarity among each other.

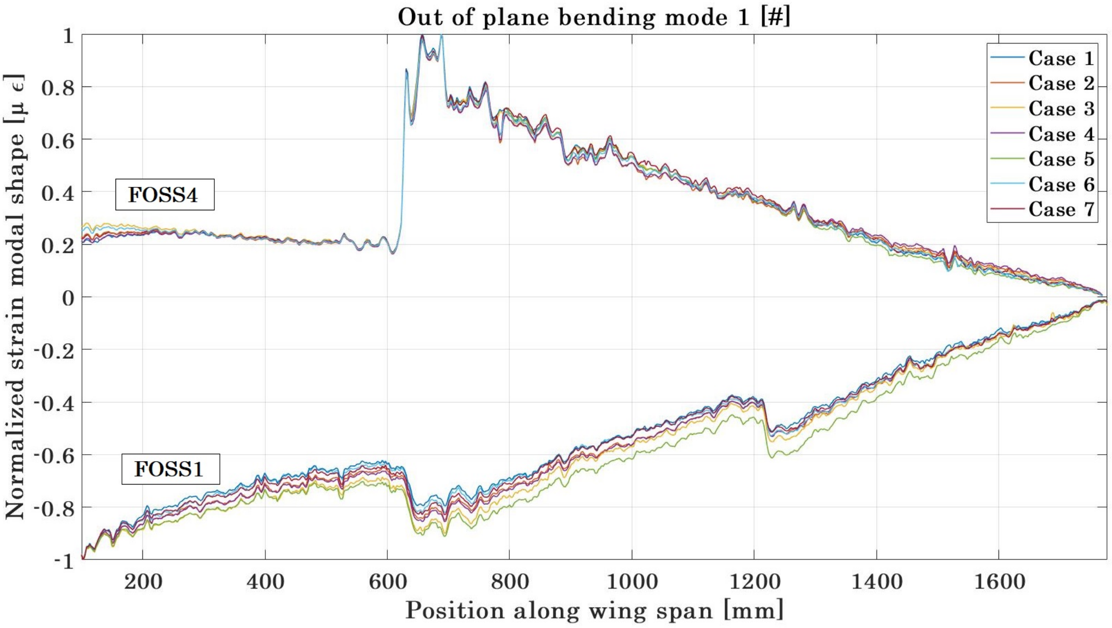

Figure D.1: Repeatability of MSS from seven case measurements: Mode 1, FOSS 1 and 4

The standard deviation and relative error for each sensing gauge of FOSS2, FOSS3 and FOSS4, for all three bending modes analyzed in this project are shown in the graphs below.

As explained in chapter 3 section 3.5, the peaks in error and standard deviation correspond to the node location of the MSS. The information in the above plots is used later in the damage detection algorithm to reduce fault detection in the locations over the wing span.

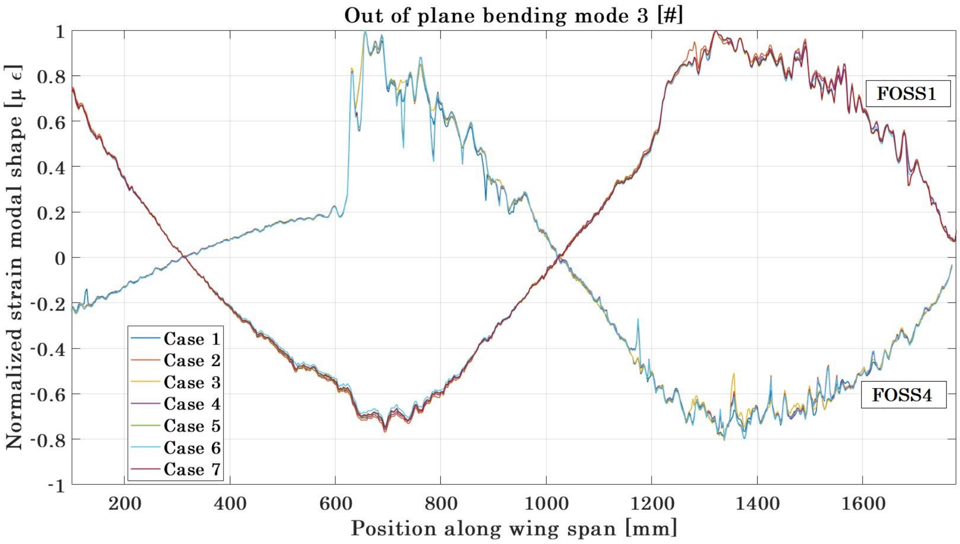

Figure D.2: Repeatability of MSS from seven case measurements: Mode 3, FOSS 1 and 4

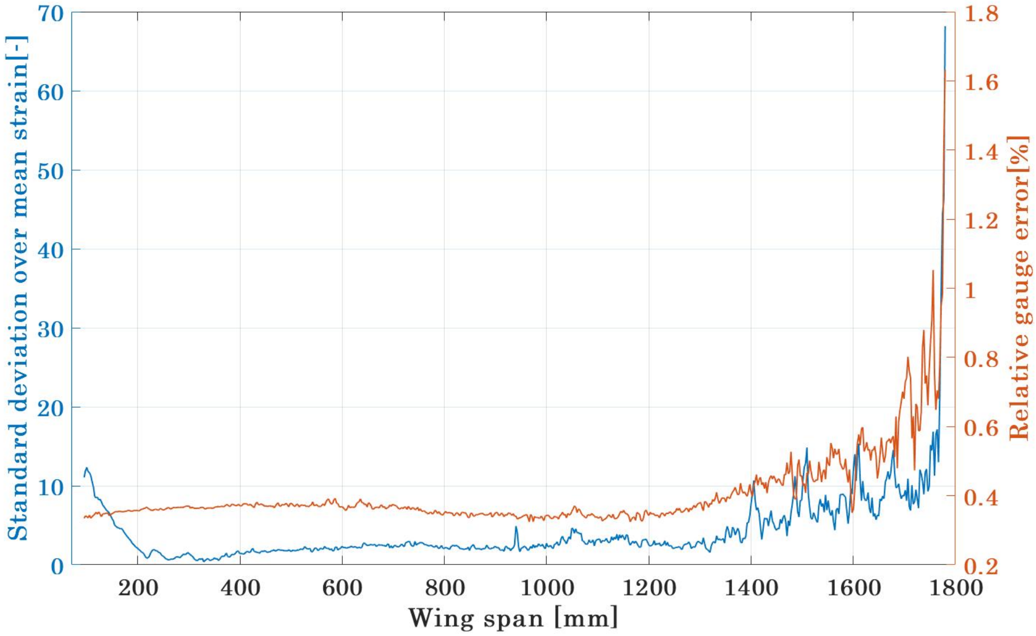

Figure D.3: Standard deviation and error over wing span for 1^{st} mode, FOSS2

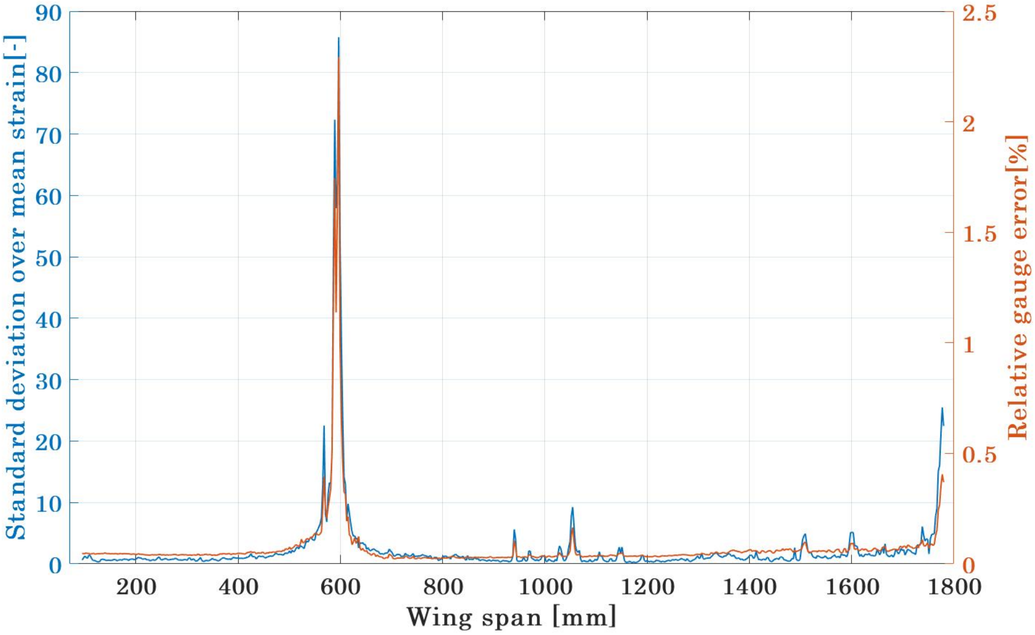

Figure D.4: Standard deviation and error over wing span for 2^{nd} mode, FOSS2

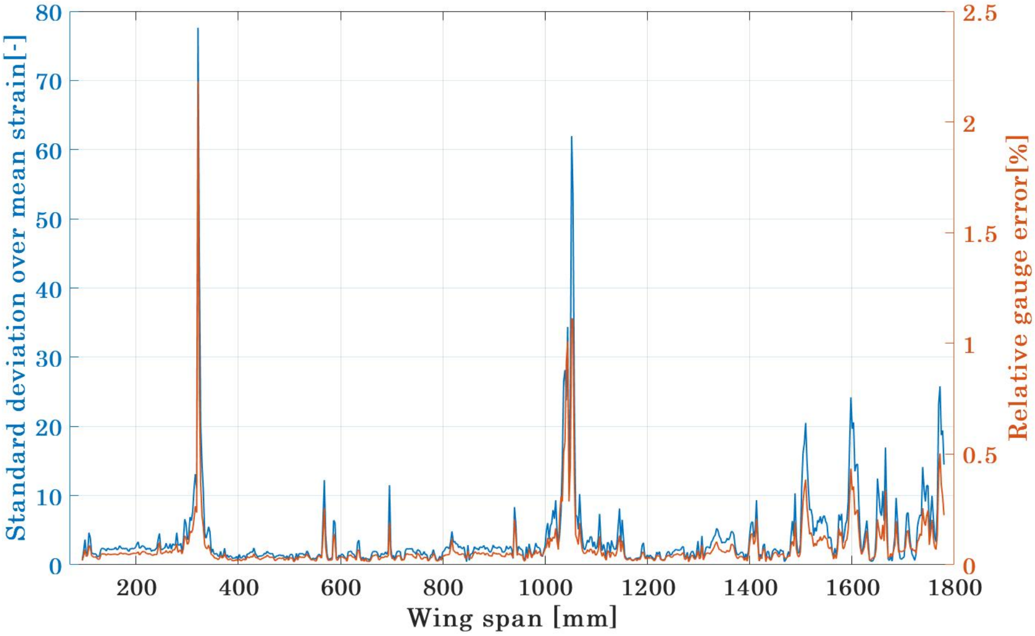

Figure D.5: Standard deviation and error over wing span for 3^{rd} mode, FOSS2

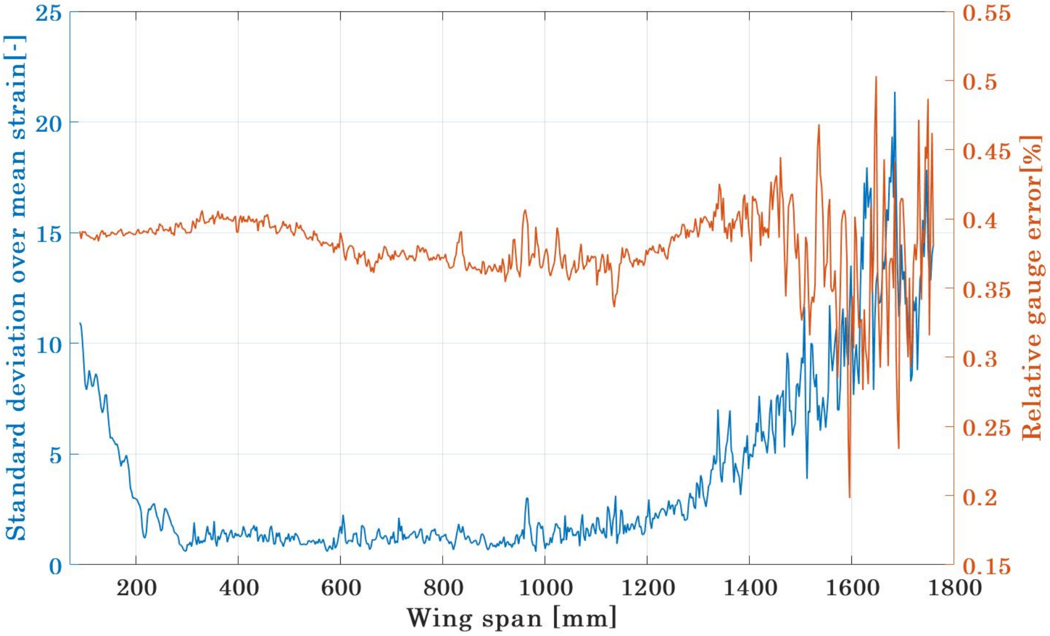

Figure D.6: Standard deviation and error over wing span for 1st mode, FOSS3

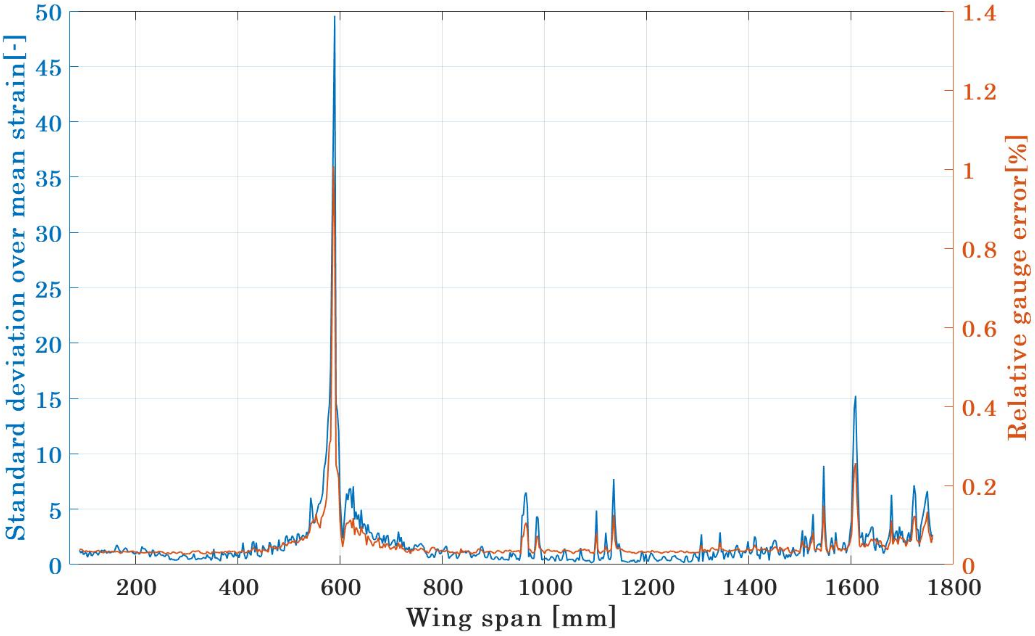

Figure D.7: Standard deviation and error over wing span for 2nd mode, FOSS3

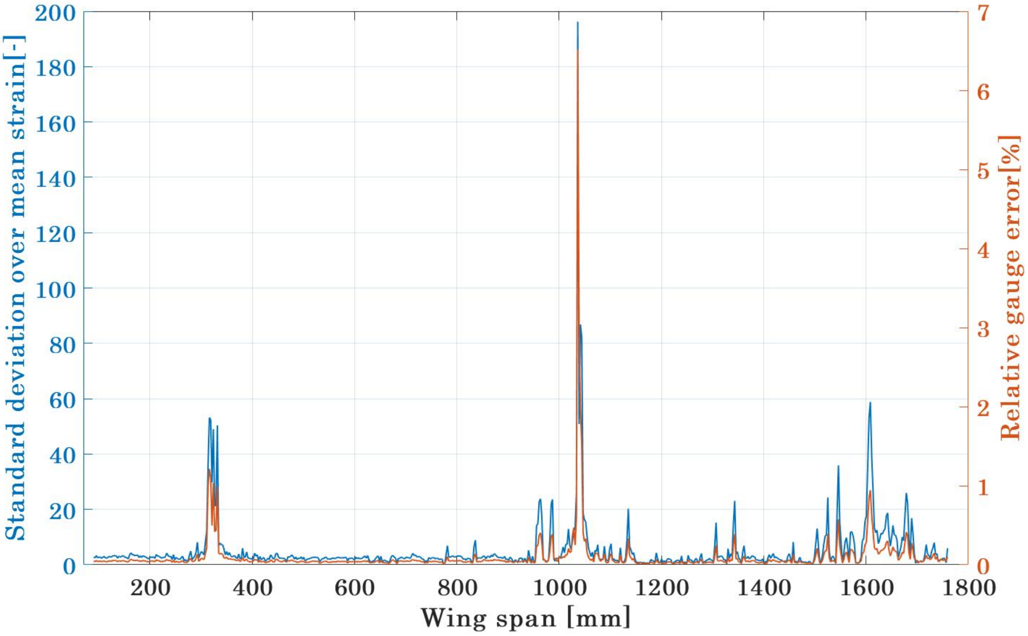

Figure D.8: Standard deviation and error over wing span for 3^{rd} mode, FOSS3

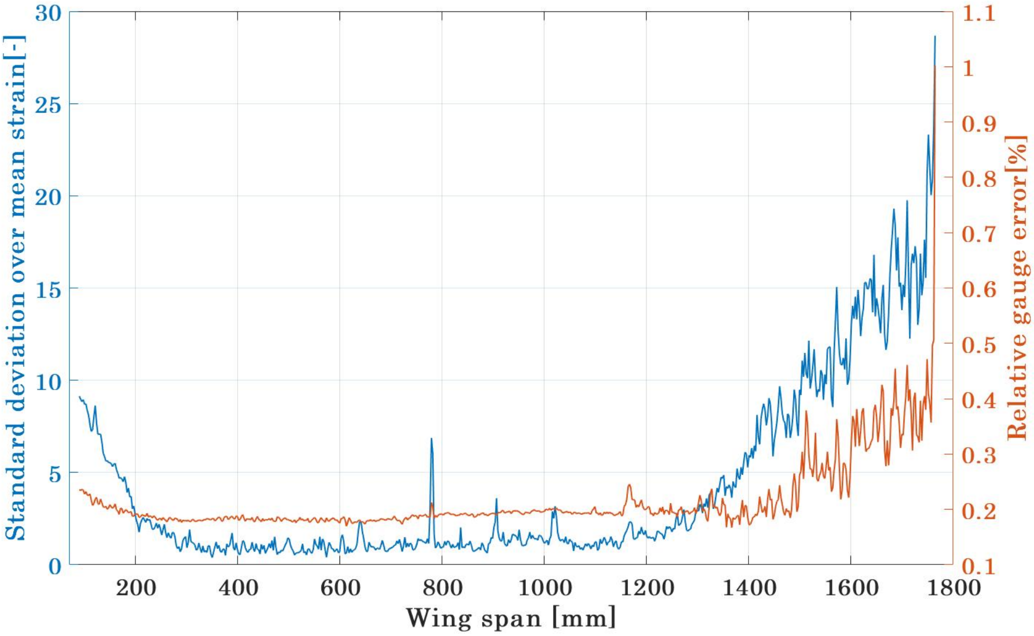

Figure D.9: Standard deviation and error over wing span for 1^{st} mode, FOSS4

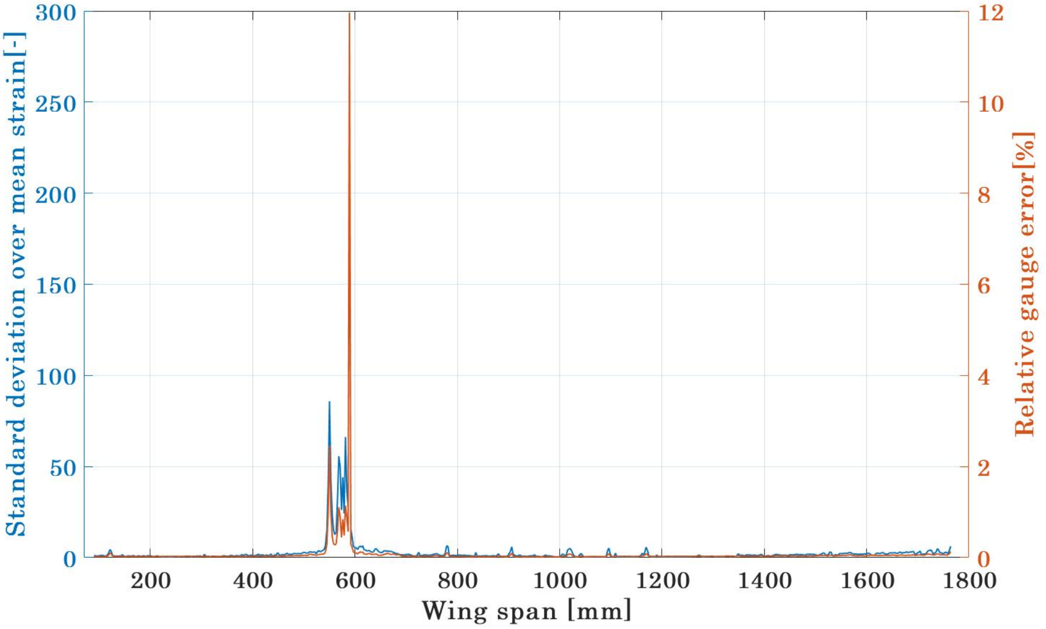

Figure D.10: Standard deviation and error over wing span for 2^{nd} mode, FOSS4

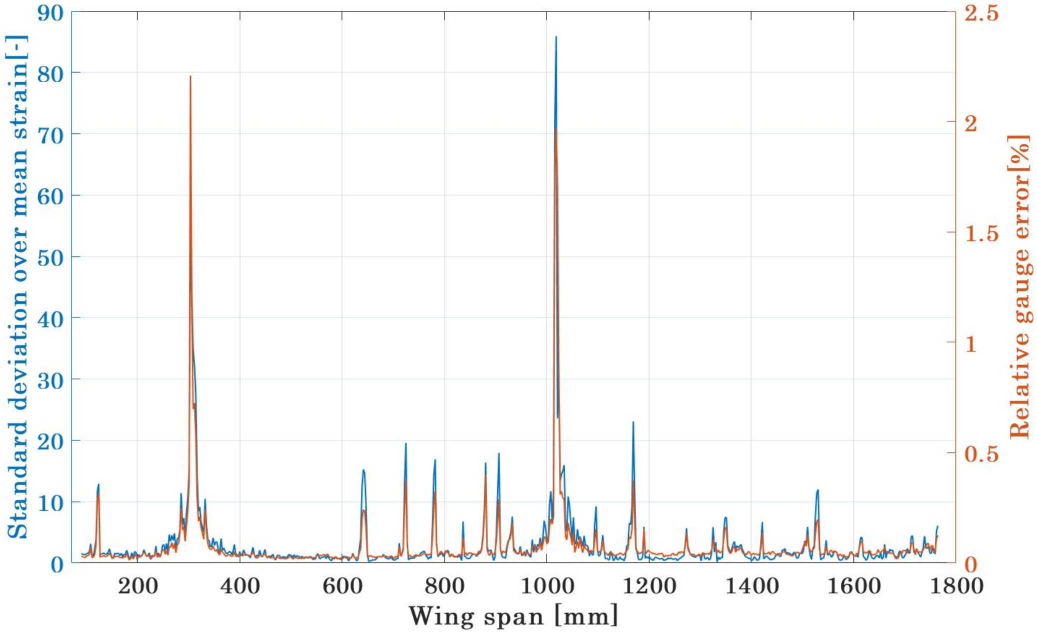

Figure D.11: Standard deviation and error over wing span for 3^{rd} mode, FOSS4

E

Experimental results: A further graphical analysis

The figures below are an extension of the graphical analysis of chapter 4 section 4.4, damage location results.

Figure E.1 displays the probability map of correct damage location over the wingspan. This map was obtained by means of the extrapolation of only the mass experiments conducted on the bottom wing surface. Alternatively, figure E.2 shows the extrapolation in the top wing surface.

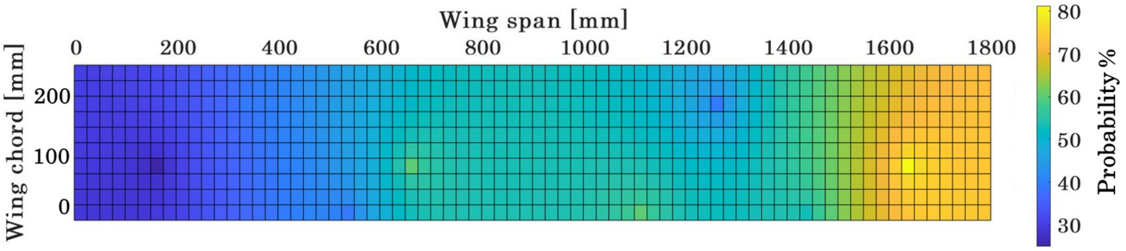

Figure E.1: Probability map of correct damage location in bottom wing surface

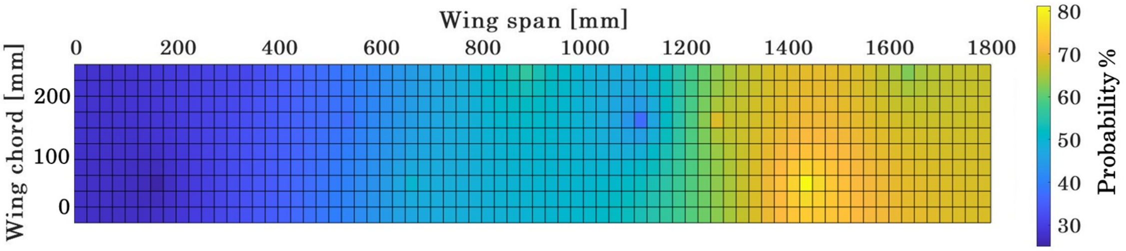

Figure E.2: Probability map of correct damage location in top wing surface

The displayed results do not differ from the discussed ones in chapter 4 section 4.4. The probability of correct damage location increases from root to tip according to the mass and stiffness distribution of the structure.

It is necessary to point out that the figures above are the result of an extrapolation of 9 positions into a mesh of dimensions [11x73] for an element size of 25 mm. This size corresponds to the diameter of the bolt head which is used to introduce the mass damages in the wing.

Bibliography

[1] A Alvandi and C Cremona. “Assessment of vibration-based damage identification techniques.” In: *Journal of Sound and Vibration* 292.1-2 (2006), pp. 179–202.

[2] General Aviation. “Epic Aircraft recibiÃ$^3lacertificaciÃ^3ndelaFAAparasumodeloE$1000.” In: *HangarX* (2019).

[3] Xiaoyi Bao and Liang Chen. “Recent progress in distributed fiber optic sensors.” In: *Sensors* 12.7 (2012), pp. 8601–8639.

[4] Arik Bergman. “Distributed and Dynamic Fiber-Optic Sensing.” PhD thesis. Oct. 2016. DOI: `10.13140/RG.2.2.13584.51207`.

[5] Rune Brincker and Carlos Ventura. *Introduction to operational modal analysis.* John Wiley & Sons, 2015.

[6] Maosen Cao, Maciej Radzieński, Wei Xu, and Wiesław Ostachowicz. “Identification of multiple damage in beams based on robust curvature mode shapes.” In: *Mechanical Systems and Signal Processing* 46.2 (2014), pp. 468–480.

[7] Xiao Chen. “Experimental observation of fatigue degradation in a composite wind turbine blade.” In: *Composite Structures* 212 (2019), pp. 547–551.

[8] Liangliang Cheng and Alfredo Cigada. “An analytical perspective about structural damage identification based on transmissibility function.” In: *Structural Health Monitoring* 19.1 (2020), pp. 142–155.

[9] Liangliang Cheng, Paolo Roberto, Marcello Vanali, Alfredo Cigada, et al. “Damage detection based on strain transmissibility for beam structure by using distributed fiber optics.” In: *Structural Health Monitoring & Damage Detection, Volume 7.* Springer, 2017, pp. 27–40.

[10] Chia Chen Ciang, Jung-Ryul Lee, and Hyung-Joon Bang. “Structural health monitoring for a wind turbine system: a review of damage detection methods.” In: *Measurement Science and Technology* 19.12 (2008), p. 122001.

[11] John M Cimbala. “Taguchi orthogonal arrays.” In: *Pennsylvania State University* (2014).

[12] Phillip Cornwell, Scott W Doebling, and Charles R Farrar. “Application of the strain energy damage detection method to plate-like structures.” In: *Journal of Sound and Vibration* 224.2 (1999), pp. 359–374.

[13] Swagato Das, P Saha, and SK Patro. “Vibration-based damage detection techniques used for health monitoring of structures: a review.” In: *Journal of Civil Structural Health Monitoring* 6.3 (2016), pp. 477–507.

[14] Daniele Dessi and Gabriele Camerlengo. “Damage identification techniques via modal curvature analysis: overview and comparison.” In: *Mechanical Systems and Signal Processing* 52 (2015), pp. 181–205.

[15] Raffaella Di Sante. “Fibre optic sensors for structural health monitoring of aircraft composite structures: Recent advances and applications.” In: *Sensors* 15.8 (2015), pp. 18666–18713.

[16] Scott W Doebling, Charles R Farrar, Michael B Prime, and Daniel W Shevitz. “Damage identification and health monitoring of structural and mechanical systems from changes in their vibration characteristics: a literature review.” In: *Los Alamos National Lab., NM (United States)* (1996).

[17] Scott W Doebling, Charles R Farrar, Michael B Prime, et al. “A summary review of vibration-based damage identification methods.” In: *Shock and Vibration Digest* 30.2 (1998), pp. 91–105.

[18] Ying Du, Shengxi Zhou, Xingjian Jing, Yeping Peng, Hongkun Wu, and Ngaiming Kwok. “Damage detection techniques for wind turbine blades: A review.” In: *Mechanical Systems and Signal Processing* 141 (2020), p. 106445.

[19] David J Ewins. *Modal testing: theory, practice and application.* John Wiley & Sons, 2009.

[20] L Eyer and P Bartholdi. “Variable stars: which Nyquist frequency?” In: *Astronomy and Astrophysics Supplement Series* 135.1 (1999), pp. 1–3.

[21] Wei Fan and Pizhong Qiao. “Vibration-based damage identification methods: a review and comparative study.” In: *Structural Health Monitoring* 10.1 (2011), pp. 83–111.

[22] Charles R Farrar and David A Jauregui. “Comparative study of damage identification algorithms applied to a bridge: I. Experiment.” In: *Smart Materials and Structures* 7.5 (1998), p. 704.

[23] Anmar Frangoul. “Massive wind turbine blade arrives in Massachusetts for testing.” In: *Consumer News and Business Channel* (Nov-2019).

[24] Mark Froggatt and Jason Moore. “High-spatial-resolution distributed strain measurement in optical fiber with Rayleigh scatter.” In: *Applied Optics* 37.10 (1998), pp. 1735–1740.

[25] MSC Software GmbH. “MSC Nastran 2018.2 Quick Reference Guide.” In: (2018).

[26] MSC Software GmbH. “MSC Nastran 2018.2 Reference Manual.” In: (2018).

[27] Yves Govers, G Jelicic, and Taner Akbay. “The use of strain sensors for modal identification of aeroelastic structures.” In: *International Conference on Noise and Vibration Engineering, Leuven, Belgium, Sept.* 2016, pp. 19–23.

[28] Yves Govers, Muhammad Yasser Meddaikar, and Kautuk Sinha. “Model validation of an aeroelastically-tailored forward swept wing using fibre-optical strain measurements.” In: *Proceedings of ISMA2018 International Conference on Noise and Vibration Engineering.* 2018, pp. 1403–1417.

[29] Alfredo Güemes and Antonio Fernandez-Lopez. “Structural health monitoring with fiber optic sensors.” In: *23rd International Conference on Optical Fibre Sensors.* Vol. 9157. International Society for Optics and Photonics. 2014, 91579R.

[30] Cole S Hamey, Wahyu Lestari, Pizhong Qiao, and Gangbing Song. “Experimental damage identification of carbon/epoxy composite beams using curvature mode shapes.” In: *Structural Health Monitoring* 3.4 (2004), pp. 333–353.

[31] Shiuh-Chuan Her and Chih-Ying Huang. "The effects of adhesive and bonding length on the strain transfer of optical fiber sensors." In: *Applied Sciences* 6.1 (2016), p. 13.

[32] LUNA innovations. "Lightweight and advanced materials: Model Validation." In: *https ://lunainc.com/solution/model-validation* ().

[33] Shivi Kesarwani. "Polymer Composites in Aviation Sector." In: *International Journal of Engineering Research and* V6 (June 2017). DOI: `10.17577/IJERTV6IS060291`.

[34] Jeong-Tae Kim, Yeon-Sun Ryu, Hyun-Man Cho, and Norris Stubbs. "Damage identification in beam-type structures: frequency-based method vs mode-shape-based method." In: *Engineering Structures* 25.1 (2003), pp. 57–67.

[35] William L Ko and Van Tran Fleischer. "Further Development of Ko Displacement Theory for Deformed Shape Predictions of Nonuniform Aerospace Structures." In: (2009).

[36] William L Ko, W Lance Richards, and Van T Tran. "Displacement theories for in-flight deformed shape predictions of aerospace structures." In: *NASA, patent number NASA/TP-2007-214612* (2007).

[37] Tadej Kranjc, Janko Slavič, and Miha Boltežar. "A comparison of strain and classic experimental modal analysis." In: *Journal of Vibration and Control* 22.2 (2016), pp. 371–381.

[38] Stephen T Kreger, Dawn K Gifford, Mark E Froggatt, Alex K Sang, Roger G Duncan, Matthew S Wolfe, and Brian J Soller. "High-resolution extended distance distributed fiber-optic sensing using Rayleigh backscatter." In: *Sensor Systems and Networks: Phenomena, Technology, and Applications for NDE and Health Monitoring 2007*. Vol. 6530. International Society for Optics and Photonics. 2007, 65301R.

[39] Stephen T Kreger et al. "Optical frequency domain reflectometry for aerospace applications." In: *Fiber Optic Sensors and Applications XIV*. Vol. 10208. International Society for Optics and Photonics. 2017, p. 1020803.

[40] Andreas Kunzel and Petryna Y.S. "Parameter Identification based on quasi-continuous strain data captured by high resolution fiber optic sensing." In: *European Workshop On Structural Health Monitoring 2016*. EWSHM. July 2016.

[41] Wahyu Lestari and Pizhong Qiao. "Damage detection of fiber-reinforced polymer honeycomb sandwich beams." In: *Composite Structures* 67.3 (2005), pp. 365–373.

[42] Dongsheng Li, Siu-Chun M Ho, Gangbing Song, Liang Ren, and Hongnan Li. "A review of damage detection methods for wind turbine blades." In: *Smart Materials and Structures* 24.3 (2015), p. 033001.

[43] Hong-Nan Li, Dong-Sheng Li, and Gang-Bing Song. "Recent applications of fiber optic sensors to health monitoring in civil engineering." In: *Engineering Structures* 26.11 (2004), pp. 1647–1657.

[44] Hui Li, Shunlong Li, Jinping Ou, and Hongwei Li. "Modal identification of bridges under varying environmental conditions: temperature and wind effects." In: *Structural Control and Health Monitoring* 17.5 (2010), pp. 495–512.

[45] YY Li. “Hypersensitivity of strain-based indicators for structural damage identification: A review.” In: *Mechanical Systems and Signal Processing* 24.3 (2010), pp. 653–664.

[46] YY Li, Li Cheng, LH Yam, and Wai On Wong. “Identification of damage locations for plate-like structures using damage sensitive indices: strain modal approach.” In: *Computers & Structures* 80.25 (2002), pp. 1881–1894.

[47] A Messina, EJ Williams, and T Contursi. “Structural damage detection by a sensitivity and statistical-based method.” In: *Journal of Sound and Vibration* 216.5 (1998), pp. 791–808.

[48] Leon Mishnaevsky, Kim Branner, Helga Nørgaard Petersen, Justine Beauson, Malcolm McGugan, and Bent F Sørensen. “Materials for wind turbine blades: an overview.” In: *Materials* 10.11 (2017), p. 1285.

[49] Diogo Montalvao, Nuno Manuel Mendes Maia, and António Manuel Relógio Ribeiro. “A review of vibration-based structural health monitoring with special emphasis on composite materials.” In: *Shock and Vibration Digest* 38.4 (2006), pp. 295–324.

[50] Maria Mrazova. “Advanced composite materials of the future in aerospace industry.” In: *Incas Bulletin* 5.3 (2013), p. 139.

[51] Rogier P.L. Nijssen. “Fatigue life prediction and strength degradation of wind turbine rotor blade composites.” In: *Contractor Report SAND2006-7810P, Sandia National Laboratories, Albuquerque, NM* (2006).

[52] Ted Ooijevaar. “Vibration based structural health monitoring of composite skin-stiffener structures.” In: *Universiteit Twente* (2014).

[53] AK Pandey, M Biswas, and MM Samman. “Damage detection from changes in curvature mode shapes.” In: *Journal of Sound and Vibration* 145.2 (1991), pp. 321–332.

[54] Bart Peeters, Herman Van der Auweraer, Patrick Guillaume, and Jan Leuridan. “The PolyMAX frequency-domain method: a new standard for modal parameter estimation?” In: *Shock and Vibration* 11.3, 4 (2004), pp. 395–409.

[55] P Pennacchi, G Cazzulani, M Chieppi, and A Colombo. “Optimal positioning of continuous optical fiber sensors for the modal analysis of turbine blades with optical backscatter reflectometer technology.” In: *ISMA2018 International Conference on Noise and Vibration Engineering.* KU Leuven-Departement Werktuigkunde. 2018, pp. 1361–1373.

[56] PCB Piezoelecrics. “MODEL:080A109. ACCESSORY FOR VIBRATION DIVISION PRODUCT.” In: *http://www.pcb.com/products?m=080A109* (Accessed on: 12/02/2021).

[57] Prajoy Podder, Tanvir Zaman Khan, Mamdudul Haque Khan, and M Muktadir Rahman. “Comparative performance analysis of Hamming, Hanning and Blackman window.” In: *International Journal of Computer Applications* 96.18 (2014).

[58] Wei Qiao and Dingguo Lu. “A survey on wind turbine condition monitoring and fault diagnosisÂ—Part II: Signals and signal processing methods.” In: *IEEE Transactions on Industrial Electronics* 62.10 (2015), pp. 6546–6557.

[59] Darwin Rajpal. “Dynamic aeroelastic optimization of composite wings including fatigue considerations.” In: *Delft University of Technology* (2021).

[60] Manjusha Ramakrishnan, Ginu Rajan, Yuliya Semenova, and Gerald Farrell. “Overview of fiber optic sensor technologies for strain/temperature sensing applications in composite materials.” In: *Sensors* 16.1 (2016), p. 99.

[61] Koushik Roy and Samit Ray-Chaudhuri. “Fundamental mode shape and its derivatives in structural damage localization.” In: *Journal of Sound and Vibration* 332.21 (2013), pp. 5584–5593.

[62] Mark A Rumsey and Joshua A Paquette. “Structural health monitoring of wind turbine blades.” In: *Smart Sensor Phenomena, Technology, Networks, and Systems 2008*. Vol. 6933. International Society for Optics and Photonics. 2008, 69330E.

[63] Anders Rytter. “Vibrational based inspection of civil engineering structures.” In: *Dept. of Building Technology and Structural Engineering, Aalborg University* (1993).

[64] Namita Sahoo, Weijia Bao, Shen Liu, Yidong Tan, Kaiming Zhou, and Lin Zhang. “Fibre Bragg grating inscription into a seven core fibre and its application as a vector bending sensor.” In: *Optical Sensors 2021*. Vol. 11772. International Society for Optics and Photonics. 2021, 117720O.

[65] Edward Sazonov and Powsiri Klinkhachorn. “Optimal spatial sampling interval for damage detection by curvature or strain energy mode shapes.” In: *Journal of Sound and Vibration* 285.4-5 (2005), pp. 783–801.

[66] Peter J Schubel and Richard J Crossley. “Wind turbine blade design.” In: *Energies* 5.9 (2012), pp. 3425–3449.

[67] Mark J Schulz and MJ Sundaresan. “Smart sensor system for structural condition monitoring of wind turbines.” In: *Denver, Colorado, USA: National Renewable Energy Laboratory* (2006).

[68] Brian J Schwarz and Mark H Richardson. “Experimental modal analysis.” In: *CSI Reliability Week* 35.1 (1999), pp. 1–12.

[69] Peyman Shabani, Fathollah Taheri-Behrooz, Seyed Sina Samareh-Mousavi, and Mahmood M Shokrieh. “Very high cycle and gigacycle fatigue of fiber-reinforced composites: A review on experimental approaches and fatigue damage mechanisms.” In: *Progress in Materials Science* 118 (2021), p. 100762.

[70] Julián Sierra-Pérez, Miguel Angel Torres-Arredondo, and Alfredo Güemes. “Damage and nonlinearities detection in wind turbine blades based on strain field pattern recognition. FBGs, OBR and strain gauges comparison.” In: *Composite Structures* 135 (2016), pp. 156–166.

[71] Irene Solbes Ferri. “Dynamic contiuous fiber optical strain sensing for damage detection and strucutral health monitoring of wind turbine blades.” In: *Report from Technical University of Delft* (2021).

[72] Bent F Sørensen, John W Holmes, Povl Brøndsted, and Kim Branner. “Blade materials, testing methods and structural design.” In: *Wind power generation and wind turbine design* (2010), pp. 417–466.

[73] Bent F Sørensen, Erik Joergensen, Christian P Debel, FM Jensen, HM Jensen, T Jacobsen, and KM Halling. “Improved design of large wind turbine blade of fibre composites based on studies of scale effects (Phase 1)-Summary report.” In: *Risø National Laboratory, Denmark* (2004).

[74] Bent F Sørensen, Lars Lading, and Peter Sendrup. “Fundamentals for remote structural health monitoring of wind turbine blades-a pre-project.” In: *Risø National Laboratory, Denmark* (2002).

[75] Genichi Taguchi and V Cariapa. “Taguchi on robust technology development.” In: (1993).

[76] Martin D Ulriksen, Dmitri Tcherniak, Poul H Kirkegaard, and Lars Damkilde. “Operational modal analysis and wavelet transformation for damage identification in wind turbine blades.” In: *Structural Health Monitoring* 15.4 (2016), pp. 381–388.

[77] P Vacher, B Jacquier, and A Bucharles. “Extensions of the MAC criterion to complex modes.” In: *Proceedings of the International Conference on Noise and Vibration Engineering*. 2010, pp. 2713–2726.

[78] Srikanth Vasudevan. “Ground Vibration Testing: System Identification using Fiber Optics.” In: *DLR Institute of Aeroelasticity* (2020).

[79] Daichi Wada, Hirotaka Igawa, Masato Tamayama, Tokio Kasai, Hitoshi Arizono, and Hideaki Murayama. “Real-Time Stress Concentration Monitoring of Aircraft Structure During Flights Using Optical Fiber Distributed Sensor with High Spatial Resolution.” In: *International Committee on Aeronautical Fatigue*. Springer. 2019, pp. 1082–1090.

[80] MM Abdel Wahab and Guido De Roeck. “Damage detection in bridges using modal curvatures: application to a real damage scenario.” In: *Journal of Sound and Vibration* 226.2 (1999), pp. 217–235.

[81] Jörg Waldvogel. “Towards a general error theory of the trapezoidal rule.” In: *Approximation and Computation*. Springer, 2010, pp. 267–282.

[82] Yanfeng Wang, Ming Liang, and Jiawei Xiang. “Damage detection method for wind turbine blades based on dynamics analysis and mode shape difference curvature information.” In: *Mechanical Systems and Signal Processing* 48.1-2 (2014), pp. 351–367.

[83] Timothy M Whalen. “The behavior of higher order mode shape derivatives in damaged, beam-like structures.” In: *Journal of Sound and Vibration* 309.3-5 (2008), pp. 426–464.

[84] Wei Xu, Maosen Cao, Wies?aw Ostachowicz, Maciej Radzie?ski, and Ning Xia. "Two-dimensional curvature mode shape method based on wavelets and Teager energy for damage detection in plates." In: *Journal of Sound and Vibration* 347 (2015), pp. 266–278. ISSN: 0022-460X. DOI: `https://doi.org/10.1016/j.jsv.2015.02.038`. URL: `https://www.sciencedirect.com/science/article/pii/S0022460X15001923`.

[85] Bin Yang and Dongbai Sun. "Testing, inspecting and monitoring technologies for wind turbine blades: A survey." In: *Renewable and Sustainable Energy Reviews* 22 (2013), pp. 515–526.

[86] XW Ye, YH Su, and JP Han. "Structural health monitoring of civil infrastructure using optical fiber sensing technology: A comprehensive review." In: *The Scientific World Journal* 2014 (2014).

[87] MK Yoon, D Heider, JW Gillespie Jr, CP Ratcliffe, and RM Crane. "Local damage detection using the two-dimensional gapped smoothing method." In: *Journal of Sound and Vibration* 279.1-2 (2005), pp. 119–139.

[88] Jie Zhou and Zheng Li. "Damage detection based on vibration for composite sandwich panels with truss core." In: *Composite Structures* 229 (2019), p. 111376.